

Dynamics in Thin, Freely Suspended, Fluid Films: Impact of Picoliter Droplets and In-plane Microrheology

Dissertation

zur Erlangung des akademischen Grades

doctor rerum naturalium

(Dr. rer. nat.)

genehmigt durch die Fakultät für Naturwissenschaften
der Otto-von-Guericke-Universität Magdeburg

von Dipl.-Chem. Sarah Dölle
geb. am 19.10.1983 in Halle (Saale)

Gutachter: Prof. Dr. Ralf Stannarius

Prof. Dr. Frank Giesselmann

eingereicht am: 25.09.2017

verteidigt am: 12.04.2018

Otto von Guericke University Magdeburg
Faculty of Natural Science

Abstract

Dissertation

**Dynamics in thin, freely suspended, fluid films:
Impact of Picoliter Droplets and In-plane Microrheology**

Dipl.-Chem. Sarah Dölle

We employ high-speed video imaging to study microdroplets of a few picoliters volume impacting on freely suspended smectic liquid-crystal films. Depending on the impact parameters, in particular droplet velocity and mass, three different regimes are observed such as trapping, bouncing and tunneling. Fast droplets may penetrate the film completely (tunneling). After they have passed the film, they are coated with a layer of film material while the original smectic film remains intact. Droplets with a velocity in a certain intermediate range deform the film, which hurls the droplet back (bouncing). In both regimes, tunneling and bouncing, a substantial amount of kinetic energy is lost. The energy is partially dissipated during droplet impact and during subsequent mechanical vibrations and oscillations of the film and the droplet. Slow droplets are caught and embedded in the film (trapping). A side aspect is the determination of interface tensions of the materials from the balance of capillary forces. The hydrodynamics of thin freely suspended fluid films were analyzed by investigating the gravitation-induced motion of droplets and beads on inclined smectic films. Thin smectic films are ideal model systems to study the exceptional phenomenon of in-plane flow close to two dimensions. The mobility of droplets and the viscosity of the film were measured for a SmA material (a mixture of a 4-nitrophenyl-4'-alkyloxybenzoate and four 4-alkyloxyphenyl-4'-alkyl(oxy)benzoates). Considering the hydrodynamics of the film, no difference to solid inclusions were found. The mobility follows a Saffman-like behavior in films with a Saffman length much smaller than the film width. When the Saffman length becomes comparable to the film width, the hydrodynamics are solely governed by lateral confinement effects and air-film-coupling can be disregarded. The more complex SmC films (Phenylpyrimidine mixture) were investigated using solid silica beads as inclusion material. The orientation of the SmC director was tested to have no effect on the mobility of the beads. The flow field around a moving bead as well as the dynamics in SmC films are in good agreement with the behavior in SmA films.

Otto-von-Guericke-Universität Magdeburg
Fakultät für Naturwissenschaften

Kurzzusammenfassung

Dissertation

**Dynamik in dünnen, freistehenden, fluiden Filmen:
Einschlag von Picolitertröpfchen und Mikrorheologie in der Filmebene**

Dipl.-Chem. Sarah Dölle

Die Hydrodynamik des Einschlages von Pikolitertropfen auf einen freistehenden, smektischen Film wurde mit Hilfe einer Hochgeschwindigkeitskamera untersucht. In Abhängigkeit von der Aufprallgeschwindigkeit und der Tropfenmasse konnten verschiedene Regime nachgewiesen werden. Tropfen mit hoher Geschwindigkeit schlagen bzw. tunneln durch den Film. Nach ihrem Austritt auf der anderen Seite des Films sind die Tröpfchen von Filmmaterial ummantelt. Der smektische Film heilt trotz Materialverlusts wieder vollständig aus. In einem Bereich mittlerer Aufprallgeschwindigkeiten, tritt ein Trampolineffekt auf. Die Tröpfchen deformieren den Film, gehen aber keine Verbindung ein und werden wieder zurückgeschleudert. Bei diesem wie auch beim Tunnelprozess wird ein erheblicher Teil der anfänglichen kinetischen Energie dissipiert. Die Energie wird teils in die Deformation des Aufschlags, teils in anschließende mechanische Vibrationen von Tropfen und Film umgewandelt. Tröpfchen, die mit einer niedrigeren Geschwindigkeit landen, werden nach dem Auftreffen in den Film eingebettet. Diese Einbettung lässt sich in drei Phasen einteilen. In der ersten Phase des Aufschlages wird kinetische Energie innerhalb von Mikrosekunden dissipiert. Film und Tropfen erhalten eine gemeinsame Grenzfläche. Die zweite Phase ist geprägt von einem Wirken der Kapillarkräfte hin zu einer Gleichgewichtsform. Dieser Prozess ist in weniger als einer halben Sekunde weitgehend abgeschlossen. Für die Analyse dieser ultraschnellen Formänderungen des Tröpfchens ist eine sowohl zeitlich als auch räumlich hochauflösende Kamera unverzichtbar. Im Verlauf der Einbettung wird um das Tröpfchen in der dritten und längsten Phase ein Meniskus aus Filmmaterial gebildet. Die Bildung des Meniskus ist filmdickenabhängig und kann einige Sekunden in Anspruch nehmen aber auch nach mehreren Minuten noch nicht abgeschlossen sein. Neben diesen Betrachtungen, konnten auch Oberflächenspannungen der Materialien gemessen werden, da die Grenzflächenspannungen direkt aus dem Gleichgewichtszustand der beobachteten Kontaktwinkel hervorgeht.

Die durch Gravitation gerichtete Bewegung von Tropfen und Glaskugeln in einem geneigten, freistehenden Film wurde genutzt, um die Hydrodynamik in dünnen Filmen zu erforschen. Dünne, freistehende, fluide Filme sind optimale Modellsysteme um

Strömungen und Fließverhalten in 2D zu untersuchen. Die Beweglichkeit von Tröpfchen und die Viskosität des Filmes wurden für ein SmA Material (eine Mischung bestehend aus einem 4-Nitrophenyl-4'-alkyloxybenzoat und vier 4-Alkyloxyphenyl-4'-alkyl(oxy)-benzoaten) ermittelt. Die Resultate zeigen keine Differenz zur Beweglichkeit von festen Inklusionen in SmA Filmen. Die Beweglichkeit kann durch das Saffman-Delbrück-Modell beschrieben werden, wenn die Saffmanlänge der Inklusion wesentlich kleiner ist als die Filmbreite. Wächst die Saffmanlänge auf eine Größenordnung, die mit der Filmbreite vergleichbar ist, wird die Hydrodynamik durch die Wechselwirkung des Filmflusses mit der äußeren Begrenzung dominiert. Die Reibung mit der umgebenden Luft kann dann vernachlässigt werden. Allerdings müssen bei Experimenten mit flüssigen im Gegensatz zu festen Inklusionen Phänomene wie Evaporation, Formänderung beim Einbetten des Tröpfchens in den Film und Meniskusbildung beachtet werden. Die Meniskusbildung tritt zwar auch bei festen Inklusionen auf, wirkt sich bei flüssigen Inklusionen, bedingt durch einen geringeren Unterschied der Dichten, jedoch relativ stärker auf die Gewichtskraft aus. Die Wechselwirkung von zwei Tröpfchen, welche sich in unmittelbarer Nähe zueinander auf einem Film bewegen, wurde beobachtet. Wird eine bestimmte Distanz zwischen diesen Inklusionen nicht überschritten, bewegen sich die Tröpfchen in einem gemeinsamen Strömungsfeld. Das bewirkt eine signifikante Erhöhung der Geschwindigkeiten beider Tröpfchen. Die Geschwindigkeit ließe sich jetzt eher durch die kombinierte Masse beider Tröpfchen beschreiben.

In den komplexeren SmC Filmen wurden als Inklusionsmaterialien Glaskugeln verwendet, das Filmmaterial bestand aus einer Phenylpyrimidin-Mischung. Die Orientierung des \vec{c} Direktors um eine ruhende Glaskugel folgt einem Defekt der topologische Stärke +1. Diese Orientierung wird teilweise zurückgedrängt wenn die Inklusion anfängt sich schneller im Film zu bewegen. Dann orientiert sich der \vec{c} Direktor entsprechend der Strömung, welche keinen erkennbaren Unterschied zum Strömungsfeld eines SmA Films zeigt. Es wurde der Frage nachgegangen, ob sich die Orientierung des \vec{c} Direktors auf die Beweglichkeit einer Inklusion im Film auswirkt. Experimentell wurden dafür Partikel auf Filmen mit komplexeren Direktorfeldern und Inversionswänden untersucht, jedoch konnte kein Zusammenhang nachgewiesen werden. Die Filmdicken der SmC Filme wurden, bedingt durch die zur optischen Beobachtung erforderliche Doppelbrechung, größer als 1000 nm gewählt. Die experimentell gewählten Bedingungen resultieren in einer Hydrodynamik der Filme, welche durch Wechselwirkung der Strömung mit dem Filmhalter limitiert ist und sich durch die 2D Navier-Stokes-Gleichungen für begrenzte Geometrien beschreiben lässt.

Contents

Abstract	i
Kurzzusammenfassung	ii
Contents	iv
Preface	vi
1 Introduction	1
1.1 Basics of Liquid Crystals	1
1.1.1 The Nematic Mesophase and the Director Concept	2
1.1.2 Smectic Mesophases	4
1.1.3 Optical Anisotropy	5
1.1.4 Viscosity	7
1.1.5 Freely Suspended Smectic Films	10
1.1.6 π -Walls in SmC Films	12
1.2 Impact Dynamics of Droplets	13
1.2.1 Classification through Weber and Ohnesorge Numbers	14
1.2.2 Impact of Picoliter Droplets on Fluid Films	15
1.3 Inclusions in Smectic Films	16
1.3.1 Geometry of Inclusions	17
1.3.2 Interfacial Tension of Embedded Droplets	19
1.4 Dynamics in Thin Films	19
1.4.1 The Stokes' Paradox	20
1.4.2 Theoretical Approaches to 2D Fluid Dynamics	20
1.4.3 Experimental Approaches to "Quasi 2D" Fluid Dynamics	22
2 Experimentals	23
2.1 Materials	23
2.1.1 Film materials	24
2.1.2 Inclusion materials	25
2.2 Equipment	26
2.3 Sample Preparation and Setups	27
2.3.1 Operating the Drop-on-Demand Dispenser	27
2.3.2 Vertical Film Setup	29
2.3.3 Droplet Impact Setup	30
2.3.4 Tilted Microscope Setup	31
2.4 Measuring Techniques	33

2.4.1	Measurement of Film Thickness	33
2.4.2	Determination of the SmC Director	35
2.4.3	Fluorescence Microscopy	37
2.4.4	Inclusion Tracking	38
3	Impact of Picoliter Droplets	40
3.1	Impact on Silicon Wafer and Evaporation	40
3.2	Impact on Smectic Films: Trapping	42
3.2.1	The Embedding	43
3.2.2	Meniscus Formation	48
3.3	Impact on Smectic Films: Bouncing	51
3.3.1	Droplet and Film Deformations	52
3.3.2	Energy Loss and Holding Force	54
3.4	Impact on Smectic Films: Tunneling	56
3.4.1	Energy Loss	57
3.4.2	Detachment and Self-Healing	59
3.4.3	Coated Droplets	60
3.5	We-Oh Classification	63
3.6	Conclusions	63
4	Motion of Inclusions in Freely Suspended Films	65
4.1	Experimental Model	66
4.1.1	The Buoyancy	66
4.1.2	The Gravitational Force	67
4.1.3	The Frictional Force	70
4.2	Droplet Motion in a SmA Film	71
4.2.1	Experiments with Embedded Droplets	72
4.2.2	Determination of the Film Viscosity	72
4.2.3	Droplet Velocities and Mobilities	75
4.2.4	Motion of Two Droplets in Proximity	76
4.3	Motion of Glass Beads in SmC Films	78
4.3.1	Smectic Orientation around Beads	79
4.3.2	Flow Field around Beads	81
4.3.3	Bead Moving Through π -Walls	83
4.3.4	Bead Velocity and Mobility	86
4.4	Conclusions	87
	Bibliography	90

Preface

Motivation

Many people hearing about freely suspended liquid crystal films for the first time may feel a bit lost, even after explaining a liquid crystal and a freely suspended film. Inevitably, the question arises that fundamental researchers dread coming up: Why is anybody interested in this? And even more challenging: What does that have to do with me? Let me try to answer the first question, then you can decide the second one for yourself.

Freely suspended fluid films are something almost everybody discovered and loved during their childhood in the form of soap bubbles. They are basically a liquid put into the restricted geometry of a thin film. If such a film is very thin, which is experimentally feasible with smectic liquid crystals, it can almost be regarded as a fluid stretched out in two dimensions so that the third one can be completely disregarded. In other words, smectic liquid crystals are excellent model systems for quasi-two-dimensional fluids. Until our knowledge is quite incomplete about the field of 2D fluid dynamics and here is why.

The theory of *ideal* 2D fluid dynamics has ever been a challenging and possibly frustrating problem since no trivial solution could be found. So far, all efforts have led to the so called *Stokes Paradox*. Experimentalists strive to come closer to a solution by trying to create experiments in 2D environments. But how can you realize experiments in 2D? Well, setting the philosophical discourses aside, it is not surprising: you cannot. And even though you may come close, it is not sufficient to realize the theory. It is fascinating how a problem that refuses to be designable in real life may not be described theoretically as well. For me, this seems to agree very well and reminds me instantly of Heisenberg's uncertainty principle.

Apart from theoretical questions, a profound knowledge about the flow in these restricted geometries would be beneficial for various biological, physical and chemical systems. The motion of proteins or lipid rafts depends on the fluid flow in the geometrically restricted membranes. [1–3]. Researchers investigating smectic liquid crystal

films are interested in the dynamics of defects, textures and inclusions in those film. Also, new characteristics may arise when forcing a fluid into a new geometry. For thin liquid crystalline films, temperatures of phase transitions can be shifted gravely. Some 3D systems may even pose questions that are closely related to 2D problems, like a wire falling in a 3D fluid [4].

The second subject of my thesis deals with droplet impacts on freely suspended fluid films. It may not seem related at first glance, however, this topic evolved naturally from the first one since I placed micrometer sized droplets as tracer particles on fluid films to investigate the dynamics. The investigation of the impact process of picoliter droplets turned out to be quite interesting and rewarding when phenomena like droplet rebound and tunneling were discovered. The evolution of the droplet impact where forces are balanced by microscopic shape changes is relevant for interfacial science. The tunneling of droplets results in a formation of microcapsules which might be even valuable for technological applications. Furthermore, there is economic interest in this research because for instance ink-jet printing systems gradually shift down to smaller droplet sizes for better resolutions. The impact of such droplets on freely suspended films has never been investigated as detailed and well resolved as in this work. Particularly, impact on smectic films adds a completely novel aspect to this field.

Outline

This thesis is based on my research from 2011 to 2015. The central subject matter of this thesis is freely suspended smectic films. The aim of this thesis is the investigation of viscous and capillary forces acting on small micrometer sized liquid or solid inclusions as well as their motion in freely suspended films of different smectic phases. Initially, the focus of my work was directed at the dynamics of these films. In the process of researching, it became apparent that the impact and especially the evolution of small droplets on freely suspended films were crucial for analyzing the dynamics of embedded droplets. However, the topic of droplet impact emerged to be both interesting and challenging, growing to a part of my thesis equal to film dynamics. Whereas the introduction comprises these two topics, two separate chapters present the findings each containing experimental results, discussions and conclusions.

In the introduction, the basics of liquid crystals are developed up to a point where smectic phases and some of their features may be understood. Then, droplet impact on freely suspended films is introduced, followed by a short overview of inclusions in freely suspended films, focusing mainly on geometry and interfacial tensions. Finally, the section of dynamics in thin films allows a basic understanding of the limitations and

intriguing peculiarities of the hydrodynamic theory in two dimensions. A brief summary of the experimental findings for thin film dynamics concludes the introduction. I tried to keep the order of the introduction, not including the basics of liquid crystals, throughout the thesis. Thus, the findings are structured likewise beginning with droplet impact followed by the film dynamics.

This work continues the work of other scientists in our group of whom Sebastian Baumgärtner contributed a major part with his diploma thesis. He investigated the motion of small beads on SmA films and started first experiments with droplets in those films. My thesis proceeds to give a more detailed analysis of droplets in freely suspended SmA films and moves on to the investigation of the more complex SmC films.

During my time in Magdeburg, I have worked on various projects beyond the scope of this thesis. About one year was dedicated to experiments in weightlessness which were related to liquid crystal experiments on the international space station within project OASIS (Observation and Analysis of Smectic Islands in Space). The preparation and execution of these experiments were one of the most impressive experiences in my life. Unfortunately, the data gathered in weightlessness on parabolic flights were not as well defined as the experiments on ground using the same setup. Thus, they have been excluded from the thesis.

Acknowledgements

This work was financially supported by the DFG (project STA 425- 28) and the German Space Administration, DLR, project OASIS-CO.

I am very much indebted to my advisor Ralf Stannarius for believing that I could successfully combine my chemical background with the physical projects of this thesis. He was always encouraging to explore new fields and think independently. Thanks to him, I had the opportunity to participate in zero gravity experiments and work on several different projects apart from the presented study.

My enthusiasm for the field of liquid crystals was first induced by Jan Lagerwall. He gave an inspiring lecture with plenty of hands on tasks that simply would not allow me to fall asleep. He also introduced me to the world of international research when I was a student at Martin Luther University in Halle. The interest in colorful textures and unique pattern formations was greatly nourished by a participation in the liquid crystal summer school. Apart from many interesting talks, I was impressed by a presentation on the possibilities of microscopy and conoscopy by Daniel Krüerke. The acquired knowledge helped me throughout the entire time of my research. I also want to thank Eva

Enz, Stefan Schymura, Hsin-Ling Liang and Martin Kühnast for being collaborative and reliable. Thanks to a culture of open, enthused discussions and a great work atmosphere I have come to appreciate liquid crystal research and moved on to write my thesis in this area.

I want to thank Thomas John who was a very welcoming when I first started my work in Magdeburg. He introduced me to MatLab based image analysis and taught me how to be resourceful in designing new experimental setups with limited equipment. When he left the group, Torsten Trittel never hesitated to help me when I lacked knowledge of engineering or I needed some advise. His uncomplicated manner lightened every complication and I enjoyed working with him on the parabolic flight campaigns. I need to thank Alexey Eremin for numerous discussions and the introduction to new measuring techniques like fluorescence microscopy. Furthermore, I am always happy to remember the lunch breaks and dinners with Tanya Ostapenko, Gabriela Tamba, Nerea Sebastian and other colleagues of the group. They were always helpful in discussing new solutions for daily challenges. I especially have to thank Tanya for taking time to proof read some parts of this thesis and being an ambassador of motivation. Jürgen Weißenborn, head of the mechanical workshop of the physical institute, and his experience was very important in designing efficient experimental setups.

During my time as Ph.D. student, I had the chance to work with different groups all over the world. At the University of Colorado in Boulder, I had the chance to work with Cheol Soo Park and Zhiyuan Qi in the group of Noel Clark where I could improve my understanding of smectic films and work with high-vacuum setups. Joseph Maclennan was always interested in the work progress and a very focused partner in discussions. The pleasant work atmosphere was very memorable. I want to thank Yuka Tabe for the opportunity to spend two months in her group at Waseda University in Tokio. She took good care of me far in excess of our work. I am also grateful that Takemi Yamane dedicated a major part of his time to helping me assembling the setup. In the group of Agnes Buka in Budapest, I spent only two weeks. However, I am thankful to the Péter Salamon and Tamás Viscek who broadened my knowledge about liquid crystals in magnetic fields and let me contribute to a study on flexoelectric effects.

I want to thank my flat mates Jakob Schweizer and Thomas Ehrling for filling our flat with life. I am especially grateful to Jakob Schweizer who took it upon himself to check the comprehensibleness of the introduction which is outside of his subject area. My family and friends have accompanied me though these years in Magdeburg. I want to thank my mom for keeping up the hopes and her constant support. I want to thank my dad for driving the extra mile and helping me out when I needed a quick craftsman. I want to acknowledge my cousin Luise Dölle for proof reading some sections of the thesis.

I am truly grateful for the curiosity that my uncle and god father Jürgen Reichstein piqued in me. Until he passed away this year, he was always faithful and interested in my work. His background support gave me the necessary patience to finish this thesis. My grandparents Clemens and Waltraud Dölle were always offering help and the calm place for writing was well appreciated. I am very grateful for my large family who rooted for me the entire time. Finally, I thank Anton Niadzelka for his support when I needed time to work. He and our daughter spent long hours in parks and playgrounds while I was writing. Additionally, his relaxed way of dealing with challenges had such a positive influence on my motivation as I had to embrace a bit by bit progress. There are many more who have supported me during my time as Ph.D. student and I want to express my gratitude for helping me along way.

September 25th, 2017

Sarah Dölle

Chapter 1

Introduction

1.1 Basics of Liquid Crystals

Since the discovery of liquid crystals (LCs) by Friederich Reinitzer [5] and Otto Lehmann [6] around 1890, the research has advanced greatly. From an insignificant subject, interesting to a small group of scientists, it developed to a corner stone of soft matter science and various applications. The best-known is the Liquid Crystal Display (LCD) which is ubiquitous nowadays and has great economic value. Apart from commercial applications, liquid crystallinity has always been a fundamental pillar of life itself since biological membranes and cell walls are partly built up by liquid crystalline phases. The term *liquid crystal* describes aggregate states that are found for certain materials on the transition from solid to liquid [7]. These intermediate states of matter are also called mesomorphic phases or mesophases (Greek: *meso* - middle).

Defining basic characteristics of liquids and crystals will subsequently benefit the understanding of liquid crystals. The crystalline state is commonly distinguished by a rigid positional and orientational long-range order. More specifically, the centers of mass of the molecular units are arranged on a three-dimensional periodic lattice and the units are oriented macroscopically. This well defined long-range order is responsible for the anisotropy of the crystal. When the crystal melts into an isotropic liquid, the long-range order of the molecules is lost. The molecules in an isotropic liquid may be characterized only by a short-range order of position and orientation. Additionally, the molecules are able to diffuse freely. In other words, a given particle pattern at point x_0 does not imply any probability of finding a particle at another location far from x_0 apart from the average particle density. The term *isotropic* describes any property that is invariant in all spatial directions and it applies to media like gases, amorphous solids

or normal liquids. Henceforth, if a property is anisotropic, it depends systematically on the direction of investigation.

Liquid crystalline phases exhibit a liquid-like order in at least one spatial direction and show some degree of anisotropy. The orientational long-range order is preserved, whereas the positional long-range order is lost completely or at least in one spatial direction. Even if the positional long-range order is entirely lost, the orientational long-range order suffices for the appearance of anisotropic properties. Depending on the degree of positional order, liquid crystals are known in the form of nematic, smectic or columnar phases.

nematic	orientational but no positional order
smectic	orientational order and long-range positional order in one direction of space
columnar	orientational order and long-range positional order in two directions of space

The molecular units that form a mesophase are called *mesogens*. A key feature that a thermotropic mesogen has to provide is a shape anisotropy, namely an anisometry. Different molecule shapes that show liquid crystalline phases have been found, like calamitic (rod-like), discotic (disc-like), sanidic (board-like) or banana-shaped mesogens. For this study, an introduction to calamitic mesogens, as sketched in figure 1.1 will be sufficient. Following a nomenclature of G. Friedel [8], calamitic liquid crystalline phases can be categorized in nematic, smectic and cholesteric phases. More phases, like the blue phase, and many subclassifications have been found until now.

If different mesophases arise within a single compound, these phases will vary in the degrees of freedom in orientational and/or positional order. Two major classes of liquid crystals are known. When a liquid crystalline phase arises by change of temperature, the system is called thermotropic. In analogy to the mesophases, organic molecules which form thermotropic LC phases are also referred to as mesogens. If a liquid crystalline phase is induced by addition or subtraction of solvent, the system is called lyotropic [9]. However, lyotropic liquid crystals will not be discussed since they were not requisite for this study.

1.1.1 The Nematic Mesophase and the Director Concept

The simplest liquid crystalline mesophase is the nematic phase (abbreviated N), cf. figure 1.1. It possesses no positional long-range order but an orientational long-range order in one spatial direction. In the case of calamitic (rod-like) molecules, a nematic phase is formed by a local arrangement of molecules where the long axes of the molecules

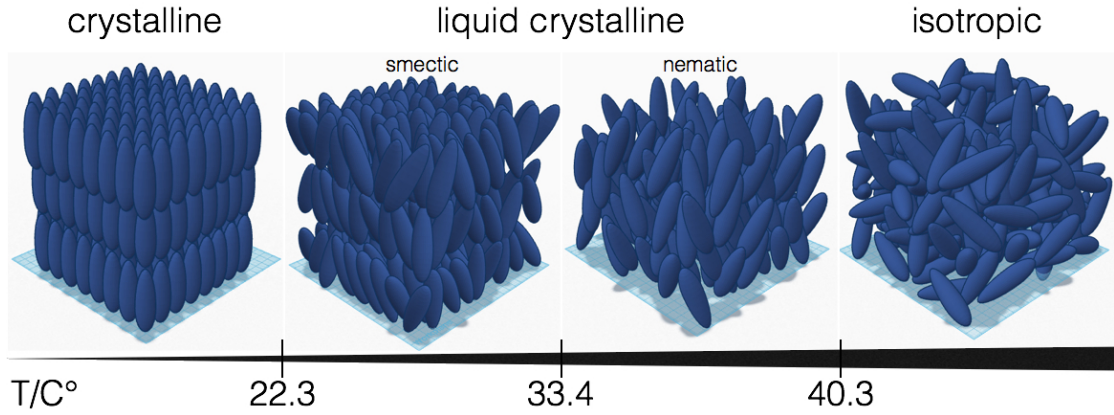


FIGURE 1.1: Schematic representation of the phase diagram of thermotropic liquid crystal 8CB (*4'-n*-octyl-4-cyano-biphenyl). With increasing temperature, the crystalline phase transforms into the smectic and nematic liquid crystalline mesophases and finally into the isotropic phase. Each ellipsoid unit sketches a calamitic molecule.

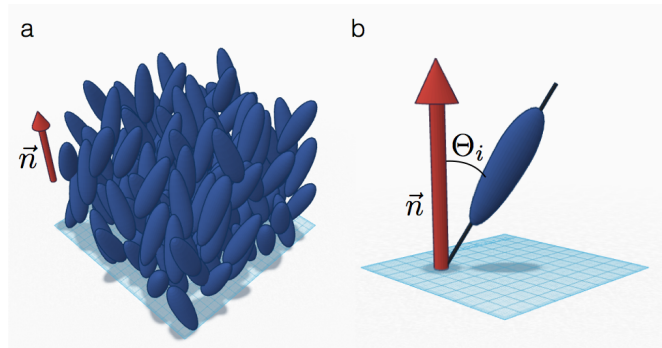


FIGURE 1.2: (a) Schematic sketch of a nematic phase. The arrow indicates the orientation of the director \vec{n} . One ellipsoid represents one calamitic molecule. (b) The polar tilt angle Θ_i of an individual molecule is displayed with respect to the director \vec{n}

are on average parallel to each other. The only difference to an isotropic phase is the orientation of the molecules along this common axis. The axis is denoted by the unit vector \vec{n} , referred to as the director, cf. figure 1.2. The sign of the director has physically no significance for non-ferroelectric LCs, $\vec{n} \equiv -\vec{n}$.¹ A nematic phase is strictly apolar in its orientation, which applies even to N phases with polar molecules.

A distinction between an isotropic and a liquid crystalline phase is found in the degree of orientational order, which is described by the order parameter S , cf. equation 1.1. The parameter quantifies the mean deviation of the designated molecule axis from the common orientation axis. The tilt angle Θ_i is a measure for the angle between the individual molecule and the director as depicted in figure 1.2(b).

$$S = \frac{1}{2} \cdot \langle 3\cos^2\Theta_i \rangle \quad (1.1)$$

¹Ferroelectric LCs are chiral substances formed by mesogens with a permanent dipole moment. The orientation of the dipole moment in a chiral smectic SmC^* phase results in a ferroelectric polarization.

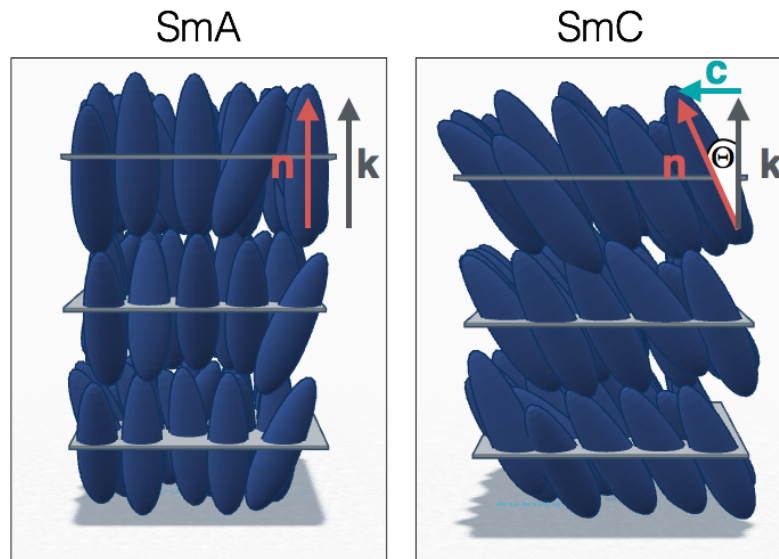


FIGURE 1.3: Schematic sketch of a SmA and a SmC phase. The director \vec{n} is displayed along with the layer normal \vec{k} . For the SmC phase the over all tilt angle Θ is displayed with the \vec{c} director. As a guide for the eye, the average center of gravity of the molecules within one layer is indicated by an intersecting sheet.

Considering an ideally oriented crystal, the order parameter reaches $S = 1$. In contrast, isotropic liquids would yield $S = 0$. Nematic liquid crystals show order parameters of $0.4 \leq S \leq 0.8$ [10].

1.1.2 Smectic Mesophases

The mesophases mainly dealt with in this thesis are smectic phases (abbreviated Sm). In contrast to the nematic phase, the smectic phases show a positional long-range order. Many types of smectic phases are known [11]. However, only two types of smectic mesophases are of importance to this study: the SmA phase and the SmC phase, see figure 1.3. Here, the positional order is limited to only one dimension resulting in a layered structure.

In a SmA phase, the molecules are arranged in layers and oriented parallel to each other with their long axis aligned perpendicular to the layer plane. The molecules are free to rotate around their long axis. They may also tilt slightly and precess on a cone. However, within this precession, no preferred angle can be found for SmA phases. The molecules have high, liquid-like mobility along the layers.

SmC phases are just like SmA phases arranged in layers and the molecules are free to rotate around their long axes. The long axes of the molecules are on average tilted by Θ with respect to the layer normal \vec{k} . This mean tilt is correlated across the layers. The preferred direction of the molecules can also precess on a cone but they show a

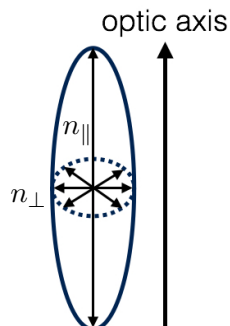


FIGURE 1.4: Schematic of an index ellipsoid with the refractive indices n_{\perp} and n_{\parallel} . An index ellipsoid sketches the refractive index in different directions in space. The optic axis of the ellipsoid, which is drawn next to the ellipsoid for better visibility, lies along its rotational symmetry axis.

preferred azimuthal angle on this cone (cf. angles in figure 1.7). The tilt angle can be temperature dependent. For certain compounds, it can continuously decrease to zero upon heating, where a transition to the SmA phase occurs.

1.1.3 Optical Anisotropy

Liquid crystalline phases exhibit anisotropic physical properties. Apart from optical anisotropy, one can find anisotropic behavior for example in diffusion, electrical and thermal conductivity, magnetic response and flow dynamics.

Considering light as a wave constituted by an electric and a magnetic oscillating field that run orthogonal to each other, the refractive index n is a measure for the compression of the wave length in a certain medium with respect to vacuum. Isotropic materials like water or air can be described with one refractive index. At least two refractive indexes are at least necessary for a precise characterization of rod-like liquid crystals. The refractive index parallel n_{\parallel} and the refractive index orthogonal n_{\perp} to the long axis of the director are not equal. The magnitude of their difference is called birefringence Δn , see equation 1.2 .

$$\Delta n = n_{\parallel} - n_{\perp} \quad (1.2)$$

Calamitic LCs usually show $\Delta n > 0$, which is described as optically positive. Furthermore, SmA phases are optically uniaxial, i.e. a rotation around the long axis of the molecule has no impact on n_{\perp} (and on n_{\parallel}) [12]. This axis allowing a free rotation without changing any optical properties is also called optic axis. Even though, SmC phases are biaxial with three different refractive indexes they may be approximated as uniaxial for our purposes. Uniaxial materials are often simplified by an index ellipsoid as seen in figure 1.4 to the left [13].

The effective optical anisotropy depends also on the angle of the light wave towards the material and may be described better by the ordinary refractive index n_o and the

extraordinary refractive index n_e . Light waves propagating through the medium with a polarization in the same plane as the optic axis experience the extraordinary refractive index, which is identical with n_{\parallel} if the propagation direction is perpendicular to the optic axis. If the optic axis is slightly tilted towards the incident light, only part of the refractive index n_{\parallel} takes effect, and the extraordinary refractive index n_e is reduced. Light with a polarization perpendicular to the optic axis will experience the ordinary refractive index which is equal to n_{\perp} . If the light propagates through the medium along the optic axis, only the ordinary refractive index n_o is effective and no birefringence can be found.

Hence, the polarization of light can change if it propagates through a birefringent material. A standard way to detect birefringence is an illumination of the sample with linear polarized light and a subsequent test if the polarization is changed. The incident light can be polarized by a polarizer filter. Considering the case that the sample is not changing the polarization, light rays would be blocked completely by a second polarizer filter if the second polarizer is rotated by 90° towards the first one [14]. The second polarizer is also referred to as analyzer. Sets of two linear polarizer filters rotated by 90° to each other are called crossed polarizers. However, if the sample material is birefringent, the incoming polarization could be altered, assuming the light experiences the extraordinary refractive index. Thus, the light passes the analyzer and the sample appears bright.

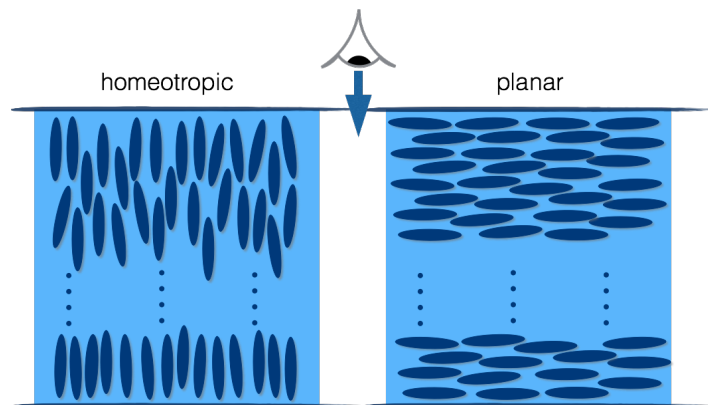


FIGURE 1.5: Homeotropic and uniform planar alignment of calamitic mesogens in the N phase. The dark boundaries above and below the material are potentially glass substrates. The arrow indicates the direction of investigation.

Two different orientations of calamitic mesogens in the nematic (N) phase are shown in figure 1.5. Besides the depicted homeotropic and uniform planar alignment, other orientations like degenerate planar or tilted homeotropic anchoring are possible. These macroscopic alignments are well known for liquid crystals confined between substrates. A special surface treatment of the substrates directs the desired alignment of the molecules. If the orientations in figure 1.5 were analyzed between crossed polarizers, the homeotropic

alignment would appear dark, the planar alignment possibly bright. The homeotropic orientation is also often found for free surfaces of calamitic mesogens, which will be shown for freely suspended SmA films in section 1.1.5.

1.1.4 Viscosity

In bulk samples, the shear viscosity appears as an average over all domains of the mesophase. However, the viscosity of liquid crystals is anisotropic on a nanoscopic scale and depends on the angle between director and shear direction. A macroscopic anisotropy of the viscosity is found when the director is aligned over a larger area. This occurs for example in small restricted systems where surface anchoring dictates the molecular orientation. Such restricted geometry may be found in freely suspended smectic films (c.f. section 1.1.5) with layers oriented parallel to the surface.

The hydrodynamic theory of nematic liquid crystals was treated by Erickson [15] and Leslie [16, 17] for laminar flow fields. Their findings include the determination of the shear viscosity $\eta(\Theta, \Phi)$ for arbitrary director orientations:

$$\begin{aligned} \eta(\Theta, \Phi) = & \alpha_1 \sin^2 \Theta \cos^2 \Phi \\ & + \frac{1}{2}(-\alpha_2 \sin^2 \Theta \cos^2 \Phi + \alpha_3 \cos^2 \Theta \\ & + \alpha_4 + \alpha_5 \sin^2 \Theta \cos^2 \Phi + \alpha_6 \cos^2 \Theta). \end{aligned} \quad (1.3)$$

The dissipative part of the stress tensor contains six constants $\alpha_1 - \alpha_6$ that have the dimension of a viscosity and are known as Leslie coefficients. As shown later by Parodi [18], only five of these coefficients are independent. The Leslie coefficients are required for any calculation of the director rotation or flow. Viscosities η_i and γ_1 can be obtained following equation 1.4, if Θ and Φ in equation 1.3 are chosen according to figure 1.7.

$$\begin{aligned} \eta_1 &= \frac{1}{2}(\alpha_3 + \alpha_4 + \alpha_6) \\ \eta_2 &= \frac{1}{2}(-\alpha_2 + \alpha_4 + \alpha_5) \\ \eta_3 &= \frac{1}{2}\alpha_4 \\ \gamma_1 &= \alpha_3 - \alpha_2. \end{aligned} \quad (1.4)$$

The viscosities in equation 1.4 are the basic viscosity coefficients for the nematic mesophase. They were defined by M. Miesowicz [19] for a fixed director field.

- η_1 - director \vec{n} parallel to gradient of flow
- η_2 - director \vec{n} parallel to flow direction
- η_3 - director \vec{n} perpendicular to velocity and perpendicular to gradient of flow

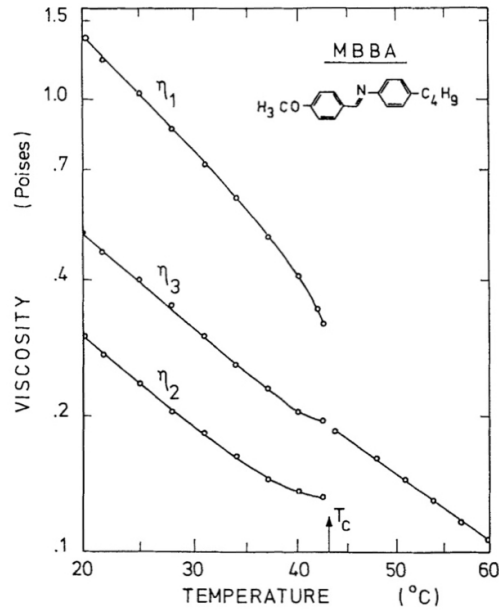


FIGURE 1.6: Miesowicz viscosities of MBBA. The temperature is linear in $1/T$. Taken from Gähwiler, 1973 [22].

In the original paper, the first two definitions of η_1 and η_2 are interchanged. The definitions presented here have been retained from Helfrich [20, 21].

In figure 1.6 the three viscosities η_i of MBBA (N-(4-Methoxybenzylidene)-4-butylaniline) are plotted as a function of the temperature. While η_3 appears to be nearly a continuation of the isotropic viscosity, η_2 and η_1 differ notably. Shearing the sample along the director requires less force than shearing it perpendicular to the director. The effective viscosity measured for a set director alignment at angles Θ and Φ is given by:

$$\eta(\Theta, \Phi) = (\eta_1 + \eta_2 \cos^2 \Theta) \sin^2 \Theta \cos^2 \Phi + \eta_2 \cos^2 \Theta + \eta_3 \sin^2 \Theta \sin^2 \Phi. \quad (1.5)$$

Angles Θ and Φ are defined in figure 1.7.

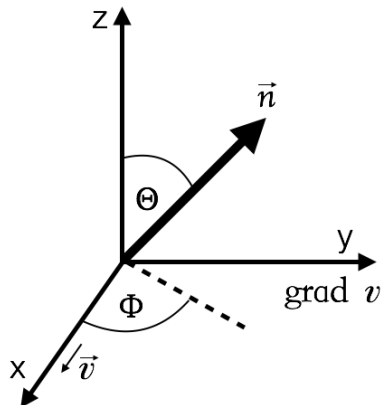


FIGURE 1.7: The orientation of the director \vec{n} is defined by the tilt angle Θ and the azimuthal angle Φ with respect to the flow velocity \vec{v} .

If the director has a component in the shear plane, the viscosity coefficient η_{12} needs to be considered as well. Viscosity η_{12} is largest when the director lies at an

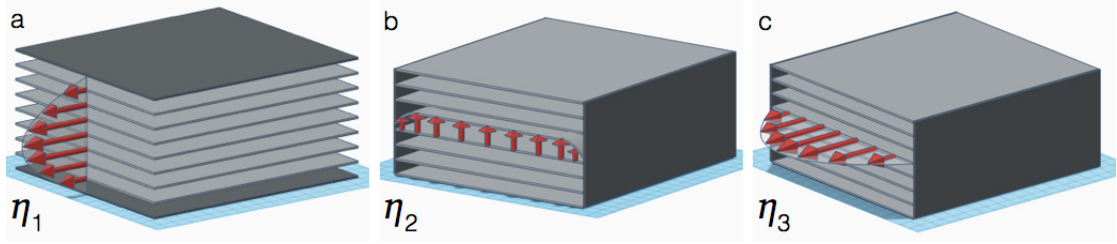


FIGURE 1.8: Schematic sketch of flow fields in a **SmA** phase between two parallel plates (dark-gray). The arrows indicate the flow velocities. The director is aligned parallel to the arrows in figure part (b). Adapted from Schneider et al. [23]

angle of 45° between the flow and the flow gradient. In this case, the viscosity follows $\eta_{45^\circ} = \frac{1}{2}(\eta_1 + \eta_2) + \frac{1}{4}\eta_{12}$ [22]. If the condition of a fixed director field is set aside, also the rotation of the director must be considered. Additional to the Miesowicz coefficients and η_{12} , the rotational viscosity γ_1 is required to form a complete set of coefficients that allow the description of a nematic liquid crystal.

In smectics, the exact description of the viscosity becomes more complex. Experimentally, it is not trivial to measure the viscosities due to the difficulties in controlling the director and avoiding disclinations. Fortunately, in the form of freely suspended films (c.f. section 1.3), smectic materials exhibit a more defined director field. For our purposes, it will be sufficient to describe a freely suspended smectics film as a "quasi 2D" nematic.

Three different shear scenarios between parallel plates are shown for a **SmA** phase in figure 1.8. These are the simplest shear scenarios which correspond exclusively to either η_1 , η_2 or η_3 . In figure 1.8(a), the velocity gradient is oriented parallel to the director which refers to viscosity η_1 . The molecules move normally to the director along with their neighbors in the same layer. This motion can be thought of as a gliding of layers on each other and is highly improbable to occur in freely suspended films. In figure 1.8 (b), a flow perpendicular to the layers and parallel to the director is indicated which corresponds to viscosity η_2 . This requires the permeation of molecules through the layers. A flow of molecules between layers is negligible in the present study. Hence, viscosity η_2 does not give a contribution as well. The viscosity η_3 impacts the motion perpendicular to the director with a velocity gradient parallel to the layer, as depicted in figure 1.8(c). The molecules move perpendicular to the director along with their neighbors in the adjacent layers. This type of flow may be found in freely suspended films.

The in-plane motion of a large particle embedded in a freely suspended film causes a flow exclusively parallel to the film. Though the molecules are linked with neighboring molecules in adjacent layers, they remain in their layer and move solely within the x-y plane. Along the director (along the z-axis), the material appears like an isotropic liquid.

Thus, a freely suspended SmA film is regarded a good approximation to an isotropic liquid in two dimensions. Mobility investigations of inclusions in freely suspended SmA films are a feasible method of obtaining η_3 . The viscosity η_3 can also be determined by observing the motion of islands (cf. section 1.1.5) on a freely suspended film as done by F. Schneider [24].

Considering a freely suspended SmC film, the complexity increases due to the additional SmC director \vec{c} . The model in figure 1.8 may only be regarded as a rough approximation since it was developed for SmA materials. The viscosities η_1 and η_2 would give no substantial contribution as well and η_3 controls the mobility of the motion of an embedded inclusion in the film plane.

In a first approximation, three cases can be distinguished for η_3 . Firstly, there is the case when \vec{c} is parallel to the flow. The second case is found when the SmC director \vec{c} is perpendicular to the flow. And a third case arises for the rotation of the \vec{c} director around the layer normal \vec{k} . The case of an orientation of the SmC director \vec{c} perpendicular to the flow and the gradient does not exist since the director is restricted to the x-y plane. A view along the layer normal \vec{k} offers a simplification approach, where the SmC director \vec{c} may be interpreted as the director \vec{n} of a nematic phase. Considering nematics, these cases would correspond to η_1 , η_2 and γ_1 . Hence, a freely suspended SmC film may be approximated by a 2D nematic, where due to the lower dimensionality not all nematic viscosities are relevant. This model oversimplifies the viscous behavior of SmC films, yet still provides a reasonable approximation for tilt angles Θ smaller than 20° . Further discussions are beyond the scope of this work. A theoretical description of the flow behavior of the SmC phase is given by Carlsson, Leslie and Clark [25].

1.1.5 Freely Suspended Smectic Films

Freely suspended films (FSFs) are well suited to investigate fluid dynamics in quasi two-dimensional systems [26, 27]. Furthermore, they have a large surface to volume ratio which make them ideal systems to investigate surface and interface properties.

The smectic phase forms freely suspended films of remarkable stability. Such films can be drawn when a smectic material is smeared over a hole in an object plate. They are relatively robust even when extremely thin [28]. Films created this way are mostly thinner than $10\ \mu\text{m}$. The layers of the smectic phase are oriented parallel to the film plane, see figure 1.9. The film thickness d is always a multitude of molecular layers. Though, also film thicknesses of only a single layer may be stable. When treated carefully, films can persist several hours or even up to days. This is clearly very different from soap or ink films. They are greatly affected by drainage of the solvent which leads

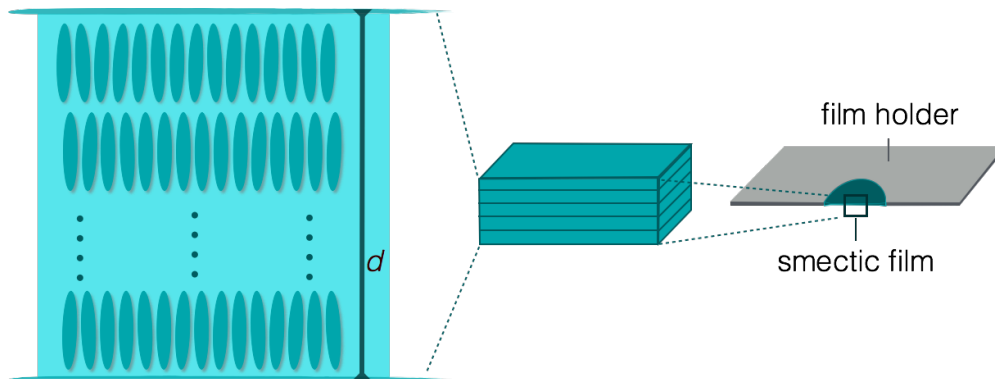


FIGURE 1.9: Sketch of a freely suspended smectic film (SmA). To the right, the film is depicted with the film holder. The FSF spans the hole inside the film holder. The middle segment of the figure shows the layered structure within the film. To the left, the orientation of the molecules in the layers is shown for a smectic A phase.

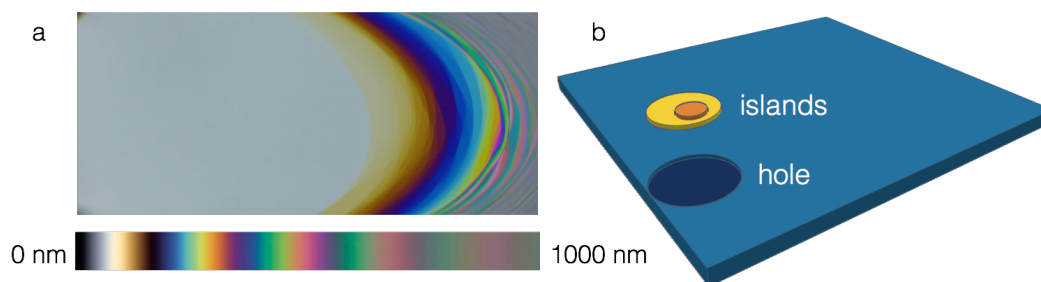


FIGURE 1.10: Image of a SmA FSF. (a) The picture was taken using reflected light microscopy. The white area is homogeneous in thickness. The well-defined areas with different colours on the right side belong to different film thicknesses. The film becomes thicker from left to right. Below the image, a color diagram shows the change of color for film thicknesses from 0 to 1000 nm. (b) A sketch of a freely suspended film with a hole and islands.

to a thinning of the film and finally to rupture. Smectic materials do not require solvent and provide the possibility to work on freely suspended fluid films not thicker than two molecular layers ($\approx 6 \text{ nm}$). The stability can benefit from different attractive forces like van der Waals forces, pi stacking of the aromatic cores and depending on the molecules even polar interactions.

When a film is investigated in reflected light, the film shows bright colors depending on the film thickness as displayed in figure 1.10(a). The colors appear when the film thickness is in the same range as the wavelengths of visible light. Uniform colors indicate uniform films thicknesses. Jumps in film thickness are visible as sharp boundaries between different colors. Also disks of thicker or thinner areas may exist and move on the film. These thicker domains are known as islands [29, 30], thinner domains as holes, see figure 1.10 b.

Looking at the molecules within the layers, a SmA phase shows homeotropic alignment with respect to the surface. Considering light propagating perpendicular through

the film, no effective birefringence is found for **SmA** films. They can be considered quasi-two-dimensional liquids since the fluidity within each layer is liquid-like. This changes when looking at **SmC** films, because the molecules are tilted with respect to the film plane and thus birefringence is detectable. A **SmC** film could be regarded as a polar 2D nematic phase where the \vec{c} director of the **SmC** phase represents the nematic director \vec{n} .

The peculiar stability of these films is based on their layered structure. Continuous thinning of the film thickness in analogy to isotropic liquids is not possible [31]. The formation of a hole is essential for a rupture of the film. Thinning is bound to the creation of a hole within at least one layer. The depth of the hole depends on the number of smectic layers involved. The hole can also cut through the entire film. Interestingly, even when a hole penetrates the film completely, it might still be stable, since holes up to a specific threshold radius R_h tend to heal up and close again. The surface energy E_{surface} that is gained by creating a hole and thus reducing the surface is counterbalanced by the line tension energy E_{line} required for the formation of a new edge, see equation 1.6 [7] and equation 1.7 where σ_{sm} is the surface tension of the liquid crystal, N is the number of molecular layers and d_s is the height of a single layer.

$$E_{\text{line}} = 2\pi\sigma_{\text{sm}}Nd_sR_h \quad (1.6)$$

$$E_{\text{surface}} = 2(\pi\sigma_{\text{sm}}R_h^2) \quad (1.7)$$

The film stability depends on the relation between line tension versus surface energy. Only if the radius of the hole R_h is bigger than a threshold radius, the film will actually break. With $E_{\text{line}} = E_{\text{surface}}$, the critical Radius $R_{h\text{crit.}}$ can be found following equation:

$$R_{h\text{crit.}} = Nd_s. \quad (1.8)$$

When a film is given time to equilibrate usually one distinct film thickness outlasts turbulences and fluctuations. This provides the opportunity of working with a stable film well defined in its spatial dimensions.

1.1.6 π -Walls in **SmC** Films

In freely suspended **SmC** films, π -walls appear as bright or dark stripes between crossed polarizers and are caused by a continuous rotation of the \vec{c} director over a set distance. A half rotation of the \vec{c} director corresponds to a π -wall and, a full rotation to a 2π -wall [7]. The \vec{c} director field is depicted in figure 1.11 for π - and 2π -walls.

When π -walls are observed in magnetic or electric fields, they appear as narrow stripes separating regions of director orientations which are energetically equivalent with

respect to the external field. Without such field, those walls are not narrow and well defined but often broad with a slow gradual change of the director [32].

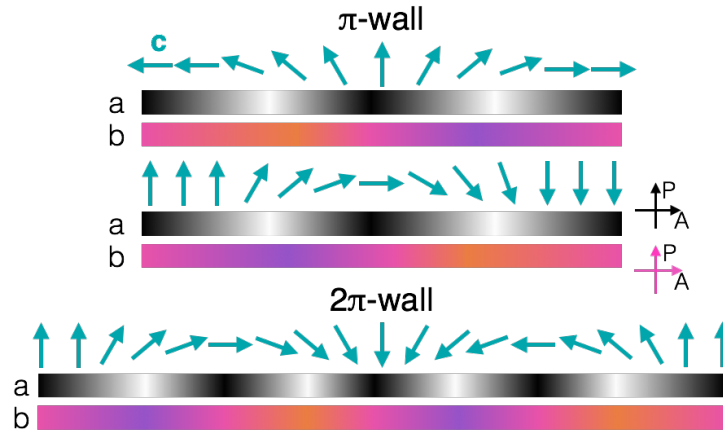


FIGURE 1.11: Schematic of \vec{c} director field for the π - and 2π -walls and qualitative sketches of the optical reflectivity of the SmC film between crossed polarizers (a) and crossed polarizers with λ -waveplate (b).

1.2 Impact Dynamics of Droplets

” In the land of splashes, what the scientist knows as Inertia and Surface Tension are the sculptors in liquids, and fashion from them delicate shapes none-the-less beautiful because they are too ephemeral for any eye but that of the high-speed camera”

— Edgerton and Killian (1954), modified [33]

The phenomenon of droplet impact has been subject to research for more than hundred years. One of the early scientists investigating this topic was Arthur Mason Worthington who published the ”splash of a drop” in 1895. Apart from numerous drawings, he achieved to capture photoengravings of a drop of water falling into a pool of milk. The rapid shape changes of the splash pose a serious challenge to the observer. Worthington solved the problem by illuminating the process by a flash of exceedingly short duration and repeating the experiment with a later onset of illumination time, thus compiling a series of pictures showing the full process [34]. With the development of high-speed imaging [35] the measurability improved greatly and the dynamics of droplet impact were being studied more extensively. During the last century many kinds of liquids, substrates and surfaces have been investigated. An overview of different types of dynamic behavior of droplet impact can be found in a review article by Yarin [36].

1.2.1 Classification through Weber and Ohnesorge Numbers

The Weber number (We) is an auxiliary tool used in fluid dynamics when the flow behavior between two fluids needs to be characterized. It is a dimensionless number following equation 1.9, where σ_d is the surface tension, l is the diameter, ρ is the density and v is the velocity of the droplet.

$$We = \frac{\rho v^2 l}{\sigma_d} \quad (1.9)$$

The We number is expressing the ratio between kinetic and capillary forces determining the driving force of the impact. If $We \gg 1$, impact pressure prevails over capillarity, spreading and splashing becomes likely. When $We \ll 1$, the surface tensions prevents intense deformations.

The Ohnesorge number Oh relates the viscosity η to inertial and capillary forces, cf. equation 1.10. It indicates the prevailing resistance to the process. If Oh is larger than the square root of We or at least larger than 1, the resistance derives mainly from viscous forces.

$$Oh = \frac{\eta}{\sqrt{\rho l \sigma_d}} = \frac{\sqrt{We}}{Re} \quad (1.10)$$

The Ohnesorge number can also be written as a ratio of the square root of the Weber number to the Reynolds number. The Reynolds number relates inertia to viscosity as in $Re = \frac{\rho v l}{\eta}$.

Four different impact regions using Weber and Ohnesorge numbers were described by Schiaffino and Sonin [37]. Figure 1.12 shows a simple diagram of these regions.

Regime (I) — inviscid, impact driven — The dominant driving force is the impact pressure. The flow is resisted primarily by inertia. With $We \gg 1$ and $Oh \ll \sqrt{We}$ the impacting fluid behaves nearly inviscid and shows intense splashing and spreading followed by underdamped interfacial oscillations. The timescale of interfacial oscillations is much longer than the initial spreading.

Regime (II) — inviscid, capillary driven — With $We \ll 1$ and $Oh \ll 1$ the fluid still behaves inviscid but impact velocity generated effects are negligible. The imbalance of the capillary force at the contact line should drive the flow. The spreading is resisted mainly by inertia. In Region I and II viscous forces damp out the oscillations at later timescales.

Regime (III) — highly viscous, capillarity-driven — With $We \ll 1$ and $Oh \gg 1$, spreading is driven by the capillary force. Viscosity effects become more important than inertia effects, resulting in overdamped systems without oscillations.

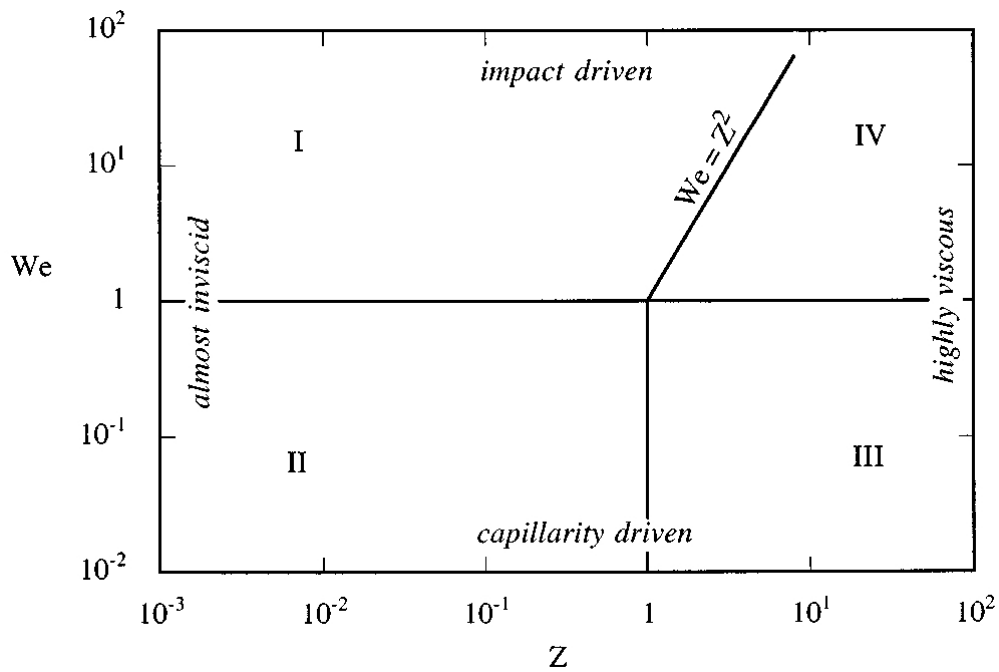


FIGURE 1.12: The four regimes within the $[We]$, $[Oh]$ plane. The Ohnesorge number is named Z in this plot. Taken from Schiaffino and Sonin, 1997 [37].

Regime (IV) — highly viscous, impact-driven— The behavior depends on the dynamic pressure of impact, with $We \gg 1$ and $Oh \gg \sqrt{We}$ and is resisted mainly by viscous shear. Capillarity is negligible and oscillations are absent.

1.2.2 Impact of Picoliter Droplets on Fluid Films

The majority of investigations on droplet impact so far dealt with macroscopic drops. Many studies have been conducted on spreading of droplets for Reynolds numbers between 100–2000 and Weber Numbers between 1 and 400 for droplets of 200–3000 μm in diameter [38–43]. However, the invention of ink-jet printing generated an interest in the fluid dynamics of these small droplets. Since the mechanical energy of the droplet impact changes with the radius to the power of three, the prevailing forces considering picoliter droplets can differ strongly from experiments with larger drops.

The second component when looking at droplet impacts is the target material. Again, a wide range of materials has been tested like wetted solid surfaces [43–46], liquid pools [47–53] or solid surfaces [54–64]. However, a field that has not been investigated in detail before is the droplet impact on free-standing films. This section continues to abstract two works on micron-sized droplets impacting on free-standing films highlighting the challenges in these experiments.

Kim and Wu published an investigations of aqueous droplets tunneling through a soap film [65]. They found that the impacting droplets need a minimum velocity to tunnel through the film. This threshold value is linearly proportional to the film thickness and increases for thicker films. However, the observation system was not able to catch the droplet-film interactions with only 5000 frames per second. Additionally, the image resolution allowed only the determination of the position of the droplet. The shape changes of droplet and film remain in the dark as seen in figure 1.13.

Another study on dispensing small droplets a liquid film was conducted by Do-Quang and co-workers in 2010 [66]. Droplets and film material both consisted of oily ink. They also found threshold energy for the tunneling event. After passing the fluid film, the droplet carried film material. This way a new color printing mechanism was proposed where the color ink is provided in small freely suspended fluid films and the droplet ejected by the print head is only equipped with a transparent carrier fluid. Additionally to the experimental part, a brief analytical model and a more detailed numerical model was employed to understand the puncture and healing process. Though, the images of their experiments could not give sufficient validation of their findings, cf. figure 1.14.

1.3 Inclusions in Smectic Films

Thin smectic films have been investigated in past years for various reasons since the strong impact of surface induced effects and the macroscopically well ordered layer structure provide a unique sample system. Inclusions in these films expand the scope of investigation and application extensively. Inclusions could be e.g. organized on a film using rather low external fields or even self-assembly. Especially, inclusions in SmC films are eligible for self-assembly because of the generated director field distortions around the obstacle. It is known that director field distortions can contribute to alignment effects of inclusions in a bulk SmC phase. But also the weak forces in a FSF can create

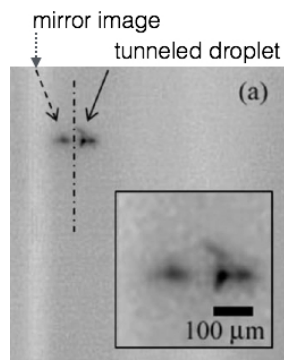


FIGURE 1.13: A water droplet tunneling through a soap film. "Shortly after the impact, an elongated dark region can be identified in (a), showing that the film is stretched by the droplet."

Taken from Kim et al. [65]

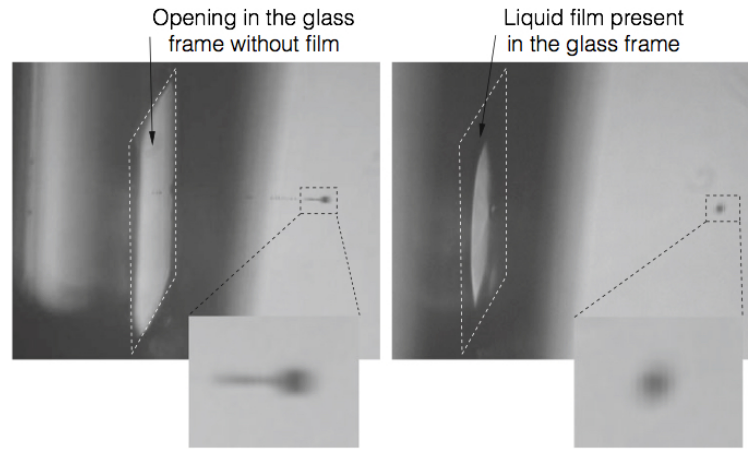


FIGURE 1.14: "Microscope pictures of a dispenser droplet with satellites, ejected prior to filling the frame with a liquid film (left), and a film droplet, i.e. after passing through a free liquid film, under the same dispensing conditions (right)." Taken from Do-Quang et al. [66]

aligned patterns of inclusions, like hexagonal structures or chains [67, 68]. These defined patterns allow new functionalizations.

Furthermore, inclusions facilitate the monitoring of fluid dynamics in FSFs, which show unique properties due to their quasi two-dimensionality. The fluid dynamics will be discussed in an individual section later on. This section will focus on the geometric states and interface tensions of inclusions and surrounding film.

1.3.1 Geometry of Inclusions

If the vertical extension of an embedded inclusion exceeds the film thickness, capillary forces keep the inclusion equatorially fixed in the center of the film plane. Small inclusions that avoid wetting may also sit on top of the film as shown for a Polystyrene bead in figure 1.15. They can be used as tracer particles to investigate the flow field in the film. In the following, only inclusions with diameters bigger than the film thickness will be discussed.

Liquid Inclusions — The shape of a liquid inclusion depends on the surface tensions of the droplet and film material. In contrast to our research, the most investigated liquid inclusions are of the same material as the film. Close to the smectic-nematic or smectic-isotropic phase transition droplets of nematic or isotropic phase may form within the smectic FSF. Figure 1.15 shows a simplified version of different inclusion shapes. For SmA* films of CM11B ((2S,3S)-2-chloro-3-methylpentanoic-acid-[40 -(undec-10-enyloxy)-bi-phenyl]-ester) a lentil-like appearance of the inclusions was stated. Isotropic inclusions of the same material as the film show spherical caps that

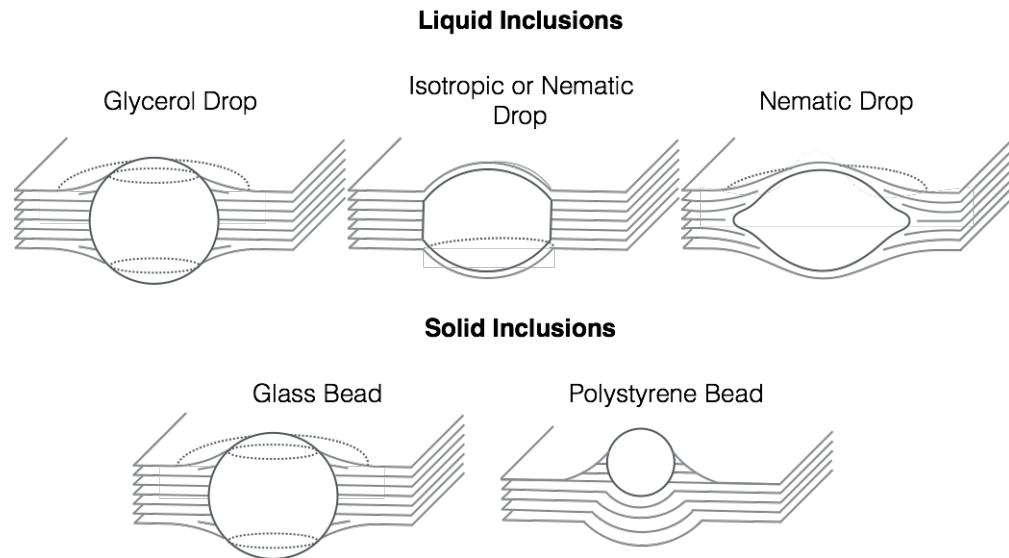


FIGURE 1.15: Different shapes of inclusions in smectic FSFs. Looking at the top row, the Glycerol inclusion was found to be almost spherical in a SmC^* film. Isotropic inclusions, consisting of the same material as the film, show a lentil-like shape with two spherical caps. This was stated for inclusions in SmA^* film. Nematic inclusions may look similar. However, the sketch of the nematic in the top row to the right is a geometry found for a $\text{SmA } 8CB$ film. In the bottom row, the glass bead is embedded in the film surrounded by a wedge shaped meniscus similar to the Glycerol inclusion. Polystyrene beads may float on the film surrounded by a wedge-shaped meniscus. The sketches are adapted from Bohley et al. [69]

stick out the film plane. However, isotropic Glycerol inclusions were found to be almost spherical in a Felix 16-100 SmC^* film [69]. Depending on the size of the inclusion, a large meniscus can build up. It was shown by Dolganov and coworkers, that Glycerol inclusions may diffuse into the film material, dissolving the initial droplet [70]. Nematic inclusions might show a similar geometry as isotropic droplets. This could be assumed by the work of Dolganov, Cluzeau and colleagues [71–75]. Though, it is important to keep in mind that their work dealt mostly with chiral materials and did not actually focus on the three-dimensional geometry of the inclusions. Remarkably, Stannarius and co-workers found a more deformed type of lentil for nematic inclusions in smectic A 8CB films [69]. The cross-section of this inclusions resembles a lemon shape, cf. Figure 1.15.

Solid Inclusions — Solid inclusions like Polystyrene and glass beads have been investigated [76]. Dust particles or small Polystyrene beads may sit on the film whereas bigger particles are usually integrated into the film as shown in Figure 1.15. A wedge shaped meniscus is formed around those inclusions. It may take up to minutes until a stable meniscus is built, depending on the size of the inclusion and the fluidity of the film.

1.3.2 Interfacial Tension of Embedded Droplets

Presuming that the fluids of embedded droplet and fluid film are completely immiscible, the tension between droplet, film and air can be determined by Youngs equation cf. equation 1.11.

$$\sigma_{\text{film}} = \sigma_{\text{droplet}} \cdot \cos\theta \quad (1.11)$$

$$\sigma_{\text{film}} = \sigma_{\text{droplet}} \cdot \frac{a^2 - h^2}{a^2 + h^2} \quad (1.12)$$

Youngs equation can also be expressed in equation 1.12 if the inclusion is composed of two spherical caps [77, 78]. The opening angel 2θ , the height h and the radius a of a droplet are defined in Figure 1.16. For both equations the film thickness is disregarded which is tolerable when the droplet height is much bigger than the film.

1.4 Dynamics in Thin Films

Very thin fluid films can be considered quasi-two-dimensional-systems as aforementioned. Often when downgrading from three to two dimensions the physical description of an event becomes simpler and more evident. On the contrary, theoretical characterization of this system poses a serious challenge as we will see in the following sections. Experimentally, a two-dimensional fluid can be approximated by setting a liquid, thin and freely-suspended film in an evacuated environment. In the two final sections of this introduction we will learn about experimental previous works on thin film dynamics and their limitations.

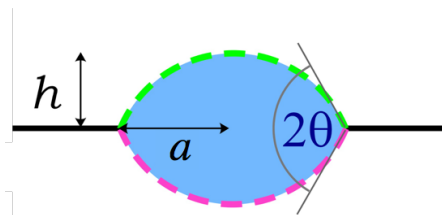


FIGURE 1.16: Sketch of a small droplet embedded in a freely suspended film defining the parameters h (height of the droplet), a (radius of the droplet) and 2θ (opening angle).

1.4.1 The Stokes' Paradox

The fundamental set of equations that describe the dynamics of viscous, newtonian fluids are the named NAVIER-STOKES equations [79]. They were found on the basis of conservation laws and first-order approximations by Claude-Luis Navier and George Gabriel Stokes around 1840. The translational motion in a viscous incompressible fluid is well described by these equations considering the three-dimensional case. Already Sir Stokes found a solution for the case of a sphere in a three-dimensional laminar flow field.

Contrary to intuition, the motion of an infinite long cylinder in an infinitely extended 3D fluid in vacuum does not have a simple solution. The no-slip condition around the moving cylinder requires a motion of the surrounding fluid. At the same time, the motion of the fluid at infinity should be zero. These two conditions cannot be fulfilled in a steady solution. This problem is also known as the Stokes' paradox.

1.4.2 Theoretical Approaches to 2D Fluid Dynamics

In the beginning of the 20th century, Oseen tried to solve this problem by neglecting the inertia term and the instationary term [80]. The solution is valid for boundary conditions close to the cylinder. But the resulting force is a force per length. If one reduces the length of the cylinder, the mobility diverges to infinity. In other words, for a thickness of the fluid close to zero the mobility of the inclusion becomes infinitely large. This leads to the peculiar situation that, in two dimensions, the movement of a disk in a fluid would require no force.

Around 1975, Saffman and Delbrück (SD) investigated the diffusivity of a protein in a thin lipid membrane and developed a full hydrodynamic description of the translational motion of an inclusion in a fluid membrane. They found that not only the viscosity of the membrane η but also the viscosity of the surrounding fluid η' (e.g. air or water) affects the mobility of the inclusion [1, 2]. If the no-slip condition between film and outer fluid should hold, both viscosities have to be taken into account. Saffman stated that even if the viscosity of the surrounding fluid η' might be small compared to the viscosity η of the liquid film, its contribution to the momentum dissipation is still relevant. The relation between the viscosities times the thickness of the film d yields a length, called the Saffman length $\ell_S = \eta d / 2\eta'$. This length can be considered the distance from the inclusion beyond which the fluid flow caused by the moving inclusion can be disregarded. In order to avoid confinement-related shear, the extension of the fluid needs to be much larger than the Saffman length. $\varepsilon = r / \ell_S$ is defined as the reduced radius which needs to be smaller than 1 for finite solutions. For an inclusion radius $r \ll \ell_S$, a finite mobility

b is obtained with equation 1.13, where γ is the Euler constant.

$$b = \frac{1}{4\pi\eta d} \left(\ln \frac{2\ell_s}{r} - \gamma \right) \quad (1.13)$$

Another case, which is experimentally just as important, was approximated by Saffman and Delbrück by simply restricting the system size [2]. If the extension of the fluid film is much smaller than the Saffman length, $R_F \ll \ell_S$, finite size effects cannot be neglected. The mobility b is obtained with the crucial parameter being the radius of the film R_F ,

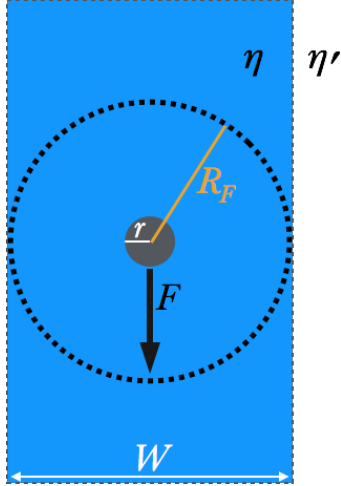


FIGURE 1.17: Sketched top view of an inclusion with radius r in a 2D fluid film. The extension of the film is defined for a circular film with the radius R_F and a rectangular film with the film width W . η is the viscosity of the film, η' the viscosity of the outer fluid.

see figure 1.17 and equation 1.14. For a valid approximation of the mobility, the radius of the circular domain R_F needs to be much bigger than the inclusion radius, $R_F \gg r$.

$$b = \frac{1}{4\pi\eta d} \left(\ln \frac{R_F}{r} - \frac{1}{2} \right) \quad (1.14)$$

Eremin and co-workers published a work on a rectangular geometry of a freely-suspended film [27]. Neglecting the viscosity of the outer fluid, they found a mobility following

$$b = \frac{1}{4\pi\eta d} \left(\ln \frac{W}{2r} + C \right), \quad (1.15)$$

considering an infinitely long rectangular membrane with the width W . The constant C is a geometrical fit parameter $C = -0.88 \pm 0.02$. This empirical relation was tested for a wide range of film widths to be accurate, including the experimental a range of $1 \lesssim W/2r \lesssim 200$.

In 1981, Hughes, Pailthorpe and White (HPW) published an extension of the SD theory for arbitrary inclusion radii and viscosities, where the outer fluid is not anymore restricted to very small viscosities [81]. In the range of $r \gg \ell_s$, they predicted a mobility with 3D-like behavior, which seems intuitive. However, their solution requires difficult numerical calculations. A simple analytical approximation to their model was developed

by Petrov and Schwille (PS) [82] in 2008. For $10 > \varepsilon > 0.2$ the PS solution describes a cross-over from 2D (SD regime) to 3D-like behavior.

Since all experiments in this study have been conducted for $r \ll \ell_S$ in the range of $\varepsilon < 0.1$, the SD solution is considered sufficient for description.

1.4.3 Experimental Approaches to "Quasi 2D" Fluid Dynamics

Experiments approaching "quasi 2D" dynamics have been done on thin liquid films which are often freely suspended but also various types of immersed membranes. Those experiments were analyzed employing the SD-HPW-PS model [26, 83–85]. The dynamics of these systems have been mostly derived from rheology experiments using Brownian motion and the Einstein relation. In the course of these studies, the membrane viscosity [3, 86] or the inclusion size [87] have been extracted from diffusion data.

A study on the dynamics in a smectic freely suspended film (FSF) was published by Eremin and co-workers in collaboration with the group of Noel Clark in 2011 [27]. The method of investigating the diffusion of smectic islands in a FSFs was complemented by experiments of islands and beads moving in a FSF due to gravitation. That way different regimes could be tested. In fact, the whole range from confinement-dominated to air friction regime was spanned. The prediction for the cross-over from confinement-restricted to air-coupling-restricted dynamics at $W/2\ell_s \gtrsim 2.7$ could be confirmed for smectic 8CB (4-*n*-octyl-4-cyanobiphenyl) films.

The publication from Qi et al. [88] went one step further into the exploration of "2D dynamics" by trying to remove the air surrounding the film. They observed the diffusion of oil droplets in a FSF 8CB film at different air pressures. When a film is investigated under high vacuum, it becomes almost a physically ideal two-dimensional Newtonian fluid. The mobility of an inclusion depends on the air pressure and changes from air friction dominated near atmospheric pressure to confinement restricted at high vacuum ($\lesssim 0.02$ Torr). In between those regimes, at a pressure of about 70 Torr the viscosity of air becomes very low. In this cross-over regime, air can be treated as layers slipping over film and inclusion. However, this is directly linked to a film of only a few nanometers. These approximations cannot be extended to thicker films.

Chapter 2

Experimentals

2.1 Materials

Rhodamine 6G <i>M5N</i>	Minimum 99% purity see section 2.1.1	Across Organics from W. Weißflog Halle University
PP1	5- <i>n</i> -Octyl-2-[4-(<i>n</i> -hexyloxy) -phenyl]pyrimidine 100% purity	Synthon (purchased 2010)
PP2	5- <i>n</i> -Decyl-2-[4-(<i>n</i> -octyloxy) -phenyl]pyrimidine 100% purity	Synthon (purchased 2013)
8CB	4'- <i>n</i> -Octyl-4-cyano-biphenyl 100% purity	Synthon (purchased 2012)
Ethylene Glycol	Minimum 99% purity	Merck
Hydrofluoric Acid	Minimum 48% purity	Carl Roth
Glass Beads	"Glasstrahlperlen MGL" Diameters 20-100 μm see section 2.1.2	Eisenwerk-Würth GmbH
Water	Distilled water reprocessed by Milli-Q unit with a conductivity of 590 μS	Merck Millipore

2.1.1 Film materials

Liquid Crystals

Three different liquid crystals, two SmA and one SmC material, served as FSFs. Mixture *M5N* was used in the SmA phase and consists of the following five compounds.

4-hexyloxyphenyl-4'-methoxybenzoate	17.6%
4-octyloxyphenyl-4'-pentyloxybenzoate	24.3%
4-heptyloxyphenyl-4'-hexylbenzoate	10.6%
4-butyloxyphenyl-4'-hexylbenzoate	27.5%
4-nitrophenyl-4'-octyloxybenzoate	20%

The substances were obtained from W. Weissflog, Halle University. A mixture of the first four compounds is known as *Mischung 5*, it exhibits a nematic phase over a broad temperature range [89, 90]. The addition of a certain amount of 4-nitrophenyl-4'-octyloxybenzoate to *Mischung 5* induces a SmA phase which is stable in a wide range above and below room temperature. The mixture was found to age within weeks when exposed to light resulting in a change of color from white to a yellowish brown. The storage of the liquid crystal in an opaque brown container extended the life span notably.

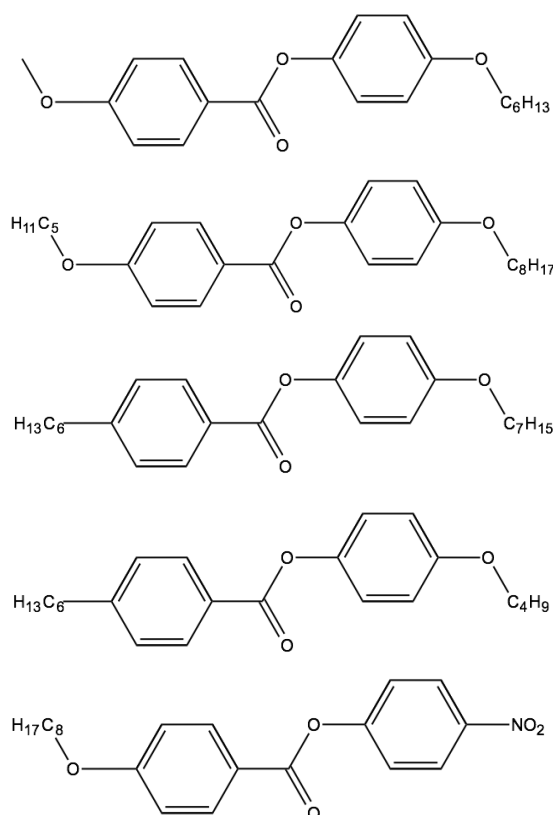


FIGURE 2.1: Chemical structures of all compounds in the *M5N* mixture.

8CB, 4'-*n*-octyl-4-cyano-biphenyl, is a well characterized liquid crystal with a room temperature **SmA** phase. The surface tension of *8CB* with respect to air is $\sigma = 0.0278 \text{ N/m}$ [91].

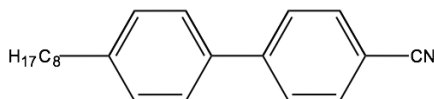


FIGURE 2.2: Chemical structure of *8CB*.

SmA	—	N	—	I
	33.8°C		40.8°C	

TABLE 2.1: Mesomorphism of *8CB*

The mixture of equal amounts of 5-*n*-octyl-2-[4-(*n*-hexyloxy)phenyl]pyrimidine (PP1) and 5-*n*-decyl-2-[4-(*n*-octyloxy)phenyl]pyrimidine (PP2) will be referred to as *PP* mixture and was applied in the **SmC** phase.

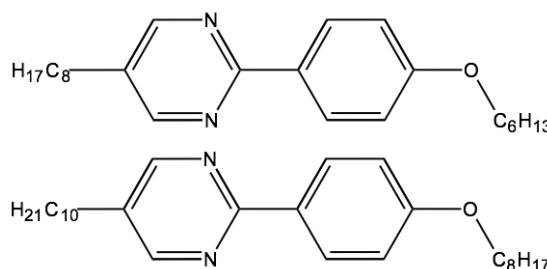


FIGURE 2.3: Chemical structures of compounds in *PP* mixture.

As shown in the table of mesomorphism, the room temperature **SmC** phase is followed upon heating by a **SmA** phase and a nematic phase before the isotropic phase sets in. The surface tension of this mixture with respect to air is $\sigma = 0.02245 \text{ N/m}$ [77].

SmC	—	SmA	—	N	—	I
	52°C		68°C		72°C	

TABLE 2.2: Mesomorphism of *PP*

2.1.2 Inclusion materials

Liquid Inclusions

Aqueous droplets were usually doped with 5 wt.-% ethylene glycol, which was purchased

from Merck with a purity of at least 99%. The droplets were placed on the film via a droplet dispenser creating droplet diameters of up to $50\ \mu\text{m}$. The surface tension of this mixture with respect to air is $\sigma_{\text{droplet}} = 66.38\ \text{mN/m}$ [92]. Few experiments were performed with droplets containing 50 wt.-% Ethylene Glycol. The higher viscosity of this mixture impairs the dispensing feasibility. Thus, a droplet dispenser with an orifice size of $40\ \mu\text{m}$ was used, creating droplet diameters of up to $100\ \mu\text{m}$.

Solid Inclusions

Glass beads with radii from 20 to $100\ \mu\text{m}$ were provided from Eisenwerk-Würth GmbH ("Glasstrahlperlen MGL"). The bead diameters were measured optically with a 20x magnification, which corresponds to a resolution of $0.2\ \mu\text{m}/\text{Pix}$. The uncertainty of measurement was found to be $\pm 2\ \text{Pix}$ at most. Thus, the radii were measured with a certainty of $\pm 0.4\ \mu\text{m}$.

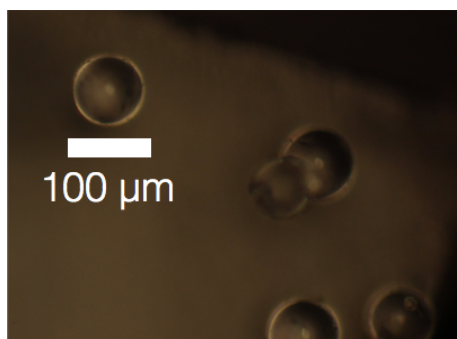


FIGURE 2.4: Microscopy image of glass beads at the edge of the film holder with a resolution of $0.2\ \mu\text{m}/\text{Pix}$.

2.2 Equipment

Droplet Dispenser	Jetting Device MJ-ATP-01	MicroFab Technologies
Spectrometer	UV-VIS Spectrometer BALK-Comet (280-900 nm)	Stellarnet Inc.
Microscope 1	Axioskop 40	Zeiss
Camera 1	Single-lens reflex camera EOS 550D	Canon
Micromanipulator	Manual micromanipulator MM 33	Märzhäuser Wetzlar
Microscope 2	Long-range microscope QM 100	Questar
Camera 2	High-speed camera Phantom V611	Vision Research
Microscope 3	Axio Imager A1 microscope	Zeiss
Camera 3	AxiocM HR	Zeiss

2.3 Sample Preparation and Setups

Firstly, the droplet dispenser and its special features are discussed. Secondly, the preparation of samples are presented along with the corresponding setups used in the respective experiment. An important part of this work was the development of the vertical film setup and the droplet impact setup. The tilted microscope setup is a tuned reflected-light microscope frequently used in the Stannarius group.

2.3.1 Operating the Drop-on-Demand Dispenser

The drop on demand dispenser is a single jet dispensing device for small volumes in the picoliter range. There are different types of dispensing systems, like printheads with conducting or ultrasonic nozzles. The system used in this study is based on piezoelectric printing, see figure 2.5. The dispenser creates droplets via a piezoceramic nozzle. The



FIGURE 2.5: Sketch of the dispenser model. Image taken from *MicroFab Technologies*.

ejection process depends solely on the mechanical force propagating to the orifice due to an electric pulse. The applied wave function is shown in figure 2.6. A small droplet of defined volume is extruded out of the nozzle at high velocity rates. By choosing the electrical pulse, the ejecting velocity can be modified as well as the droplet size to some extent. The droplet size is usually not larger than twice the orifice diameter. The dispenser can be obtained in different orifice sizes. Most experiments were performed using a nozzle diameter of about $43\ \mu\text{m}$. Additionally, a slightly larger orifice size was preferred for higher viscosity liquids. A $20\ \mu\text{m}$ nozzle was tested and deemed to clog up too easily. The dispenser was filled by sucking up the liquid through the dispenser nozzle by a syringe which was attached by a silicon tube. This way, larger dust particles cannot enter the dispenser but they still may clog the nozzle. This is prevented by filtering the liquid before filling the dispenser. Filters with a pore width of $200\ \mu\text{m}$ were chosen for sample preparation. When the dispenser is readily filled, a first test is performed by pressing a bit of the liquid out again. If the liquid runs freely in a small jet, the dispenser is ready to be hooked up to the circuit. The jet is very thin and hardly seen by eye. Mostly, only the built up of accumulated droplets on the target material is visible.

Considering the dispenser with the $43\ \mu\text{m}$ orifice, the created droplets have diameters of roughly $40\ \mu\text{m}$. This corresponds to droplet volumes of about $34\ \text{pL}$ and masses of about $34\ \text{ng}$. Depending on the ejected fluid, the droplet size may vary. The droplet velocity is adjusted by the driving voltage applied to the dispenser. The droplet impact

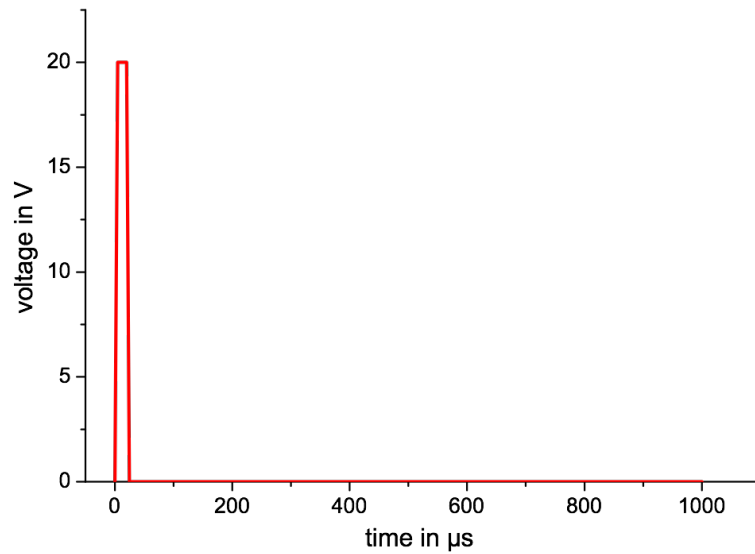


FIGURE 2.6: Function of microdroplet dispenser to eject a single droplet of water. When the viscosity of the liquid to dispense is high, the peak voltage needs to be increased. Voltage peaks of up to 50 V were used with 50 wt.-% Ethylene Glycol droplets. A voltage peak of 20 V is initiated with a ramp up function of $4 \text{ V}/\mu\text{s}$. The voltage plateau lasts for $15 \mu\text{s}$ and is ramped down at $0.66 \text{ V}/\mu\text{s}$.

velocities were derived directly from high-speed imaging. Due to air friction, the impact velocity is substantially reduced compared to the initial ejection velocity.

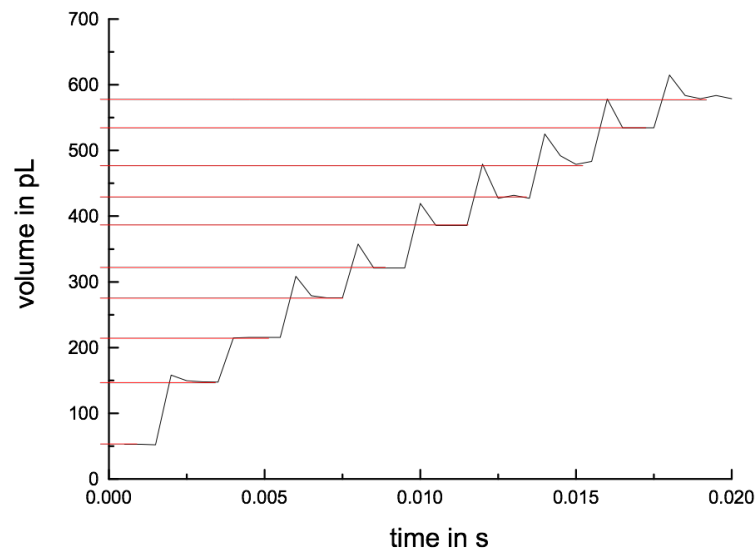


FIGURE 2.7: Volume accumulation of 10 dispensed droplets in a sessile drop over time. The droplets were shot onto a silicon wafer and observed from a side view as shown in figure 3.1. The droplet consists of water and 5wt.-% Ethylene Glycol. The first disposed droplet corresponds to the first horizontal line at about 55 pL . The onset peaks at each step is an artifact, that is based on the tracking method. At the time of merging, the sessile droplet appears too big since a spherical cap is fitted to its surface.

In figure 2.7, the volume increase of a sessile droplet is plotted over time as more

microdroplets are impacting and merging. However, the second droplet carries almost twice the volume of the first one. It was noted that a repeatable droplet size could not be reached for the first two to three droplets. After the third droplet, the volumes become more stable settling at about $55 \pm 5 pL$. Since the reproducibility of the droplet volume is not given for the first droplets, the size of the inclusions in the film were measured individually for each experiment.

2.3.2 Vertical Film Setup

The vertical film setup was initially developed for experiments in weightlessness which required remote control. The data on droplet motion in FSFs in this work were gathered using the vertical film setup as shown in figure 2.8. The setup was built for surveying a larger area compared to the possibilities of a microscope. Hence, a trajectory of 1 cm could be exploited. Furthermore, the spectrometer is able to catch data while recording a movie. The film holder was built by one movable and three fixed razor blades on an aluminum frame. A small amount of liquid crystal was placed along the edge of the fixed blade which is facing the movable one. The films were drawn by the movable razor blade operated via stepper motor. This offers a good control over drawing speed. Mostly, a slower drawing results in thicker films.

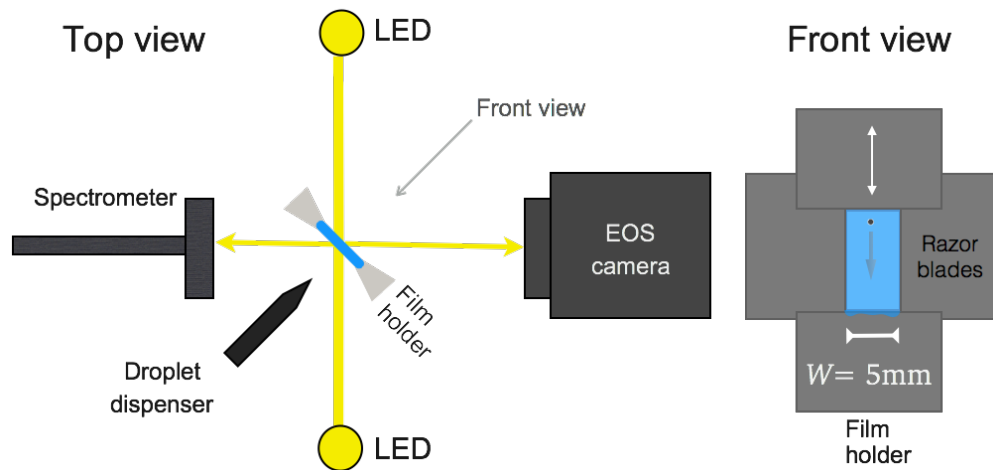


FIGURE 2.8: Schematic sketch of the vertical film setup. Top view: positional arrangement of film holder, spectrometer, LEDs and Camera. The film stands upright in a vertical position. The dispenser places the droplet horizontally on the film. The film is angled at 45° to the incoming light. Front view: schematic of the film holder built by 4 razor blades. The upper blade is movable and spans the film up to 1 cm in height. The lower blade provides a small liquid crystal reservoir. The film width was fixed at 5 mm.

The observation of the inclusion was carried out by a commercial camera (Canon EOS 550) operating with a frame rate of 60 frames per second. Movies of the moving

droplets were taken resolution of $5.5 \mu\text{m}/\text{Pix}$ and a frame rate of 60 frames/s. The illumination was provided by two white LEDs. Movies and spectra were recorded using reflected light, where light source and collecting point were kept at an angle of 90° to each other and at 45° to the film plane. Considering the movies, this setting leads to a reduced area in focus. Firstly, the shutter speed needs to be very short to avoid in-motion blurring. Secondly, the aperture must be wide for good illumination. Both of these features reduce the depth of sharpness to a minimum. Thus, only a narrow pathway in the movie is focused. However, if the droplet is placed correctly, this situation poses no problem and the inclusion stays in focus. Considering the spectra, the setting influences the measured film thickness. Reflected illumination at an angle of 45° yields a film thickness that is reduced compared to the illumination normal to the plane of the film (see measurement of film thickness in section 2.4.1).

2.3.3 Droplet Impact Setup

The droplet impact on a FSF was investigated using the setup shown in figure 2.9. The films were drawn manually on the opening of a glass capillary with inner diameter of about 4 mm. A small amount of material is spread on the capillary opening with a spatula. The film forms when a razor blade is drawn across this opening. The film thickness is estimated from the optical transmission of the film and the reflective interference colors by eye. The thickness is in the range of a few hundred nanometers, not exceeding 500 nm. The FSF is bulged outwards due to subtle overpressure ($\approx 50 \text{ Pa}$) in the capillary until it reaches approximately the shape of a spherical cap. This allows an observation direction parallel to the film plane without the film holder blocking the view. The radius of curvature of the film is roughly 2 mm. Since the diameter of the impacting droplet is below $100 \mu\text{m}$, the mean curvature of the film is therefore negligible for the experiment.

Droplets are shot onto the film by means of the micro-dispenser. A voltage pulse of 22 V was applied for only $5 \mu\text{s}$. Higher voltage peaks (up to 45 V) resulted in larger droplet velocities. However, in many cases small satellite droplets occur at high voltages. The slow limit of the droplet velocity is restricted by the gravitational force and air friction.

The experiments were recorded via long-range microscope (Questar QM 100) combined with a high speed camera (Phantom V611 from Vision Research). Illumination was provided by a 3 A LED focused with a collimator lens. The high-speed camera was employed at a frame rate of 180067 frames per second, which allows to record image sizes of 256×256 pixel. The setting was chosen since higher frame rates can only be

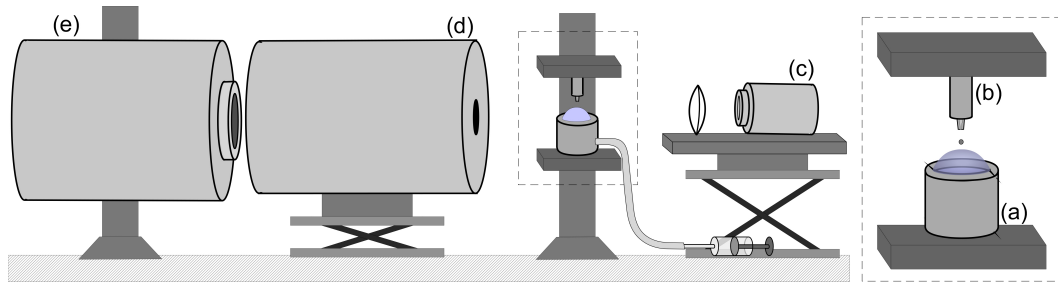


FIGURE 2.9: Schematic sketch of the experimental setup. The opening of a glass capillary (a) is covered with a FSF. The film is bulged by slight overpressure, adjusted manually with a syringe connected to the capillary. A micro-dispenser (b) creates droplets with well-defined size and speed. The droplets are ejected vertically towards the center of the horizontal top of the FSF. An LED lamp (c) combined with a focussing lens is used for illumination. The impact process is recorded by a high-speed camera (e) attached to a long range microscope (d). Taken from Dölle et al. [93]

realized at the cost of a smaller view field resulting in a lower resolution. Moreover, the illumination poses a restrictive feature. The necessary high illumination intensities set the limits to achieve suitable frame rates at the required magnifications and spatial resolutions. The position of the collimator lens needs to be well adjusted for peak illumination at the point of impact.

The evaporation experiments were conducted with a similar setup. Merely the film holder was exchanged with a silicon wafer. The silicon wafer was etched with 5 vol% hydrofluoric acid to remove the oxid layer.

2.3.4 Tilted Microscope Setup

The tilted microscope setup was only used for experiments with solid inclusions in SmC films. The setup was manufactured by mounting the Axioskop 40 microscope on an aluminum plate which is linked to a bottom plate by a hinge-joint. A simplified sketch of the setup is shown in figure 2.10. In some distance to the joint, a lifting platform with a fulcrum lever is fitted between the platforms. The lifter is a simple car-jack with a scissors mechanism. Prior to the experiment, the aluminum plate with the microscope is inclined to the desired angle between $4 - 14^\circ$ by rotating the lever.

The film holder was built by a set of 2 glass slides and 2 movable razor blades as shown in figure 2.11. The width of the film between the two razor blades was varied from 2 to 4 mm, see figure 2.11. The length of the film between the two glass slides was usually about 1 cm. The movable razor blades were pulled by hand via a screwed joint. Mostly only one blade was moved slowly from the liquid crystal reservoir to the desired width of the opening. Since the experiments required thick films, a slow drawing speed of approximately 1 mm/min was targeted. The liquid crystals in these experiments

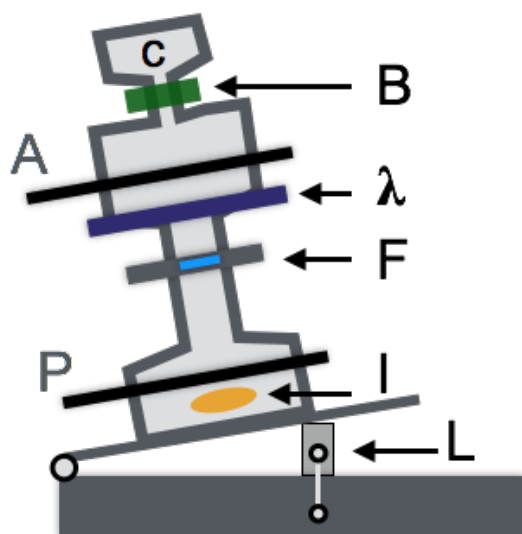


FIGURE 2.10: Simplified sketch of the tilted microscope. The microscope is mounted on a plate, which may be tilted using the lifting platform (L). The images were recorded in transmission. A 100 W halogen lamp was used as illumination source (I). Polarizer (P) and analyzer (A) were crossed at 90° . The film holder (F) with the FSF is placed on an X-Y stage. According to requirements, a λ -wave plate (λ) could be inserted. Experiments were recorded with a camera (C). A spectrometer could be connected via beam splitter (B).

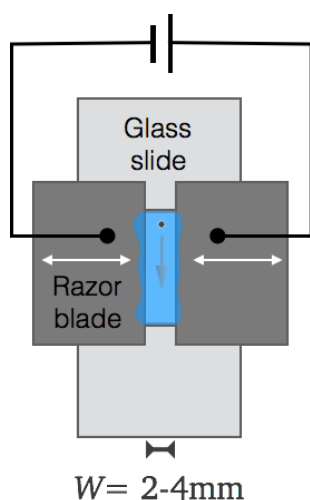


FIGURE 2.11: Schematic of the film holder built by two razor blades and two glass slides. The two blades are movable. Film widths of from 2-4 mm were drawn. The film height was approximately 1 cm. The blades are connected to a circuit with alternating current. Voltages of up to 400 V were applied.

were solely SmC materials. The director orientation could be visualized between crossed polarizers if a certain thickness of the film was given. For sufficient birefringence, only film thicknesses of more than $1 \mu\text{m}$ were probed. The film thickness was measured using the BALK-Comet UV-VIS Spectrometer from *Stellarnet Inc.*, which is integrated into the setup over a beam splitter.

An electric field was applied between the two razor blades in order to manipulate the orientation of the molecules in the film. The director orientation in an AC field was tested, in order to investigate the inclusion mobility with a set director alignment. High voltages of 200 V/mm were required for an aligning effect on the SmC director of the *PP* material. However, due to electrostatic forces, the bead deposition was impossible in such strong fields. All bead motion experiments had to be carried out without field.

Glass beads were placed on the film via micromanipulator. The deposition process requires a glass needle, which was manufactured by pulling out a glass pipette. The glass beads were stored on the film holder near the film. They could be collected with

the glass needle via adhesion. This process is monitored using the microscope Axioskop 40 from *Zeiss*. The extension of the selected bead was then measured before releasing the bead above the film. The bead is launched by a subtle tap on the manipulator. At times, adhesion would prevent the bead detachment. Then, the bead was plunged into the film followed by the retraction of the glass needle. Subsequently, the bead is dragged down the film by gravitational force.

The data were recorded with the commercial single-lens reflex camera EOS 550D from *Canon*. Movies of the moving beads were taken with a 5x magnification, which provided a resolution of $3.2 \mu\text{m}/\text{Pix}$. The frame rate was set to 60 frames/s.

2.4 Measuring Techniques

2.4.1 Measurement of Film Thickness

In 1980, Rosenblatt and Amer published a method to measure the film thickness of a thin film from its reflectivity [28]. This technique has been exploited extensively by researchers investigating FSFs. At normal incident, the reflectivity R of a film is given by

$$R(\lambda_0) = \frac{4\nu^2/(1-\nu^2)^2 \sin^2\varphi}{1 + 4\nu^2/(1-\nu^2)^2 \sin^2\varphi}, \quad (2.1)$$

where φ is the retardance $\varphi = 2\pi n N d_l / \lambda$ and $\nu = \frac{1-n}{1+n}$ [94]. N is the number of layers in the film, λ is the wavelength of light, n is the ordinary index of refraction and d_l is the thickness of one smectic layer.

The reflectivity depends on the interference of light reflected at the upper and lower surfaces of the film. The incident ray is reflected partly at the upper surface as depicted in figure 2.12 in point A and undergoes a phase shift due to $n_0 < n$. The outer fluid is air with a refractive index of $n_0 \approx 1$. The rays that are refracted into the film are reflected and refracted again at the bottom surface of the film. When the reflected rays exit the film in point B, they interfere with rays reflected at the upper surface at a path difference of $\Delta = 2p - \Delta a$. Constructive interference is obtained for

$$\Delta = 2d\sqrt{n^2 - \sin^2\zeta} + \frac{\lambda}{2}. \quad (2.2)$$

This method may be employed using laser reflectivity or white light. The laser method works well for thin films of up to about 100 nm. If white light is applied, the data is usually analyzed via spectrometer. Given a correct calibration, the intensity measured directly from RGB-pixels in images was found to be reliable as well [95].

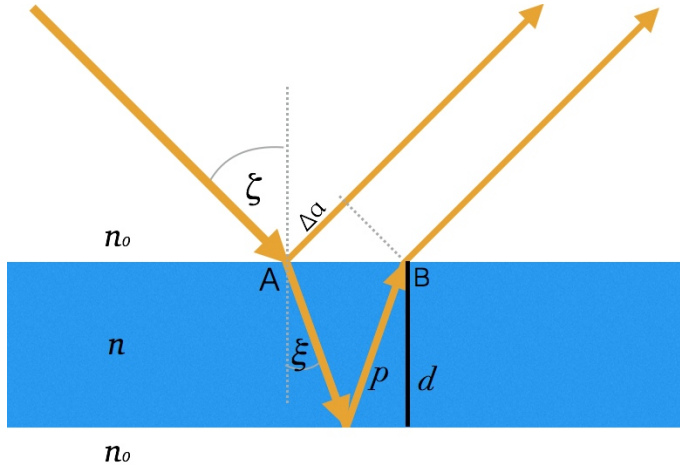


FIGURE 2.12: Sketch of light reflected from a FSF at 45° , where d represents the film thickness and p the pathlength of light. ζ denotes the incident angle, ξ corresponds to the angle of refraction.

For the investigation of flat films in the range of $80 - 5000$ nm, analyzing interference spectra of white light illumination is a well-proven technique. Firstly, a background of the white light spectrum is recorded in reflection by means of a mirror. Secondly, the sample film is illuminated and the resulting interference spectrum is analyzed. In the microscope, the beam is coupled in at normal incident angle. The reflected light is sent to the spectrometer via beam splitter. The reflected spectrum depends on the film thickness and the refractive index of the material. All experiments were conducted at room temperature, ranging from 22° to 27°C within a year. The change in refractive index is insignificant for the investigated temperature range and was disregarded. The spectra were analyzed using a Matlab program written by Alexey Eremin which simulates reflectivities for the given range of wavelengths on the basis of equation 2.1. The spectrum created for a specific film thickness is compared to the experimental spectrum searching for a maximum overlap. Starting from this initial film thickness, a range of film thicknesses is scanned. It is crucial to start the scan for a set of initial film thicknesses since the algorithm is easily stuck at local minima. Experimentally, it is important to record the spectrum for a homogeneous film thickness. Layer steps or islands in the field of view may obscure the spectrum.

The Matlab program generates values for the case of normal incident found in tilted microscope setup. In the vertical film setup, the incident and reflection angle are set to 45° . For a film with a refractive index of about $n = 1.5$, the film thicknesses calculated from the spectra have to be scaled down by factor 0.88 following equation 2.3.

$$d = p \sqrt{1 - \left(\frac{\sin \zeta}{n}\right)^2} \quad (2.3)$$

2.4.2 Determination of the SmC Director

Experiments on inclusion mobilities in SmC films have been conducted using polarizing microscopy. In this setup, two linear polarizers are integrated into an optical microscope. The first polarizer is located between lamp and sample. The second polarizer, also referred to as analyzer, is positioned between sample and observer, as seen in figure 2.10. The setting of crossed polarizers is found when the angle between their transmitting axes is 90° .

Considering a SmA film and normal incident light, a dark state is obtained if the film is positioned horizontally between crossed polarizers. The incident rays experience only the ordinary refractive index of the material since the molecules are oriented homeotropically. If a SmC film is placed between crossed polarizers, the image becomes bright on two conditions. Firstly, the SmC director must not be parallel to the polarization plane of either analyzer or polarizer. The birefringence and thus the intensity of the transmitted light is largest when the optic axis of the sample is at 45° to the incoming polarization of light. Secondly, a certain minimum thickness is required since the effect is small for thin films. The thickness determines how much the phases of ordinary and extraordinary rays are shifted. Only a sufficient phase shift will allow visual detection of the birefringence. For *PP* films, this constrains the thickness to values approximately above 1000 nm.

An optical image of a SmC film between crossed polarizers is shown in figure 2.13. Two defect points are visible in the center of the image. Defects are points of disclination of the SmC director and appear in different strengths. A schematic defects with the strengths -1 and +1 is given in figure 2.14. They hardly differ from each other when either of these structures are investigated between crossed polarizers. While going around each disclination point, the light is blocked four times when the molecules are either parallel to the analyzer or polarizer. Thus, four black stripes originate from the defect point, also referred to as extinction cross. One way to distinguish the defects is by investigating the orientation of the extinction cross. If the cross is not oriented along the polarizer axes, it must be a -1 defect. However, no distinction can be made in a fixed position if the cross is oriented along the polarizer axes. For the purpose of this study, only defects with a strength of 1 will be requisite.

So far, the orientation of the SmC director is not well defined. More information can be gathered using a retardation plate. It is inserted at 45° to analyzer and polarizer. An image with crossed polarizers and additional retardation plate is shown in figure 2.15. The retardation plate allows to distinguish the orientation of the SmC director along the analyzer direction from an orientation along the polarizer direction. The retardation



FIGURE 2.13: Reflective microscopy image of a defect structure in a SmC film between crossed polarizers.

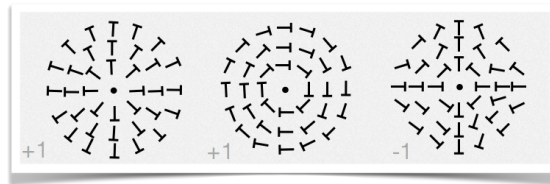


FIGURE 2.14: Schematic of three defects with strength 1. The defect to the left is a radial +1 defect, the center +1 defect is tangential and the defect to the right is a -1 defect.

plate is a birefringent selenite plate which adds a fixed optical path difference of 550 nm to the sample. It is also known as (full) wave plate or lambda wave plate. When the wavefront with 550 nm experiences a phase shift of one complete wavelength, it is absorbed by the analyzer. Thus, the image appears in a magenta color which is a combination of longer (red) and shorter (blue) wavelengths. The direction with high refractive index is indexed slow axis. For optically positive materials, this corresponds to the extraordinary axis.

When the SmC director is perpendicular to the slow axis of the λ -wave plate, the relative retardation decreases. This situation is defined as subtractive position. The wavelength experiencing a phase difference of a full wave length is shifted to shorter wavelengths. Thus, a color in the blue range will be absorbed by the analyzer and the remaining wavelengths combine to a color, similar to a second order blue.

If the SmC director is parallel to the slow axis of the wave plate, the relative retardation increases. A shorter wavelengths experiences a full wave length phase difference and gets absorbed. This situation is defined as additive position. The transmitted red and green wavelengths form a hue close to a first order yellow.

Depending on the thickness of the sample and microscope adjustment the colors may vary slightly. In figure 2.15, the second order blue is shifted to a violet shade, the first order yellow changed to an orange hue.

This knowledge allows to determine the orientation of the SmC director of the bright stripes in figure 2.13. With figure 2.15, a distinction between a radial and a tangential



FIGURE 2.15: Reflective microscopy image of the defect structure in figure ???. The SmC film is illuminated between crossed polarizers with a λ -wave plate. Dashes indicate the orientation of the SmC director around the topological defect.

setting in the defects is accomplished. However, the sense of direction of the black stripes is still unknown. A simple solution to the problem of discrimination of +1 and -1 defects is the rotation of the sample between crossed polarizers. Extinction crosses corresponding to -1 defects will rotate against the actual moving direction. Textures with a strength of +1 will persist in their orientation.

Additionally, a 45° rotation can also be carried out with inserted lambda wave plate. The areas formerly placed in the extinction cross are now susceptible to the investigation with the retardation plate. This second technique of rotation will be applied in section 4.3.

Note that this experimental setup excludes the determination of the sign of the SmC director orientation. Thus, the data will always give two possible results. However, in a FSF, the sign of the SmC director is invertible by looking at the film from below and it does not enter the continuum equations.

2.4.3 Fluorescence Microscopy

An embedded droplet in a FSF forms a meniscus after several seconds. The task of distinguishing the inclusion from the surrounding film was solved by fluorescence microscopy using the Axio Imager A1 microscope. The droplet material was doped with the fluorescent dye Rhodamine 6G, see figure 2.16, c.f section 2.1. An aqueous solution containing 0.1 mg/ml Rhodamine 6G and 5 wt.-% Ethylene Glycol was prepared as inclusion material. The droplets were placed via droplet dispenser on an M5N film (SmA). The dye molecule is sufficiently soluble in water. The addition of a small amount of Ethylene Glycol did not have a noticeable effect on the solubility. The dye has peak absorption at $\lambda_{abs} = 524 \text{ nm}$ and peak emission at $\lambda_{em} = 550 \text{ nm}$. It was excited using a 100 W halogen lamp combined with filter set 09 from Zeiss. The filter allows for excitation in the range from 450 nm to 490 nm . Wavelengths above 510 nm are blocked.

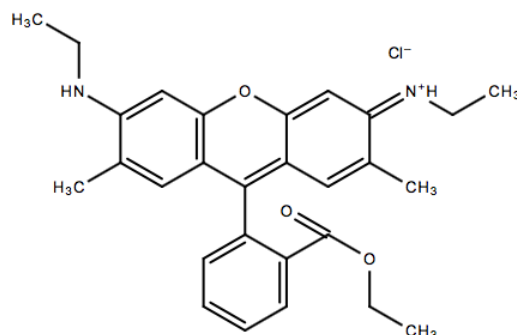


FIGURE 2.16: Molecular structure of Rhodamine 6G.

After droplet impact, the inclusion was investigated for 20 min. Every minute, a fluorescence and a standard light transmission picture were taken. The dye is diffusing into the liquid crystal over time. This becomes obvious from about 10 min after impact. However, on shorter time scales the dye diffusion may be neglected for the purposes of this study.

2.4.4 Inclusion Tracking

Movies of the experiments on inclusion mobility have been recorded by camera EOS 550D. One limitation of this camera is the frame rate, which can be set to 60 frames per second at most. However, in the tilted microscope setup, inclusion velocities were designedly kept small by keeping the tilt angles low. In the vertical setup, the trajectory path is long enough to generate enough data points even for higher velocities. In this setting, the camera was set to very short exposure times in order to avoid blurring.

The movies were analyzed by means of a Matlab program written by Thomas John. The program converts the single frames into black and white images depending on a manually chosen threshold value. Then, measurements are returned for all continuous areas, see figure 2.17. By setting a threshold for the tolerated eccentricity, all near to circular objects can be singled out. Subsequently, circles are fitted to the objects found. The coordinates of the center of the circles and the radii are tracked over the given set of images.

The inclusion velocities were calculated using the generated coordinates of the circles. An onset time needs to elapse before the inclusion velocity reaches a plateau. This time is influenced by various parameters. Considering *droplet inclusions*, the time to achieve constant velocity depends primarily on the cessation of evaporation. Additionally, the embedding process needs to be completed which is usually accomplished in fractions of a second. Note that the time until a full meniscus has formed was not awaited. The time until completion of the process takes much longer than the time of measurement. The meniscus itself and its time of formation increases with the thickness

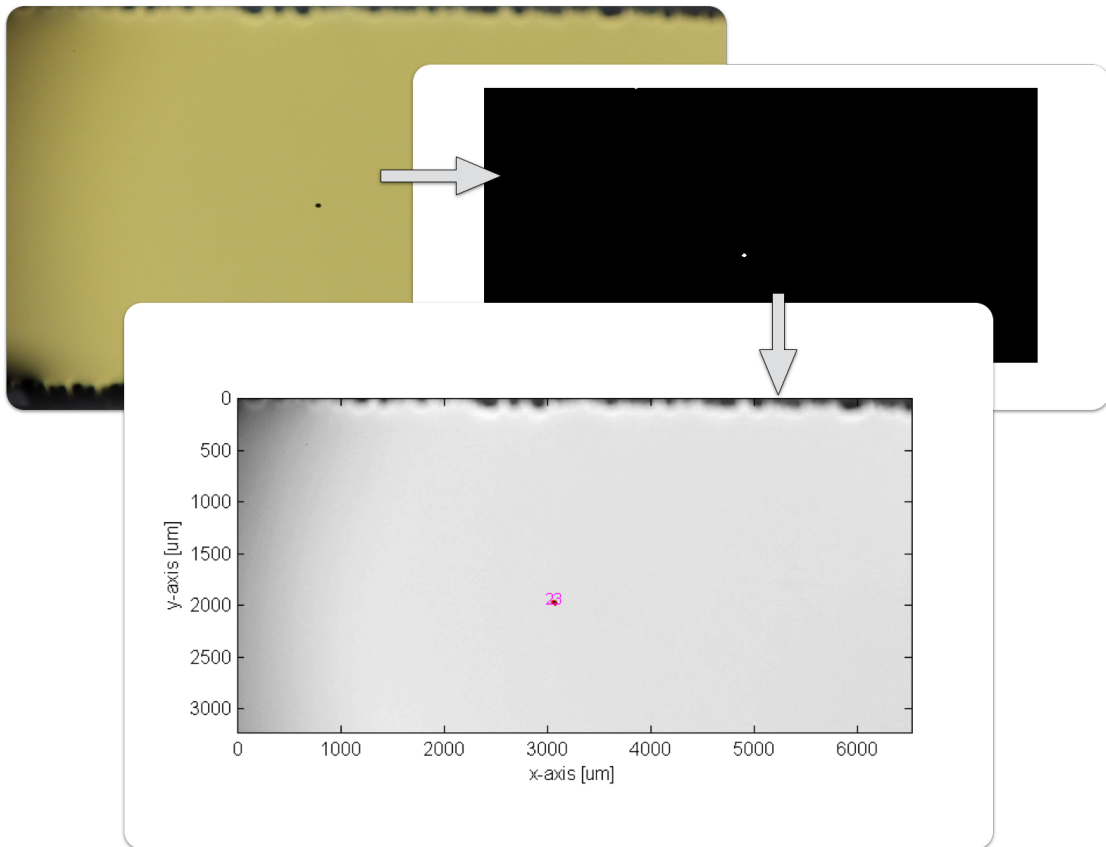


FIGURE 2.17: Droplet tracking. Arrows indicate the work flow of image processing. The initial image is transferred to an inverse black and white image where spherical objects are found. Finally, circles are drawn back into the image which is kept black and white in the background.

of the film and may take up several minutes. Considering *solid inclusions*, a constant velocity is mostly reached in fractions of a second and depends probably mainly on the completion of embedding. A constant velocity may be reached after about 3 s for droplets and 0.5 s for glass beads. After reaching a plateau, the velocity was determined via linear fit to the path-time diagram of the data.

It must be stated that many experiments resulted in data without constant velocity. This was mostly the case for very thin films with high film inclination. Then, the velocity was decreasing steadily in the beginning and, before reaching constancy, starting to decrease even further once a boundary of the film is approached.

Chapter 3

Impact of Picoliter Droplets

This chapter treats the experimental investigations of microscopic droplets impacting on solid silicon wafers and freely suspended smectic films. In the first section, the impact on a silicon wafer and the subsequent evaporation will be shown for different droplet compositions. The major part of this chapter is dedicated to the impact of droplets on freely suspended smectic films. Depending on the impact velocity, the droplet can get trapped in the film, it can rebound or even tunnel through the film. Those phenomena will be discussed in the corresponding sections. In the end, the results will be compared to the estimated driving force and the resistance of droplet impact using Weber and Ohnesorge numbers.

3.1 Impact on Silicon Wafer and Evaporation

The vapor pressure of pure water promotes a quick evaporation of picoliter droplets. Within 5 seconds, a 500 pL volume of water evaporates completely, as shown in the first row of figure 3.1, where a water droplet evaporates on a silicon wafer. If the droplets need to be investigated over a longer time, which will be crucial in some of the following experiments, the vapor pressure needs to be lowered. The addition of salt would cause a lower vapor pressure, but a possible crystallisation near the dispenser nozzle could cause clogging. Hence, different amounts of ethylene glycol were added to water. The evaporation of the droplets slows down significantly with increasing ethylene glycol concentration, as can be seen in figure 3.1. The weight percent of added ethylene glycol is noted to the right of each row. In figure 3.1, every sessile droplet is mirrored at the plane of the silicon wafer. The objects appear lentil-like, though only the upper cap belongs to the real object. The first droplet of each row is formed by up to 10 smaller

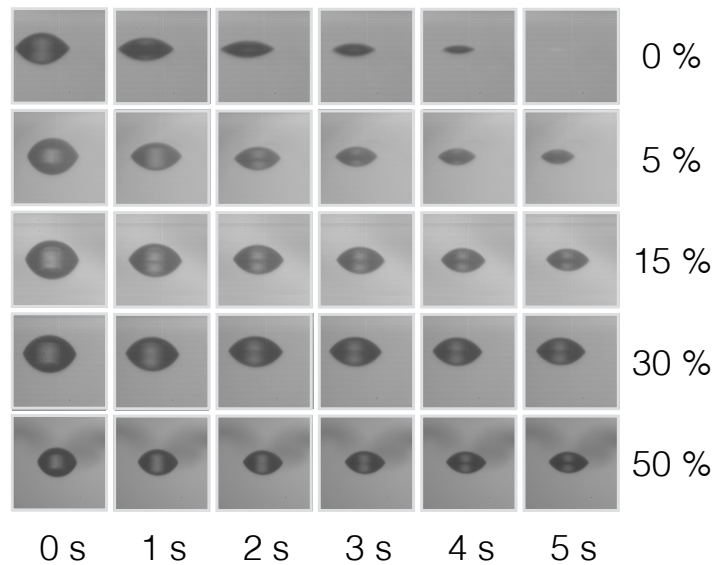


FIGURE 3.1: Side view of a droplet on a silicon wafer over time. The sessile droplets are mirrored on the surface of the silicon wafer. The lower spherical cap corresponds to the reflection of the real object. In every horizontal line of images, a different initial water/ethylene glycol concentration is shown. The initial weight percent of ethylene glycol is shown to the right of each experiment. The droplet at 0 seconds consists of up to 10 smaller droplets shot by the droplet dispenser. The image of the sessile droplet at 0 seconds was taken immediately after merging of the last smaller droplet. The droplets were investigated using the droplet impact setup, see chapter 2.3.3. The width of each image is $279\mu\text{m}$.

droplets shot by the droplet dispenser. The total volume of the merged droplet varies from around $500 - 700\text{ pL}$.

The volume of a droplet is calculated from the images. It is assumed that the cross-section of a lentil-like object is shown which is built from two spherical caps. Since the lower cap belongs to the mirror image, the volume must be divided by two. The reduction of the droplet volume over time is shown in figure 3.2. Every mixture shows evaporation. Even the droplet with an initial concentration of 50% ethylene glycol loses volume. It is likely that the evaporation processes have not ended by the end of the observation. When water molecules evaporate, the surface of the droplet is enriched with ethylene glycol. The higher ethylene glycol concentration at the surface lowers the vapor pressure. This concentration gradient will be equalized by diffusion. Therefore, the evaporation should strongly depend on the diffusion of ethylene glycol in the aqueous droplet slowing down the evaporation process considerably.

Even though a slow evaporation is desirable for the following experiments, tremendous problems occurred in keeping the dispenser running for higher ethylene concentrations. The corresponding higher viscosity perturbs a smooth workflow of the dispenser and resulted in repeated clogging. Due to the sensitivity of the functionality of the dispenser, the lowest amount of ethylene glycol will be employed for most of the following

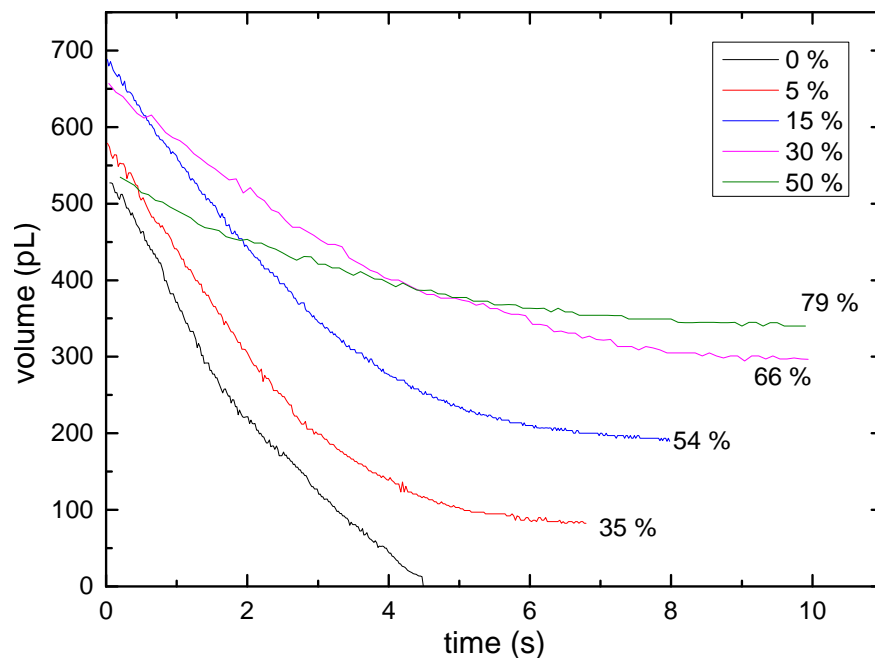


FIGURE 3.2: Evaporation of aqueous droplets with different amounts of ethylene glycol over time. The initial amount of ethylene glycol is noted in the legend in weight percent. The concentration after a given period of time is indicated next to the corresponding curve.

experiments. This provides a viscosity low enough for dispensing and, at the same time, avoids a complete evaporation.

3.2 Impact on Smectic Films: Trapping

If droplets hit a freely suspended film with a low to moderate velocity, they are caught in the film. Experimentally, this was tested for a range of impact velocities. In figure 3.3, two image series of trapped droplets are shown. Note that there is no qualitative change in the impact behavior for the different impact velocities. Both droplets sit on the film and are subsequently integrated.

The trapping process can be roughly divided into three phases with different time scales: in the first phase, the kinetic energy of the droplet is transformed into potential energies of film and droplet deformations, kinetic energy of the film and other forms. Concurrently, a substantial part of the energy is dissipated. This process occurs on a time scale of a few microseconds. Impact deformations and oscillations are not unique to trapped droplets and manifest more distinctive for higher impact velocities. Thus, they will be discussed in section 3.3.1. In the second phase, the droplet changes shape and position in the film to reach a certain balance of capillary forces. This phase progresses on

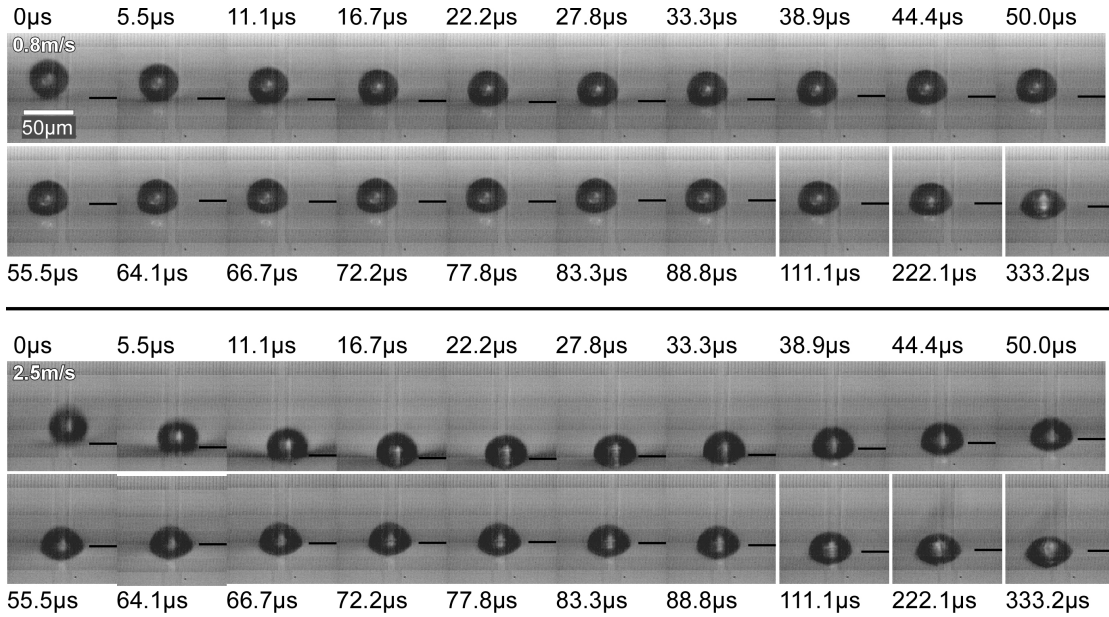


FIGURE 3.3: Photo sequence of droplets impacting on a (SmC) film (*PP* mixture), figure taken from doelle et al. [93]. The first two rows show a droplet with an initial velocity of 0.8 m/s, the lower two rows a droplet with an impact velocity of 2.5 m/s. The black lines indicate the level of the film.

a time scale up to several milliseconds. The third phase is characterized by the formation of a meniscus of smectic material around the droplet. This can take up several seconds. Phase two and three, embedding and meniscus formation, are described in depth in the following.

3.2.1 The Embedding

The process of droplet incorporation into the film starts when droplet and film have a common contact line. In figure 3.3, this is roughly observable from the fourth image. Unlike the droplet and film deformations, the embedding is a process that can only be deduced from the changes in droplet shape. In this work, the embedding time will be defined as the time from initial contact until the droplet reaches a symmetrical shape in the film plane. This may vary for different materials and impact velocities and takes approximately 1 ms.

Shape Detection – The shapes of the droplets were detected automatically and fitted by two arcs of a circle. Thus, the droplet is assumed to consist of two spherical caps. An example of this fit is shown in figure 3.4(c). The two fitted circles intersect at two points, which were connected by a dotted line as a guide for the eye. The position of the invisible film can be deduced from the intersection points. Referring to this line, two contact angles for upper and lower cap are defined in figure 3.4(a). Since the impacting droplet moves downward in this coordinate system, the spherical caps will be named

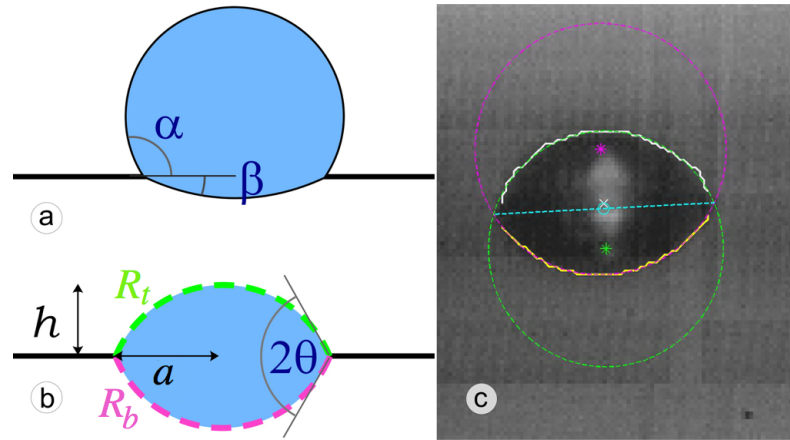


FIGURE 3.4: (a) Sketch of a droplet shortly after impact, illustrating the contact angles α, β . (b) Sketch of an embedded droplet with the equilibrium contact angle θ , the droplet radius a and its height h . The dashed green line indicates the spherical cap shape of the top cap, the dashed magenta line corresponds to the bottom cap. (c) Photo of an embedded droplet, $383 \mu\text{s}$ after impact on a FSF. The two bright curved lines mark the automatically detected droplet profiles. The green and magenta circles are best fits for these profiles. The magenta and the green dot mark the centers of those circles. The circles intersect at two points, which are connected by a dotted, blue line.

The subfigure was adapted from Doelle et al.[93]

top and bottom, or upper and lower cap. In the first images up to 100 ms, the bottom cap could not be fitted due to the fact that the detection is not possible with sufficient precision for small curvatures. In the beginning, only the radius of curvature, R_t , for the upper cap was fitted. With time, the droplet sinks into the plane and both radii of curvature are detectable.

Contact Angles – The evolution of upper and lower contact angles is shown in figure 3.5 for different impact velocities. The lower contact angle β starts at 0° . The upper contact angle α begins around 160° for faster droplets, around 120° for slower droplets. During equilibration, α and β approach each other. From $250 \mu\text{s}$, the upper contact angle drops rapidly and the lower contact angle increases. The time constant of these dynamics is almost independent of the impact velocity. However, the shape change can be more gradual for faster droplets. Interestingly, the bottom contact angle β performs a rather gradual slow relaxation, while the upper contact angle α shows a jump between 250 to $300 \mu\text{s}$.

Thereafter, the contact angles approach each other slowly and the droplet equilibrates in the plane. An contact angle of $\theta = 66^\circ$ is reached for all droplets independent of the impact velocity after about 1 ms . The shape change of the droplet is due to the fact that the surface tensions of the film stretch the droplet in the plane, which will be explained in the following.

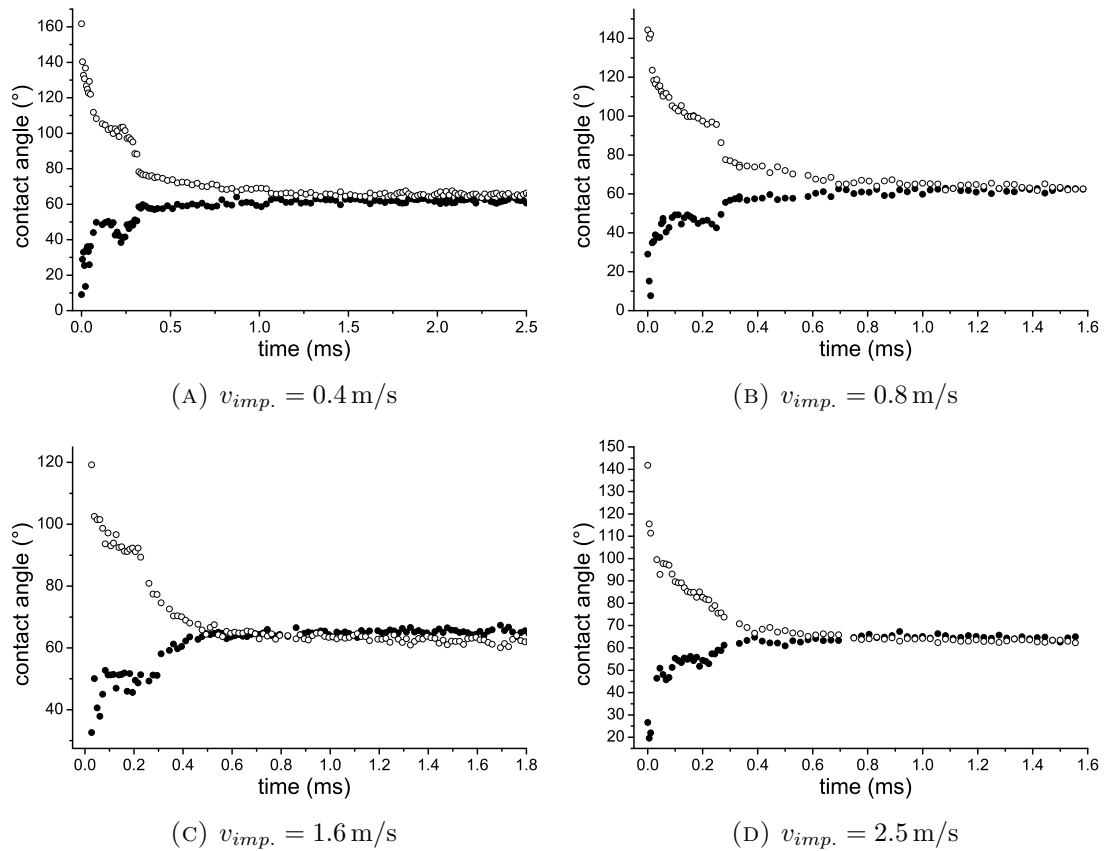


FIGURE 3.5: Evolution of the contact angles α (open circles) and β (full circles) for droplets with different impact velocities. The droplets impinge on a SmA film of $M5N$.

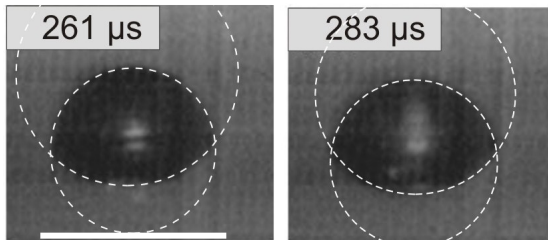


FIGURE 3.6: Shape change of a droplet with 2.5 m/s impact velocity $261 \mu\text{s}$ and $283 \mu\text{s}$ after impact on a $M5N$ film (SmA). The circular arcs are fitted as dashed lines to the upper and lower spherical caps. The white line indicates $50 \mu\text{m}$. Adapted from doelle et al. [93].

Radii of Curvature – Further information can be extracted from the radii of curvature. The radius of the lower surface scatters in the beginning and becomes more stable from 0.5 ms , see open circles in figure 3.7. The radius of the upper surface, full circles in figure 3.7, shows a jump in the data to higher values roughly after $250 \mu\text{s}$, similarly to the contact angle α in figure 3.5. This is also visible in the rapid change of the droplet shape, seen in figure 3.6, where a droplet is shown $261 \mu\text{s}$ and $283 \mu\text{s}$ after impact. Especially the decrease of the lower cap radius becomes obvious in these images. Within about $20 \mu\text{s}$, the level of the film is shifted from the lower part of the droplet almost to its center of mass. After the shape change, the radii approximate each other gradually and equilibrate within 1 to $3 \mu\text{s}$.

Interface Tensions — According to Young’s law, the surface forces acting on the

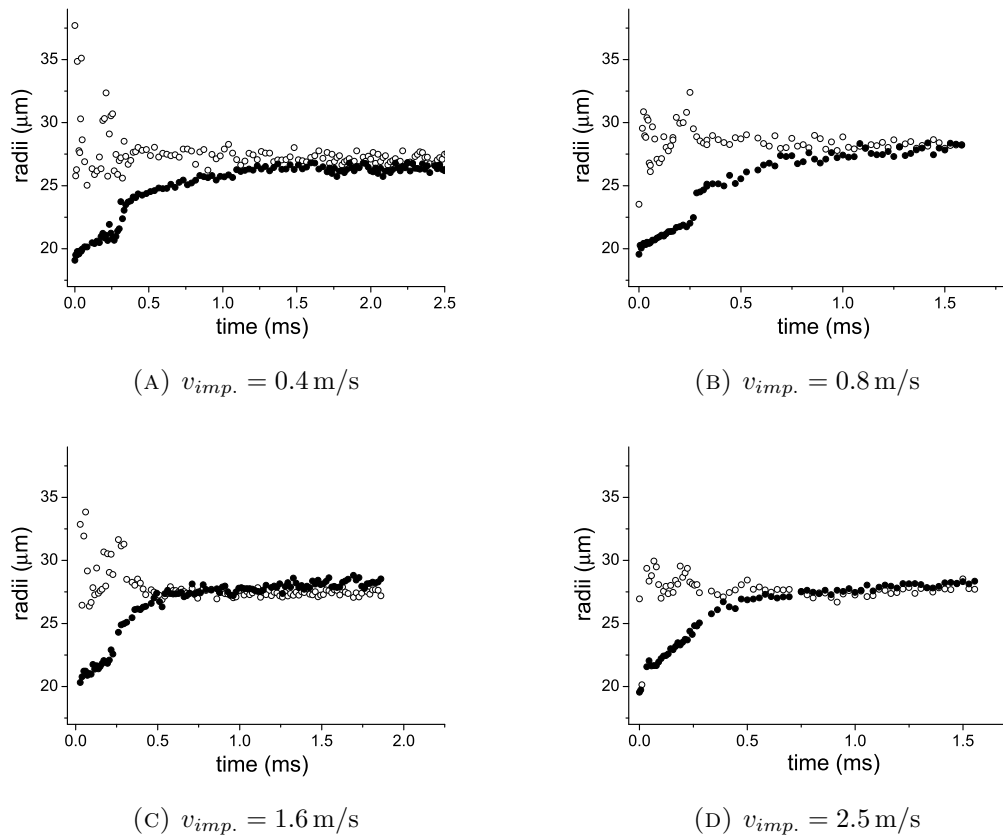


FIGURE 3.7: Evolution of the radii of curvature for droplets with different impact velocities. Open circles correspond to the radii of curvature for the lower cap, see magenta circle in figure 3.4 (A). Full circles refer to the radii of the upper cap, see green circle in figure 3.4 (A). The droplets impinge on a film of $M5N$ (SmA).

droplet can be described with eqn.3.1. A sketch of an embedded droplet with the corresponding surface tensions is shown in figure 3.8.

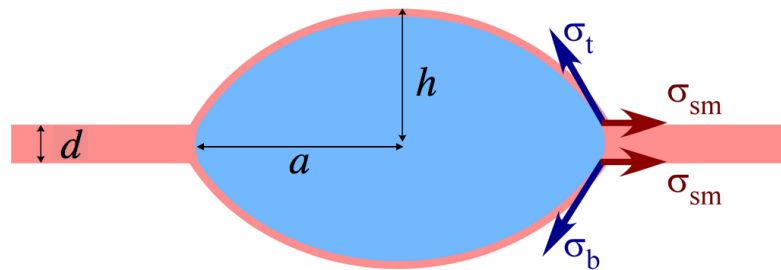


FIGURE 3.8: Cross section of an embedded droplet with related interface tensions. The interface tensions that act on the droplet are shown in red for the smectic film to droplet interface, σ_{sm} . The surface tensions are shown in blue for the top cap to air interface, σ_t , and the bottom cap to air interface, σ_b . The film thickness d and the droplet height h and radius a are indicated by double arrows.

$$\sigma_t \cos \alpha + \sigma_b \cos \beta = 2\sigma_{sm}, \quad (3.1)$$

The interface tensions at top and bottom surfaces of the droplet will be referred to as σ_t and σ_b . For the final droplet shape in equilibrium, when the tensions of its two surfaces are equal, $\sigma_b = \sigma_t = \sigma_d$, $\alpha = \beta = \theta$, and $\sigma_d \cos \theta = \sigma_{sm}$, this equation is equivalent to equation 3.2 [69, 78].

$$\sigma_{sm} = \sigma_d \cdot \frac{a^2 - h^2}{a^2 + h^2}. \quad (3.2)$$

The film thickness d is disregarded in equation 3.2, since it is at least one order of magnitude smaller than the droplet height h .¹

The equilibrium angle of $\theta = 66^\circ$ establishes the balance of droplet and film tensions, equation 3.2. It can be used to calculate the actual interfaces tensions of film and droplet. The surface tension of the *PP* film is presumably about $\sigma_{sm}^{PP} = 22.45 \text{ mN/m}$, see chapter 2. Using these values, the surface tension of the droplet can be calculated to be $\sigma_d = 55 \text{ mN/m}$. However, the surface tension of the bare droplet/air interface should be $\sigma_d = 66.38 \text{ mN/m}$ [92], which reveals that the actual surface tension of the droplet is reduced by 17%. This could be explained by the complete coverage of the droplet by film material. When the droplet hits the film, the film stays intact and covers the bottom of the droplet. Subsequently, the initially bare upper surface is overdrawn by smectic material, which continuously keeps on building. Unfortunately, literature values for comparison are not available. There are only very few studies for interface tensions of liquid crystals and no reliable values exist for our system [96, 97].

Embedding Mechanism – Possible explanations for the droplet embedding mechanism will be discussed in the following. The time scale of the droplet incorporation ranges from hundreds of microseconds up to milliseconds. Since the shape change of the droplets is a faster process, deductive reasoning suggests that the smectic film sets the limiting conditions.

After the first contact of droplet and film, the different contact angles and radii of curvature can be explained by the droplet sitting on the film with a bare upper surface. The film does not wet the droplet immediately. At the line of attack, the smectic film, the droplet and air are in contact. Starting from around $250 \mu\text{s}$, the bare droplet surface is covered by the smectic material. The surface tension of $\sigma = 66.38 \text{ mN/m}$ of the droplet–air interface is higher than the surface tension $\sigma \approx 23 \text{ mN/m}$ of the smectic–air interface. Thus, a covered droplet has a lower surface tension and surface energy is reduced. When the droplet is completely covered, the film stretches the droplet in the plane, deforming it to a lentil-like shape.

¹Since σ_d is higher than the surface tension of the film σ_{sm} , the droplet remains confined and its equilibrium shape consists of two spherical caps. If the surface tension of the droplet were lower than that of the film, the droplet would flatten continuously to cover the whole film area between the supporting frames.

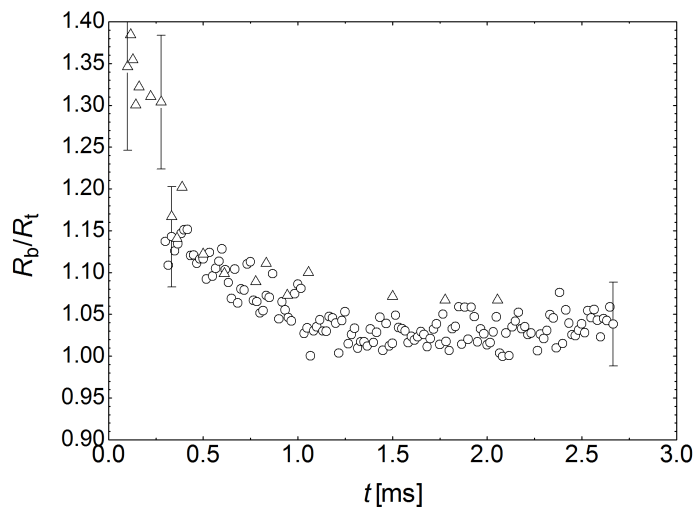


FIGURE 3.9: Ratio of the radii of curvature for the bottom cap R_b and the top cap R_t over time. The droplet had an impact velocity of 0.4 m/s. The target material was a $M5N$ film. Triangles were detected manually, circles automatically. The figure was included from Doelle et al.[93]

The ratio of the two radii is plotted in figure 3.9. Note that ratio of the radii never reaches one. However, this deviation is within our measurement precision.

The equilibrium droplet shape should be symmetrical with the center of mass in the plane of the film. The investigation of the differences of the radii of curvature in the final stage lies beyond the measurement precision, but the data suggests that the symmetrical shape can not be achieved in all experiments within the measured time. In figure 3.9, the ratio of the radii stays above one for more than 2.5 ms. One hypothesis for this phenomenon could be the difference in film thicknesses above and below the droplet. While the film below the droplet is several layers thick, the liquid crystal layer above the film may even be only a monomolecular layer.

3.2.2 Meniscus Formation

With developing the lentil-like droplet shape, the inclusion has still not attained its final form. On a longer time scale, the film material accumulates around the droplet. It continues to cover and reorganize around the inclusion until a pronounced meniscus has formed.

In figure 3.10, the droplet coverage was investigated via reflection microscopy. The uniform magenta color indicates a homogeneous film thickness around the droplet. In the first image of figure 3.10, a bright ring around the droplet is visible. It corresponds to a wedge-shaped meniscus, as seen in figure 3.11. The brightness of the ring derives

presumably from scattered light. The meniscus has already grown to roughly twice the radius of the droplet within 200 ms after impact. In the second image, 2.2 s after impact, roundish areas have formed that are partly light scattering. These areas spread out from the meniscus and continue to creep over the surface of the droplet. Several of these areas in different sizes have grown next to each other. The areas consist of thicker stacks of smectic layers, similar to the phenomenon referred to as smectic islands. Some of which are already reaching out towards the center of the inclusion. In the third image, 3.7 s after impact, the transparent areas have grown distinctively, some have already merged. In the last image, 5.2 s after impact, all spreading islands have merged to encapsulate the droplet. The brightness of the meniscus changes over time, which corresponds probably to an over-all change in the inner structure of the meniscus

In figure 3.11, a droplet with surrounding meniscus is shown from a side view, illuminated by transmission light. The droplet and its meniscus are not distinguishable in this image and the whole object appears dark. However, the meniscus is visually separable from the FSF, which appears as a faint bright line. This distinct separation of meniscus and film is typical for smectic menisci of FSFs [69, 98, 99].

A fluorescence microscopy experiment was conducted to differentiate between the droplet and its meniscus. The fluorescent dye *Rhodamine 6G* was added to the droplet. *Rhodamine 6G* is soluble in both water and the liquid crystal. Fortunately, the time

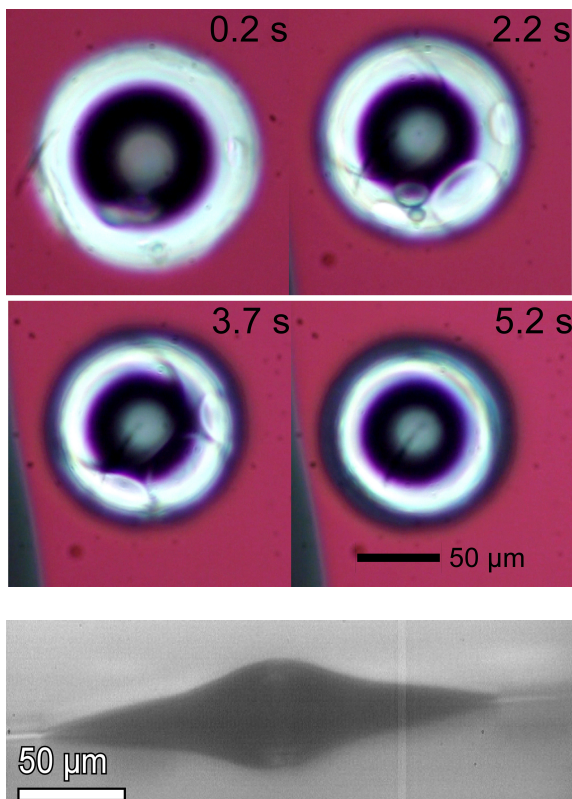


FIGURE 3.10: Reflective microscopy image, showing the top view of an embedded droplet. The droplet consists of an 5 wt.-% ethylene glycol/water mixture. It is enclosed by a meniscus, in a 500 nm thick *M5N* film in the *SmA* phase. The elapsed time after impact is given in each frame. The figure was included from Doelle et al. [93]

FIGURE 3.11: Side view of a droplet 10 min after impact: the level of the smectic film is seen at the sides as faint bright stripes. Figure taken from doelle et al. [93]

needed for the dye to diffuse into the film is sufficiently long. Thus, the droplet is still well distinguishable from the outer medium on time scales up to 5 minutes.

Fig. 3.12 shows a droplet 15 seconds after impact. The bright light microscopy image figure 3.12(a) shows the embedded droplet with its meniscus. Note that the meniscus did not grow into a circular shape. The diagonal stripes correspond to different thicknesses of the FSF. The film is thicker in the bottom right of the image than in the top left. The object sticks to a layer step towards the thinner area of the film. In figure 3.12(b) only the fluorescence image of the droplet is shown. The circular shape of the inclusion is clearly recognizable even though the dye already leaches out slowly into the surrounding medium. The diameter of the inclusion is $42\ \mu\text{m}$. The third image, figure 3.12 c, is an overlay of the previous two images, distinctly showing the size difference of the inclusion and the meniscus with a diameter of about $96\ \mu\text{m}$.

In the following short excursion, the avoidance of pure water as inclusion material is motivated. The long-time behavior of pure water picoliter droplets is strongly determined by evaporation. This encourages the choice of adding a few weight percent of ethylene glycol to a water droplet, especially if the observation time is longer than one second. In figure 3.13, a droplet of pure distilled water that has been shot onto a smectic film. The upper surface of the droplet is not immediately wetted by the film material. There, the evaporation of the droplet proceeds unhindered leaving the droplet to shrink significantly. 5 seconds after impact, the film material has completely covered the remaining water. The size of the inclusion does not change recognizable from 5.1 s to 13 s after impact. It is deduced that the evaporation is almost extinguished by the coverage, at least for the observed time.

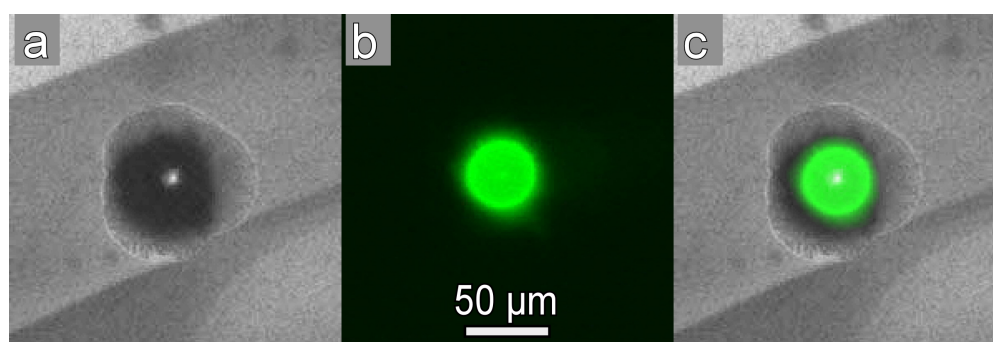


FIGURE 3.12: Top views of a aqueous droplet (5% ethylene glycol) 15 s after impact on a FSF *M5N* film: The images show a microscope image in transmission (a), a fluorescence microscopy image (b), and the superimposed image (c) of both. The microscopy image (a) clearly shows extension of the complete inclusion with its meniscus. The diagonal edges are layer steps of the smectic film. The circumference of the droplet itself can be found from the fluorescence image (b). The figure was taken from Doelle et al. [93].

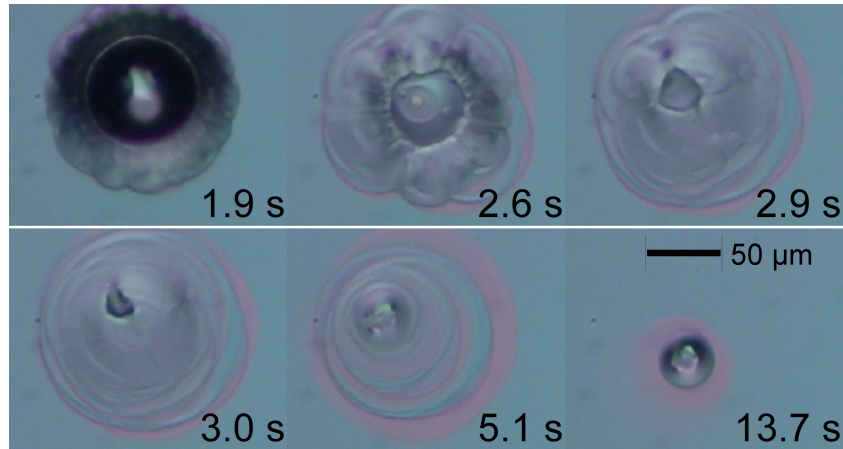


FIGURE 3.13: Evolution and evaporation of a pure water droplet in a FSF (*M5N*, *SmA*) observed via reflective microscopy. The time elapsed since the impact is given at the lower right of each image. After around 3 seconds, the lateral extension of the wedge shaped meniscus reaches its maximum of approximately $100\ \mu\text{m}$. The height of the wedge shaped meniscus was estimated from the interference colors to be several micrometers. The figure was taken from Doelle et al. [93].

3.3 Impact on Smectic Films: Bouncing

In the previous section, droplets with a low impact velocity were trapped by the film. At higher impact speeds, the phenomenon of bouncing may occur. This is only observed in a narrow velocity range and will be discussed in the following.

In figure 3.14, the impact of a droplet is shown from a side view. Two satellite droplets follow the first droplet. Unfortunately, the dispenser starts to produce satellite droplets at higher droplet velocities. All droplets have an impact speed of $4\ \text{m/s}$. The first droplet stretches and strains the film upon impact. The two smaller droplets impact in the deflected stage of the film and merge with the bigger droplet. The whole volume is hurled back up when the film swings back. Finally, the upwards velocity is sufficient to overcome the holding force caused by interfacial tensions and the droplet detaches. The droplet moves away from the film with a velocity of $-2.5\ \text{m/s}$. The velocity will

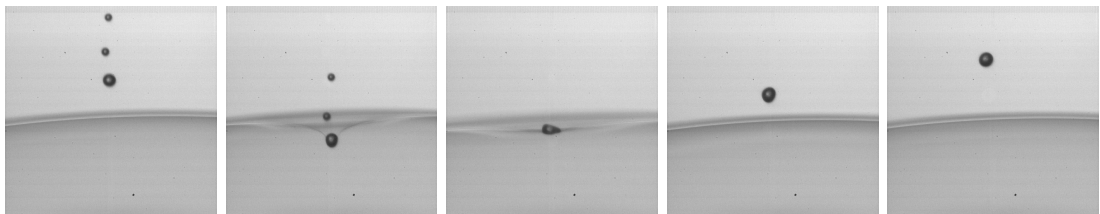


FIGURE 3.14: Droplet impact of a droplet with two satellite droplets onto a *PP* film. The impact was investigated via long range microscopy. The image dimensions are $742\ \mu\text{m} \times 742\ \mu\text{m}$ per image. The images were taken with a frame rate of 21000 frames per second. The time from one frame to the next is $47.6\ \mu\text{s}$. In the third image, the primary droplet merges with the satellite droplets.

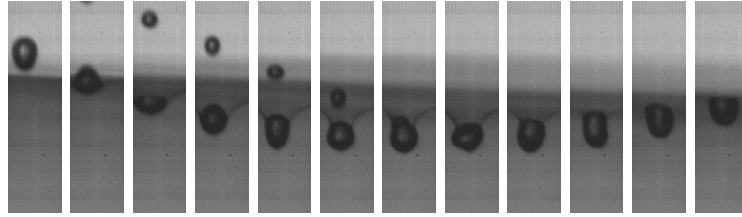


FIGURE 3.15: Droplet impact of a droplet with one satellite droplet onto an *8CB* film. The image dimensions are $93\ \mu\text{m} \times 371\ \mu\text{m}$ per image. The images were taken with a frame rate of 240000 frames per second. The time in between displayed frames is $8.4\ \mu\text{s}$.

be referred to as negative if the droplet reverses the moving direction with respect to the initial impact direction. Noticeably, the backwards motion is much slower than the impacting motion. The largest fraction of the initial kinetic energy is lost.

For *8CB* films, no bouncing droplets could be observed. In figure 3.15, a droplet impacts with enough energy to deflect the film, still the droplet ends up trapped. On the one hand, the satellite droplet impacts when the first droplet already swings upwards. This decelerates the upward movement. On the other hand, the interfacial holding force is higher because of the higher surface tension of *8CB* compared to *PP*. Thus, the interfacial holding force is one critical parameter for the phenomenon of bouncing to occur. Another difference is the liquid crystalline phase. The *8CB* film in the *SmA* phase, with its set thickness of the molecular layers, has a lower ability for elastic behavior.

3.3.1 Droplet and Film Deformations

The droplet and the film deform during the impact and perform damped oscillations back into their original shape. The film oscillation is shown in figure 3.16. The frequency of the droplet oscillations following the impact may be estimated with Lamb's model [79] and equation 3.3,

$$\omega_n = \sqrt{\frac{n(n-1)(n+2)\sigma_d}{\rho a^3}}, \quad (3.3)$$

where ω_n is the angular frequency of the n^{th} mode, ρ_d is the density of the droplet, a its radius and σ_d is the surface tension of the liquid. Since part of the droplet is in contact with the film and part of the droplet in contact with air, a precise description would have to consider two surface tensions or at least an effective surface tension. However, a valuable estimation can be made with the liquid to air surface tension. The radius r_d of the droplet and the mode number n are the two major parameters. The fundamental oscillation mode with $n = 2$, gives the simplified equation

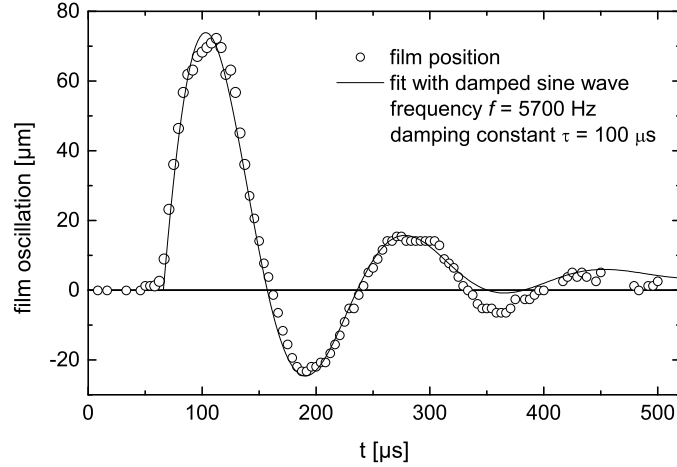


FIGURE 3.16: Damped oscillation of a film after droplet impact and embedding of the droplet. The figure was taken from Doelle et al. [100].

$$\omega_2 = \sqrt{\frac{8\sigma_d}{\rho a^3}}. \quad (3.4)$$

An aqueous droplet with 5% ethylene glycol has a surface tension of $\sigma_d = 66 \frac{\text{mN}}{\text{m}}$ and a density of about $\rho_d = 1018 \frac{\text{kg}}{\text{m}^3}$. With a radius of $22 \mu\text{m}$, $\omega_2/2\pi$ is expected to be 35 kHz. Thus, one oscillation cycle would take around $23 \mu\text{s}$. With a time resolution limit of $5.5 \mu\text{s}$ per frame, such oscillations are detectable although not in detail. Another difficulty of observation are the small amplitudes that decay rapidly.

However, at higher impact velocities, the amplitude \hat{y} of the droplet radius oscillation becomes larger and better observable. For impact velocities of 5 m/s, as seen in figure 3.17, the amplitude \hat{y} is roughly $4 \mu\text{m}$, which is about one-fifth of the radius. The initial kinetic energy of the droplet is partly dissipated by these droplet oscillations. The measured droplet oscillation from prolate to oblate have a frequency of about $\omega_2/2\pi = 35 \text{ kHz}$, which is in good agreement with Lamb's equation, equation 3.3.

The impact of the droplet deflects the film. With increasing impact velocity, the film deformation becomes larger. The energy needed for film deflection can be estimated by the excess surface area that is created during impact. Image figure 3.14 was employed to estimate the excess surface area. A close-up of this image is shown in figure 3.17. A catenoid-like membrane deformation is created with a radius of about 200 to 300 μm . An empirical fit function, see equation 3.5, can approximate the deformation.

$$f_0 - f = z \exp\left(\frac{-x}{x_0}\right) \quad (3.5)$$

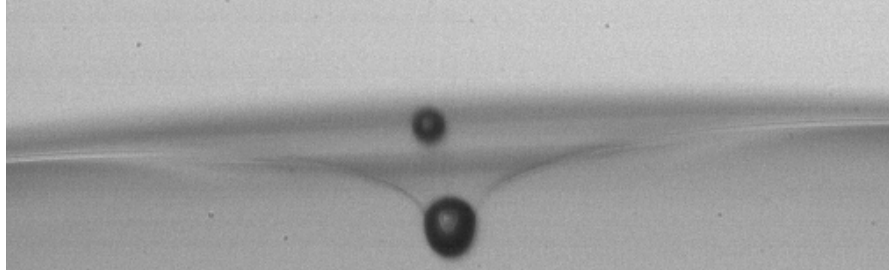


FIGURE 3.17: Deflection of a *PP* film. The center of the impacting droplet has already passed the original position of the film. A smaller droplet follows the first one.

With the parameters of $z = 80 \mu\text{m}$, $x_0 = 55 \mu\text{m}$ and x being the lateral distance from center of impact to the nearest point of no deflection, the surface area increases by $\Delta A = 3300 \mu\text{m}^2$. Hence, the excess surface energy would be $\Delta E = 2\sigma_d \Delta A = 0.15 \text{ nJ}$. This energy is mostly lost by damped oscillations back into the initial position.

3.3.2 Energy Loss and Holding Force

Fig. 3.18, resolves the process of bouncing in more detail. A droplet approaches the film with a velocity of 4.8 m/s and deforms the film upon impact. The satellite droplets follow with the same velocity. The primary droplet reaches its lowest position $43 \mu\text{s}$ after impact. The first satellite droplet with a diameter of $26 \mu\text{m}$ catches the first droplet after the reversal point when the upward motion already started. The second satellite droplet with a diameter of $23 \mu\text{m}$ impacts in figure 3.18 at around $87 \mu\text{s}$. Thus, the upward motion is decelerated by the satellite impacts, also seen in previous experiments. However, the satellite droplets amplify the oscillations of the primary droplet. During

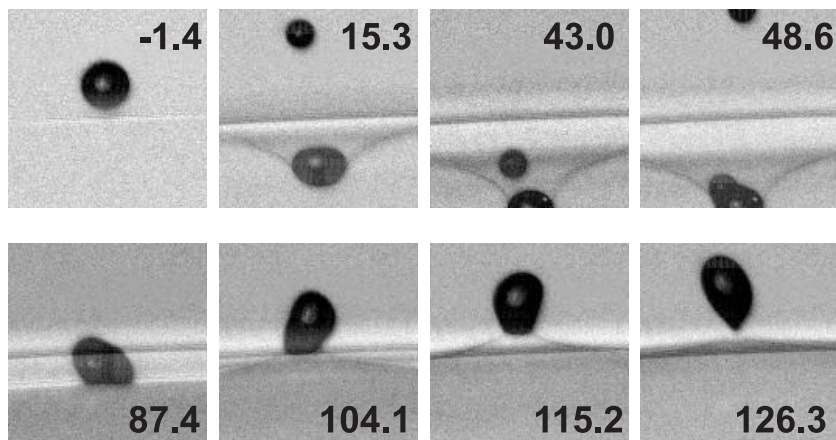


FIGURE 3.18: Droplet and two satellite droplets impacting with a velocity of 4.8 m/s on a *PP* film. The two droplets merge and bounce back from the film. The image are background subtracted with an image size of $186 \mu\text{m} \times 186 \mu\text{m}$. The time in each frame is given microseconds with respect to the first contact of film and droplet. The figure was taken from Doelle et al. [100].

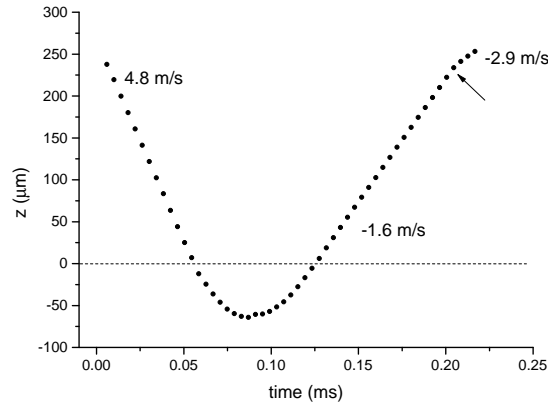


FIGURE 3.19: Trajectory of a bouncing droplet. The position of the droplet in z direction is tracked over time. The dashed line indicates the position of the undeformed film. The arrow points to the time of detachment of the droplet from the film.

the upwards motion, the droplet obtains a prolate shape and, therefore, a short contact line with the film. The droplet detaches after the last image and moves back up with a velocity of -0.96 m/s.

The phenomenon of bouncing can be investigated separately for downward motion, positive direction of impact, and the upward motion, negative direction of rebound. In the first part of the process, the impact energy of the droplet should be high enough to dilate the film but low enough not to pass it. The maximum holding force of the film can be estimated by $2\sigma_{\text{sm}}\pi 2a$, with σ_{sm} being the surface tension of the smectic film and $2a$ being the diameter of a spherical droplet, as shown in doelle et al.[100]. The calculation is valid under the assumption that the film is intact and deforms in a vertical tube with the diameter of the droplet. This can be seen in figure 3.18 at $43 \mu\text{s}$. When the droplet has stretched the film such that the equator of the droplet is in contact with the film, the film should be at its maximum holding force. For a droplet with $42 \mu\text{m}$ in diameter on a *PP* film, this force should be around $5.9 \mu\text{N}$. In fact, an impacting droplet always flattens upon impact increasing the holding force. After collision with the first satellite droplet, an equatorial diameter of $46 \mu\text{m}$ is reached increasing the holding force to about $7 \mu\text{N}$. In the case of *8CB*, the holding force for a $42 \mu\text{m}$ droplet increases to $7.3 \mu\text{N}$ due to the higher surface tension.

In the second part of the process, the upward motion, the surface energy required to detach becomes important. Even if the film swings back and above its original position, the droplet does not necessarily detach. In figure 3.19, the trajectory of a rebounding droplet is shown. Obviously, the droplet slows down when it detaches, indicated by an arrow in the figure. In figure 3.18, the velocity changes from around $v_0 = 2$ m/s to $v_{\text{final}} = -0.96$ m/s upon detachment. If the mass of both satellite droplets are added, the

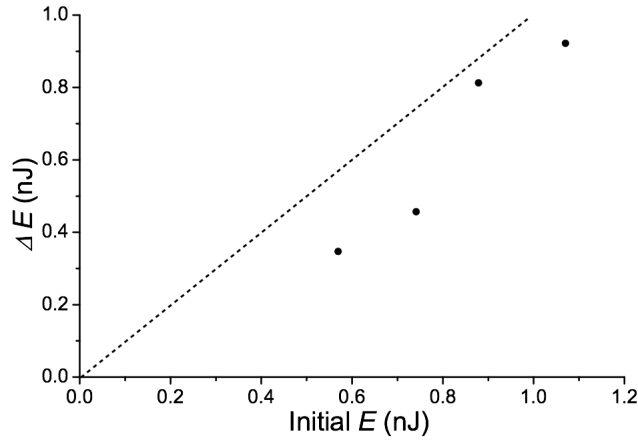


FIGURE 3.20: Energy loss of bouncing droplets on a *PP* film. The initial kinetic energy is plotted over the difference of initial and final energy. The dashed line corresponds to a complete loss of energy.

loss of kinetic energy of $m_d(v_0^2 - v_{\text{final}}^2)/2$ amounts to roughly 84 pJ or 77 %. The energy is mainly needed for work against the capillary forces between droplet and film. The energy loss is shown in figure 3.20. It is evident that the droplets do not lose a fixed amount of energy. Additionally, the satellite droplets can alter the final energy depending on the time and place of impact. Enhanced droplet oscillations may help the detachment. However, a satellite impact during upward motion of the film makes the detachment more difficult.

3.4 Impact on Smectic Films: Tunneling

In this section, the process of droplets penetrating and passing through a FSF will be investigated. The phenomenon will be referred to as tunneling even if some droplets are coated with a smectic layer during the process. The term is chosen because the smectic film regains its shape and stability after the event, leaving the impression as if the film is left unaltered.

Droplets tunneling through an *8CB* film are shown in the first row of figure 3.21. The primary droplet with a diameter of $43 \mu\text{m}$ impacts with a speed of 6.3 m/s. A satellite droplet with the same velocity follows and merges with the bigger droplet. The droplet detaches and leaves the film with 0.8 m/s. The droplet tunneling through the *PP* film, see lower row of figure fig:tunnel, impacts with a velocity of 5.3 m/s. It leaves the film with a velocity of about 1.7 m/s and has a diameter of $42 \mu\text{m}$. The smaller satellite droplets are not passing the film. In the fifth image of the lower row, the film is bend by the primary droplet. The film is invisible from that image on. The primary droplet continues its movement. However, the film is intact only three images later, when the

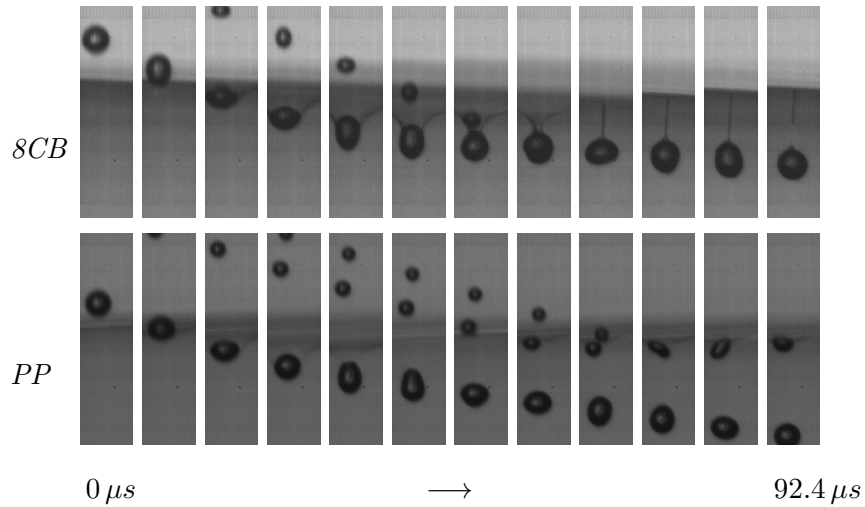


FIGURE 3.21: Droplets tunneling through an 8CB film (upper row) and a *PP* film (lower row). The image dimensions are $93\ \mu\text{m} \times 371\ \mu\text{m}$ per image. The images were taken with a frame rate of 240 kfps. The time in between displayed frames is $8.4\ \mu\text{s}$.

satellite droplets impact. The film healed within at least $25\ \mu\text{s}$. The film thickness should remain the same before and after the event, since the creation of islands and holes occurs on a longer time scale.

3.4.1 Energy Loss

Depending on the velocity of the droplets at the moment of impact on the film, droplets are either trapped, rebound or tunneled as shown in figure 3.22. At low initial velocities, the droplets are trapped. The absolute numbers of the final velocities of the trapped droplets shows a tendency to increase with higher impact velocities. At intermediate initial velocities between 4 and 5.5 m/s rebound becomes more likely. Though, it has to be stated that the plot in figure 3.22 involves droplet radii from 14 to $26\ \mu\text{m}$, thus the data points scatter and the droplet energy may not be deduced. The phenomenon of tunneling occurs at higher initial velocities above 5 m/s. Intuitively, the final velocity also rises by trend with increasing impact velocity.

The energy loss of tunneling droplets is shown in figure 3.21. The experiments were performed for droplet diameters from $30\ \mu\text{m}$ to $50\ \mu\text{m}$. A droplet with a radius of $a = 22\ \mu\text{m}$ and an impact velocity of 5.3 m/s loses about $E_{\text{loss}} = 0.58\ \text{nJ}$ to tunnel through a *PP* film. The same droplet would need more energy to tunnel through an 8CB film due to its higher surface tension. Unfortunately, there is no data available with the same droplet size for 8CB. In the 8CB experiments, the droplet always merged with a satellite droplet upon impact resulting in a bigger volume. In this case, the energies of the individual droplets before merging were summed up to the initial energy.

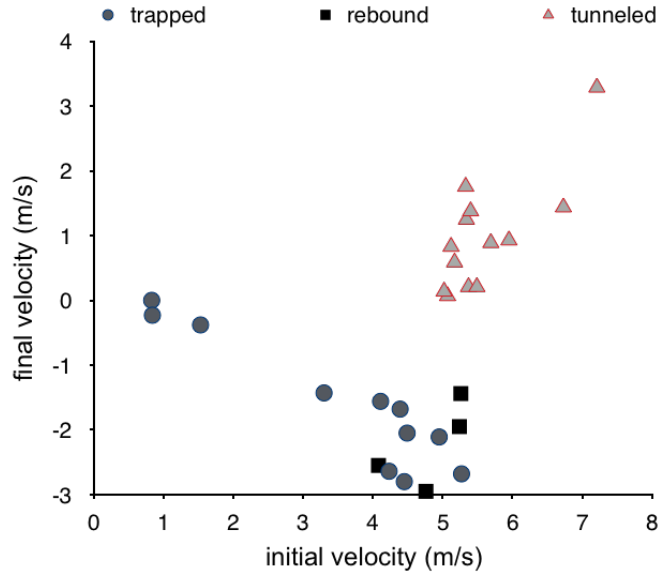


FIGURE 3.22: Final velocity of droplets interacting with a film as a function of the initial impact velocity. Droplets with radii from 14 to 26 μm were investigated on a *PP* film. The initial velocity is the velocity at the moment of impact. The final velocity corresponds to the velocity after impact, when the droplet moves away from the center of the film at maximum speed. When the droplets are trapped or rebound, the direction of motion is reversed resulting in a negative final velocity. The trapped droplets continue to oscillate in the film. Only tunneled droplets show a positive final velocity which increases distinctly with increasing impact velocity.

Droplets with an initial velocity of 6.1 m/s and a merged radius of $a = 27\mu\text{m}$ lose about $E_{\text{loss}} = 1.4\text{ nJ}$ to tunnel through an *8CB* film.

Hereafter, the single components contributing to the energy loss will be discussed.

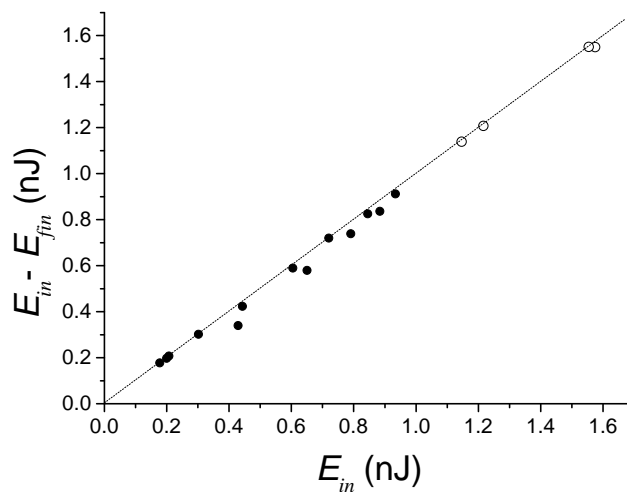


FIGURE 3.23: Energy loss of droplets tunneling through a *PP* film (full circles) and an *8CB* film (open circles). The initial kinetic energy, E_{in} , is plotted over the difference of initial and final energy, $E_{in} - E_{fin}$. The line corresponds to a complete loss of energy.

The initial kinetic energy of the droplet is partly dissipated by droplet oscillations. In chapter 3.3.1, the oscillation frequency of the ground mode was determined to be about $\omega_2/2\pi = 35$ kHz for a droplet with a radius of $22 \mu\text{m}$, $\omega_2/2\pi = 26$ kHz for a droplet with a radius of $27 \mu\text{m}$. The energy needed for this oscillation can be roughly estimated by $E_{\text{osc}} \approx m_d (\omega^2 \hat{y}^2)/6$. The oscillation amplitude \hat{y} increases with increasing impact velocity and is about $4 \mu\text{m}$ for an initial impact velocity of $v_{\text{in}} = 5$ m/s. This yields a small amount of energy of $E_{\text{osc}} \approx 0.1$ pJ for $a = 22 \mu\text{m}$ or $27 \mu\text{m}$. Thus, the droplet oscillations are not primarily responsible for the energy loss. The energy lost through film deformation is estimated in chapter 3.3.1 considering the energy required to increase the surface area. This process needs a minimum energy of $E_{\text{defl}} \approx 0.15$ nJ for a *PP* film and $E_{\text{defl}} \approx 0.18$ nJ for an *8CB* film. Since the excess surface energy was only calculated for the catenoid-like shape in figure 3.17, the energy might as well be higher if the film is deformed further. This is certainly the case for tunneling droplets. Additionally, work is performed against air when the film is moved during deflection. For *8CB* films, the detachment process with filament pinch-off requires energy as well. However, both effects are presumably small and will not be considered here. The energy needed for deflection of a *PP* film of 0.15 nJ (0.18 nJ for *8CB*) is still a small fraction of the overall energy loss of 0.5 nJ (1.4 nJ for *8CB*). This leads to the assumption that the largest part of the initial energy is dissipated immediately.

Obviously, the amount of energy needed for tunneling, as seen in figure 3.23, is not fixed as already presented for bouncing droplets. Considering droplets of the same size, a droplet with a higher impact velocity loses more energy by tunneling than a slow droplet. A possible explanation could be the difference in film deformation. A slower droplet stretches the film less before the detachment. A faster droplet can create a longer hose within the film, because the smectic material needs a specific amount of time to reduce the diameter of the hose before the final pinch-off. Thus, the faster droplet creates more excess film surface and loses more energy. However, the elongation of the hose should have a limit due to the material flow or the thinning of the catenoid. This should set a threshold for the energy loss.

3.4.2 Detachment and Self-Healing

In figure 3.24, the detachment process of a droplet is shown. This is a close-up of the experiment with *8CB* shown in figure 3.21. Clearly, the film does not break when a tunneling event occurs. In the experiments with *8CB* films, the droplet impact creates a tubular extension of the film. The length of this hose depends partly on the impact velocity. A higher impact velocity forms a longer hose. The diameter of the hose contracts over time. Finally, the hose thinning leads to filament formation and encapsulation of

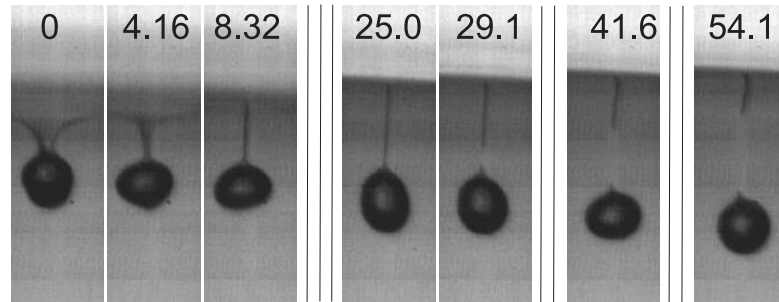


FIGURE 3.24: This close-up shows the detachment process after tunneling through an *8CB* film. The time in microseconds is given at the top of each image, starting from the first image. The image width is $82\ \mu\text{m}$. The figure was taken from Doelle et al. [100]

the droplet. As soon as the filament forms, the deflection of the film falls off and it heals up.

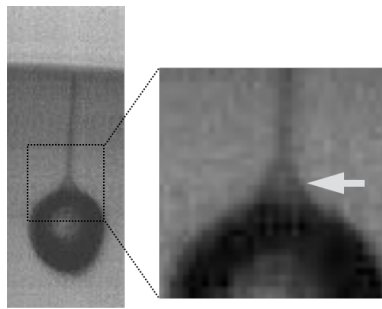


FIGURE 3.25: Air and droplet encapsulated by a smectic *8CB* film. The droplet is hanging from the smectic film similar to a ball in a string bag. When the filament is formed, the bag closes and a cone-shaped volume with air becomes trapped alongside the droplet. The trapped air does not absorb as much light as the droplet and appears brighter. It is indicated by an arrow in the enlarged and visually enhanced image.

In all *8CB* experiments, a small amount of air gets trapped along with the droplet during filament formation, as seen in the close-up in figure 3.25. When the droplet continues its motion, the filament pinches off close to the droplet. Both ends of the filament contract slowly over time. A filament with a length of about $70\ \mu\text{m}$ needs at around $350\ \mu\text{s}$ to retract completely.

The self-healing properties were also found for *PP* films. Even though the process of filament formation is not observed, the trapping of satellite droplets by an intact film, shortly after the tunneling event, confirms a rapid the self-healing, see figure 3.21.

3.4.3 Coated Droplets

During the tunneling event, the droplets become wrapped with smectic film. It is assumed that the film thickness of the freely suspended film is not altered through tunneling, as already explained in the introduction of section 3.4. Following this assumption,

the smectic coat of the droplets should have the same thin film thickness as the freely suspended film. However, the detached coated droplet can still change its size subsequently. If the coated droplets were kept in an air atmosphere, evaporation and shrinkage was observed. If the coated droplets were kept in water, the shape changes were not as drastic. Still, water and ethylene glycol molecules are probably both able to establish a transmembrane flow if the smectic coat is sufficiently thin. Yet, the specifications of this smectic liquid crystal as a permeable membrane are hardly explored [101].

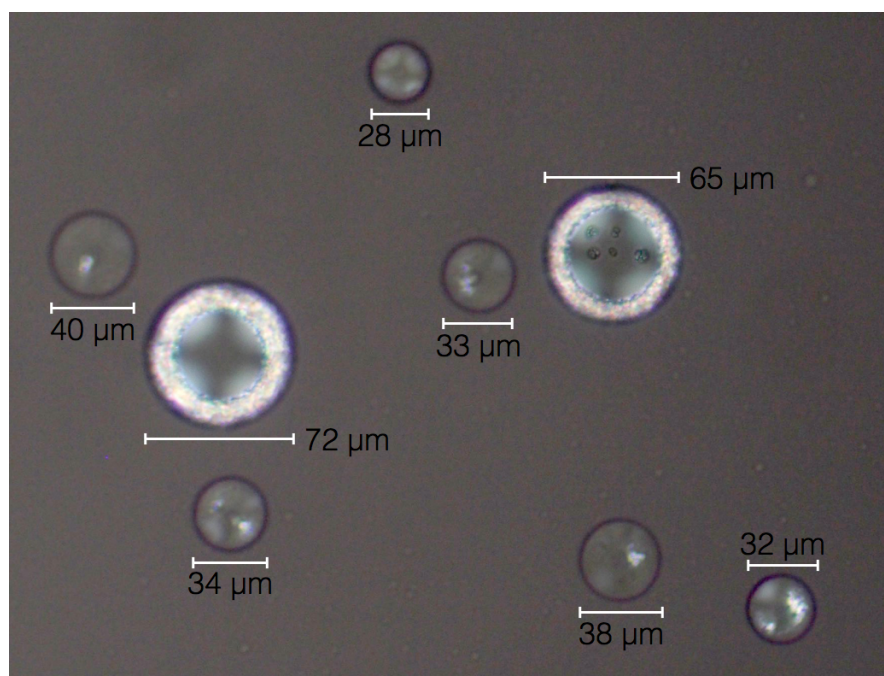


FIGURE 3.26: Shells collected on a large sessile water droplet on a glass slide observed with crossed polarizers. The smectic shells consist of *8CB*. The aqueous liquid inside and outside the shells contains 5% ethylene glycol. Contrast and brightness were adjusted for better visibility.

A tunnelled droplet can survive an impact onto solid or liquid surfaces. The small droplet dimensions lead to a small gravitational force and a sufficiently small fall velocity. A crossed polarizer image of several coated droplets is shown in figure 3.26. They were collected by a large sessile drop of water resting on a glass substrate. Two inclusions are distinctly bigger and brighter than the rest. Both show a bright and colorful ring around the encapsulated core which derives from a strong birefringence. The strong intensity must originate from an accumulation of liquid crystal molecules in different orientations which indicates the formation of a meniscus. Inside these two inclusions, diffuse dark crosses are visible. Considering a homeotropic alignment, the film should be curved spherically to generate an extinction cross, see explanation in section 1.1.2. Although a curved surface was detected, the two inclusions are not spherical but rather shaped like a spherical cap. This conclusion seems likely because of the extraordinary large droplet diameter and the surrounding meniscus. The employed droplet dispenser

is not able to create droplets with a diameter larger than $45\ \mu\text{m}$. It is deduced, that the encapsulations have attached to either the water surface or the glass substrate, as can be seen in figure 3.27(b) and (c).

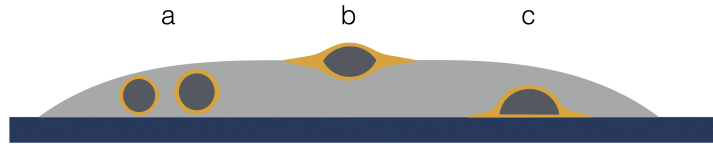


FIGURE 3.27: Side view sketch of possible configurations of the shells in figure 3.26. The large sessile droplet of water is shown in light gray. The droplet rests on a glass slide. The yellow areas depict the smectic liquid crystal and the darker gray inclusions represent the droplet material. (a) The shells are intact and completely immersed. (b) The deformed shell is floating on the water surface similarly to figure 3.11. (c) The shell is attached to the glass slide forming an encapsulation in the shape of a spherical cap.

The other, darker inclusions are intact coated droplets that are probably submerged, compare figure 3.27(a). The blurred extinction crosses, that are prominent in the two big inclusions, are missing for most of the smaller inclusions. Only the two smallest inclusions show faint extinction crosses. Some of the inclusions show small, arbitrary bright areas. Probably, these originate from a higher concentration of LC material with a stronger birefringence. Hence, the film thicknesses of those inclusions are not homogeneous. A possible cause for the accumulation of material in these areas is a preceding shrinkage. Since a shrinkage of the core leads to a surplus of coating material, the creation of thicker areas or an over all thicker smectic coat is inevitable. The strong birefringence and the different colors of the patches lead to the assumption that these accumulations of liquid crystalline material are not ordered in smectic layers. Not smectic islands have formed but disordered aggregations.

Previous experiments were performed showing the possibility of tunneling droplets through freely suspended liquid films. However, this is the first work presenting wrapped droplets as a result of this process. The coated droplets may also be referred to as liquid crystalline shells. Recently, researchers succeeded in producing smectic shells to investigate their textures and interesting defect structures [102–107]. Those shells were generated with microfluidic setups which are limited in downsizing. Shells with diameters smaller than $100\ \mu\text{m}$ can only be achieved through subsequent osmosis increasing the shell thickness. The tunneling method is the first approach to small shells with film thicknesses of less than a micrometer.

3.5 We-Oh Classification

Picoliter droplets with diameters of about $40\ \mu\text{m}$ and impact velocities from $0.4\ \text{m/s}$ to $5\ \text{m/s}$ give Weber numbers between 0.09 and 13 , following $We = \ell \rho v^2 / \sigma$. The Ohnesorge number Oh is approximately 0.037 , following $Oh = \eta / \sqrt{\rho \sigma \ell}$. The range of the experimental data is shown as a function of We and Oh numbers in figure 3.28.

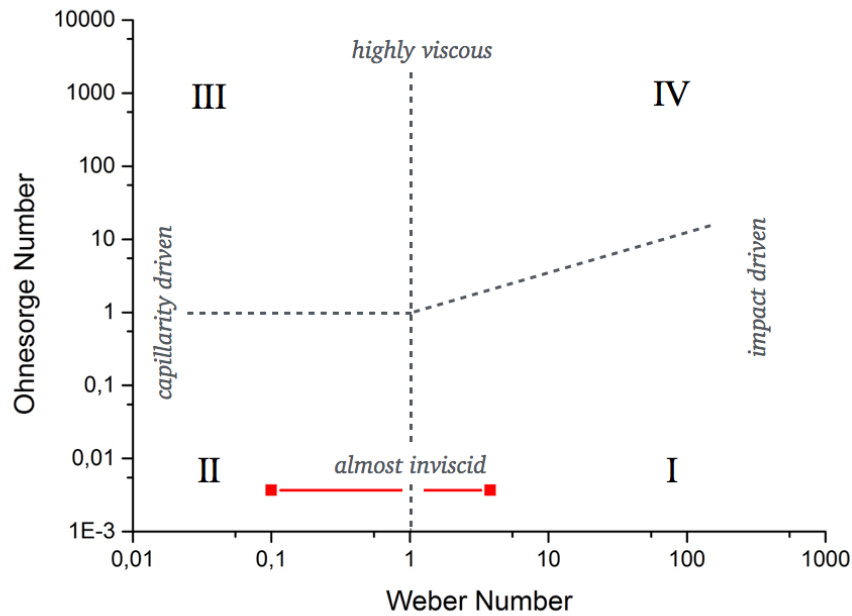


FIGURE 3.28: Range of experimental data as a function of We and Oh numbers. The four regimes I-IV of Weber and Ohnesorge classification are indicated as a guide for the eye with the dominating driving forces and resistances shown in the corresponding area of the diagram.

Thus, viscosity effects are rather small in comparison to surface tension effects. All impact experiments can be classified in regimes (I) and (II) introduced in chapter 1.2.1. The droplet fluid can be treated as inviscid and surface tension effects are dominant. This agrees well with the experimental data. As shown in the previous sections and figure 3.3 or figure 3.18, independent of the impact velocity, droplet do not show any splashing and oscillations are damped out in fractions of a millisecond.

3.6 Conclusions

The impact of micrometer-sized droplets was investigated with a long range microscope and a high speed camera. imaging of a water/ethylene glycol mixture on freely suspended smectic films using a micro droplet dispenser that can be precisely positioned near the film. The Ohnesorge number in the experiments is well below 0.01 and the Weber

number varies from 0.1 to 3.8. For the droplet diameters of this study, the surface tension dominates the impact behavior. The droplet impact may be described by a simple deposition without splashing, followed by a steady immersion in the film and meniscus formation. In addition to dissipation through viscosity of a droplet, the freely suspended film absorbs impact energy. Thus, compared to the work of Son et al. [108], who have studied similar droplet sizes on solid substrates, our droplets show even less deformations.

Initially, the droplet rests on the intact smectic film, even if it hits the film at velocities of 2.5 m/s. The same geometry has been proposed for the equilibrium description of colloidal silica particles on freely suspended films by Conradi et al. [109]. In contrast to that experiment, where the authors assumed that the upper surface of the beads remained bare during the experiment, our droplets are wetted completely within approximately 1 ms after impact.

After immersion, the droplets develop a lentil-like shape with its two spherical caps sticking out of the film plane. Comparing droplets with different impact velocities, we found that a higher impact velocity slightly accelerates the immersion process, without changing it qualitatively. The experimental setup enables a measurement of the contact angle θ of the immersed droplet, with the possibility to compare interface tensions of the droplet and the film. When we assume a surface tension of the film of $\sigma_{\text{sm}} = 22.3$ mN/m, which is a typical value for smectic materials, we obtain a tension of 55 mN/m for the droplet/smectic film/air interface.

A meniscus is formed around the droplet within a few seconds after impact. Inside the meniscus, the droplet returns to spherical shape. Menisci shapes around glycerol droplets in smectic C films have been studied in detail earlier. [98] The menisci observed here are geometrically very similar, but the smectic A films do not develop corona patterns.

When multiple droplets are shot onto the same position in the film within few hundred milliseconds, they coalesce and form larger drops. By this method, one can control the sizes of drops in discrete steps and prepare inclusions with more than 100 micrometers diameter. Furthermore, impact parameters can be varied such that droplets tunnel the free standing films, whereby they are encapsulated in a thin smectic layer, or reflected by the film. These scenarios will be described elsewhere.

Pure water droplets are not suitable for the creation of inclusions in freely suspended films because they evaporate quickly, leaving only irregular and not well reproducible remnants in the film.

Chapter 4

Motion of Inclusions in Freely Suspended Films

Experiments on the motion of liquid and solid inclusions in freely suspended films (FSFs) will be presented and discussed in this chapter. When droplets or beads are embedded in a film, they are free to move within the film plane. Thus, rheology experiments can be performed using these inclusions. In this study, their diameter is at least one order of magnitude larger than the film thickness. This restricts a free motion to the x-y-plane of the film which will be explained in the first section along with the experimental model.

The behavior of bead and droplet motion on SmA films was investigated earlier by Sebastian Baumgärtner [110]. One initial question of this study was to determine why the space time plot of droplets differs from the behavior of solid inclusions. For droplets, a constant velocity could be detected only after seconds. Starting with an initial higher velocity, the droplets would always slow down with time. Additionally, the final velocities were deemed too small for the ejected droplet volumes. Two hypothesis were set up as possible explanations. Firstly, the case was made that the droplets need up to seconds to fully embed in the film and are therefore slowed down in the process. And secondly, the friction within the droplet was considered a possibility to cause the allegedly small final velocity which does not seem reasonable. Eventually, no dependence of the droplet velocity on the film thickness could be found leaving many questions to be answered.

After an introductory part, liquid inclusions in SmA films will be described in the second section of this chapter including the determined viscosities, mobilities and the general challenges of experiments with fluid inclusions. The section for SmA films is concluded by a short excursion into the motion of droplets moving in close vicinity to each other.

In the third section, the motion of solid particles in SmC films will be treated. The orientation of the SmC director around the bead is analyzed for a stationary setting. Subsequently, the change of director orientation for a moving bead is shown as well as the flow field around it. Furthermore, the response of the velocity is investigated for a bead moving through π -walls and more complex orientations in the film. Lastly, the velocity and mobility of beads in a film with homogeneous director field will be compiled for SmC films.

4.1 Experimental Model

If a body slides down an inclined plane, forces like gravity and frictional forces act on it. A balance between the forces arises when the slope is sufficiently long and the movement is not stopped. In this thesis, the inclined plane is a freely suspended liquid film and the sliding object is embedded into this film. Since the object is fixed in the film plane, the inclination can be as high as 90° . The inclusion diameter is orders of magnitudes larger than the film thickness and the object sticks out of the film plane on both sides, cf. figure 4.1 .

Directly after inclusion placement, the gravitational force (F_{gx}) in the film plane is counteracted only by buoyancy (F_b) and the object starts to move. This motion is counteracted by frictional forces (F_{fr}) of the thin film and the surrounding air. With increasing inclusion velocity these forces grow until a force balance is reached as shown in equation 4.1. This results in a constant velocity. The friction within a thin film is the parameter of interest. It can be determined if all other components in equation 4.1 are known.

$$\vec{F}_{gx} + \vec{F}_b + \vec{F}_{fr} = 0 \quad (4.1)$$

Subsequently, the the viscosity of the film can be analyzed as well as other parameters like mobilities of inclusions in the film.

4.1.1 The Buoyancy

The buoyancy is calculated assuming a cylindrical shape in the film is occupied by the embedded inclusion, following equation 4.2. Considering a density of the liquid crystal of 1025 kg m^{-3} (8CB) [111] and a film thickness of 200 nm the buoyancy should be around $F_b \approx 0.03 \cdot 10^{-10} \text{ N}$.

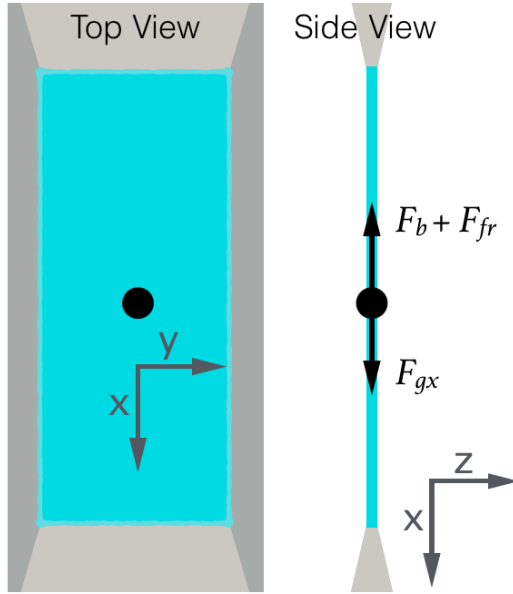


FIGURE 4.1: Sketched top view and side view of an inclusion in a vertical film defining the coordinates x , y and z . The forces acting on the inclusion are depicted in the cross section of the film. The gravitational force (F_{gx}) in x direction is counteracted by frictional forces (F_{fr}) and buoyancy (F_b). The film is drawn disproportionately thick and the film length was shortened for better visibility.

$$\vec{F}_b = m_b g \sin(\delta) = \pi r_m^2 d \rho_{\text{film}} g \sin(\delta) \quad (4.2)$$

m_b - buoyancy mass, g - gravitational force, δ - angle of film inclination, ρ_{film} - density of film material, r_m - radius of inclusion and meniscus, d - film thickness

4.1.2 The Gravitational Force

The gravitational force depends on the volume and density of the moving object, cf. equation 4.3. It will be discussed separately for solid and liquid inclusions.

$$\vec{F}_{gx} = V_{\text{incl}} \rho g \sin(\delta) \quad (4.3)$$

(V_{incl} - volume of inclusion, ρ - density of inclusion, g - gravitational constant, δ - angle of film inclination, $\delta = 90^\circ$ for vertical films.)

Liquid inclusions — Even if the density of the liquid is known, the gravitational force acting on a liquid inclusion is not easily accessible. The three main challenges that have to be considered are evaporation, shape change and meniscus formation. Firstly, a big drawback for experiments with liquid inclusions is evaporation. Although the addition of Ethylene Glycol hinders evaporation to some degree, the droplets lose mass after deposition. Due to this problem, the droplets are given time to evaporate for at least two seconds after impact. No velocity was extracted from data before this time. It is assumed that the subsequent observation time is short enough to ensure a stable

droplet volume. Secondly, the shape of a liquid droplet changes from spherical to lentil-like when the droplet enters the film. The opening angle of lentil-like embedded droplets was found to be $\theta = 66^\circ$, cf. chapter 3. It is assumed that the opening angle of the lentil does not change significantly for radii from 15 - 50 μm in the investigated time frame.

The gravitational force acting on a lentil-like inclusion is stated in equation 4.4. The lenticular volume is calculated from two spherical caps. The height of a cap is determined by equation 4.5.

$$\vec{F}_{gx} = V_d \rho_d g \sin(\delta) = \frac{\pi}{3} h_d (3a_d^2 + h_d^2) \rho_d g \sin(\delta) \quad (4.4)$$

$$h_d = a_d \left(\frac{1 - \cos(\theta)}{\sin(\theta)} \right) \quad (4.5)$$

(V_d - volume of droplet, ρ_d - density of droplet, h_d - height of one spherical cap, a_d - base radius of spherical cap of the droplet, θ - opening angle of spherical cap, cf. chapter 3.)

Thirdly, the meniscus becomes relevant because it builds up and sticks out of the film plane like the droplet. The height and extension of the overall object containing droplet and meniscus needs to be measured in order to determine the effective mass. In figure 4.2, the side view of an inclusion is shown 10 minutes after impact. A ratio of meniscus to droplet height of $h_m/h_d = 14 \mu\text{m}/23.2 \mu\text{m} = 0.6$ is derived from this image as well as the ratio of the inner meniscus radius a_m to droplet radius a_d of $a_m/a_d = 28.3 \mu\text{m}/42.1 \mu\text{m} = 0.67$. Since the radius of the meniscus is not as extended for time periods up to only 10 seconds, the ratio of outer to inner meniscus radius is derived from figure 4.4. If the appropriate incident light is coupled in from above, the meniscus can be seen in reflective microscopy with sufficient resolution. The inclusion diameter with meniscus can be determined to be 49 μm and the inner radius has a diameter of 26 μm . The detectable inner radius corresponds to the inner radius of the meniscus a_m as described in figure 4.3 rather than the actual droplet radius, giving a ratio of $a_m/r_m = 0.53$. Intergrating this into the ratio of a_m/a_d , the droplet radius a_d is given by $a_d = 0.79 r_m$. Note, that the sketch used for calculating the shape of the inclusion differs from the shape that is most probable. However, the densities of the droplet and the meniscus are very similar and no big error will be made by counting parts of the whole inclusion to the droplet instead of the meniscus.

The meniscus is not visible in low resolution used in the following velocity experiments and appears rather black. The droplet tracking technique detects only the radius of the complete inclusion including the meniscus. This becomes evident when looking at figure 4.5. Thus, the mass of the complete object is calculated as follows.

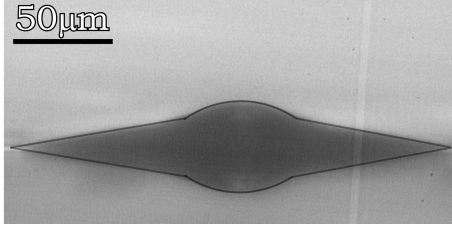


FIGURE 4.2: Side view of a large droplet 10 min after impact with lines indicating the extensions of meniscus and droplet. Modified from figure 3.11.

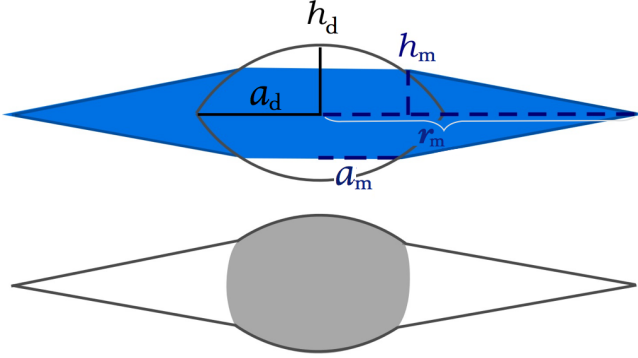


FIGURE 4.3: The upper sketch defines the following variables: h_m - height of meniscus, r_m - outer radius of meniscus, a_m - inner radius of meniscus, a_d - radius of droplet, h_d - height of droplet. The lower image shows a sketch of a probable droplet shape within the meniscus. These sketches were deduced from figure 4.2.



FIGURE 4.4: Reflective microscopy image of an embedded droplet in a FSF of *M5N*. The picture was taken about 12s after impact with a magnification of $3.3 \mu\text{m}/\text{Pix}$. It reveals the meniscus around the droplet.

$$m_{d\ m} = (V_d \rho_d) + (V_m \rho_{\text{film}}) \quad (4.6)$$

The mass of droplet and meniscus $m_{d\ m}$ is given by their volumes V_d and V_m times their corresponding densities ρ_d and ρ_{film} . The droplet volume V_d is stated in equation 4.7. Since the droplet radius is overestimated by the tracking method, the measured radius r_m is reduced by the aforementioned ratio of $a/r_m = 0.79$. The height of the spherical cap h_d is given in equation 4.5, bearing in mind that $a_d = 0.79 r_m$.

$$V_d = \frac{\pi h_d}{3} (h_d^2 + 3(0.79 \cdot r_m)^2) \quad (4.7)$$

The volume of the meniscus V_m is assumed to consist of two truncated cones minus the overlapping part of the droplet.

$$\begin{aligned} V_m = & \left\{ 2 \cdot \frac{\pi h_m}{3} [r_m^2 + (r_m \cdot 0.53) + (r_m \cdot 0.53)^2] \right\} \\ & - \{V_d\} \\ & + \left\{ \frac{\pi h_d \cdot 0.4}{3} [3(r_m \cdot 0.53)^2 + (h_d \cdot 0.4)^2] \right\} \end{aligned} \quad (4.8)$$

The gravitational force $F_g = g m_{\text{d m}}$ for a film inclination of 90° is estimated to be $F_g \approx 1.6 \cdot 10^{-10} N$ considering a measured radius of $22 \mu\text{m}$, a density of $\rho_{\text{d}} = 1018 \text{ kg m}^{-3}$ and $\rho_{\text{film}} = 1025 \text{ kg m}^{-3}$.

Solid inclusions — The gravitational force acting on solid inclusion is easy to determine if the solid object is spherical. The radius and the film inclination can be measured optically. A rough estimate yields a gravitational force of $F_g \approx 10 \cdot 10^{-10} N$ considering an inclusion radius of $22 \mu\text{m}$, a density of glass of 2490 kg m^{-3} and a film inclination of 90° .

$$\vec{F}_{gx} = V_{\text{sph}} \rho_{\text{inc}} g \sin(\delta) = \frac{4}{3} \pi r^3 \rho_{\text{inc}} g \sin(\delta) \quad (4.9)$$

(V_{sph} - volume of spherical inclusion, ρ_{inc} - density of inclusion, g - gravitational constant, r - radius of spherical inclusion, δ - angle of film inclination)

Similarly to liquid inclusions, a meniscus of film material forms around the bead very quickly and adds mass to the inclusion. However, the addition of mass is disregarded for several reasons. Firstly, the bead radii, which were mostly around $50 \mu\text{m}$, are larger than the droplet radii. Secondly, the mass per radius is higher for spherical objects, giving a lower meniscus mass to bead mass ratio. Additionally, the menisci seem less extended in the bead experiments. And most importantly, the density of glass is around 2.5 times larger than the liquid crystal density. Thus, the meniscus mass should be small compared to the bead mass.

4.1.3 The Frictional Force

The friction can not be approximated by the Stokes' law as introduced in section 1.4.1. Air and film friction are not independent from each another and it is physically not correct to add them up. When looked at separately, the flow field of the film around the inclusion should be much more extended than the flow field in air, see Saffman-Delbrück model in chapter 1.4.2. Yet, the no slip condition between air and film cannot be violated when combining the flows. Thus, the real flow field of air should expand wider compared to the a simple Stokes' flow in air. When all required forces in the force balance have been examined, an estimate of the frictional force in the film is accessible, cf. equation 4.1.

Considering a measured radius of $r_{\text{m}} = 22 \mu\text{m}$, the frictional force is found to be on the order of $F_{\text{fr}} \approx 9.9 \cdot 10^{-10} N$ for spherical glass beads and $F_{\text{fr}} \approx 1.6 \cdot 10^{-10} N$ for lentil-like droplets with meniscus.

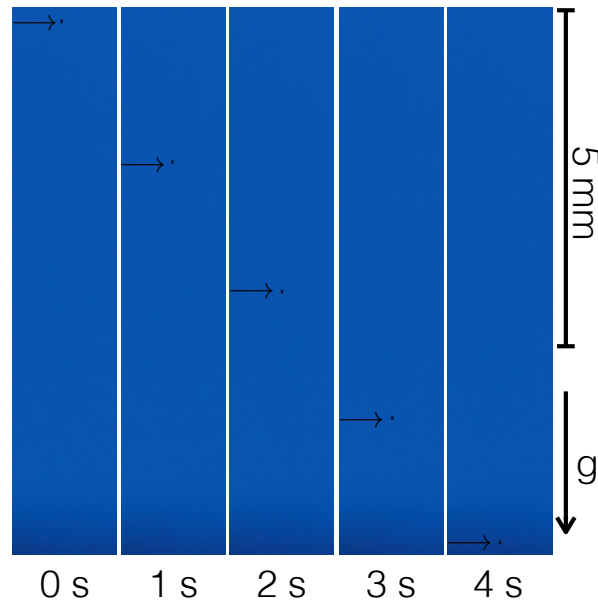


FIGURE 4.5: Image series of a droplet moving down in a FSF of mixture *M5N* with a film thickness of 180 nm. The aqueous droplet consists of 5% ethylene glycol. The displayed images are a cutout of the original image. The film width is around 5 mm, the total length of the film 15 mm. The droplet is placed approximately 3 mm below the upper edge of the film holder.

4.2 Droplet Motion in a SmA Film

In this section, the motion of liquid inclusions in a freely suspended smectic A film will be treated. The properties of the applied film material *M5N* were introduced in chapter 2. The mixture shows a SmA phase at room temperature and forms stable FSFs. The inclusion material consists mainly of water with 5 wt.-% Ethylene Glycol. Only a few experiments were performed with droplets containing 50 wt.-% Ethylene Glycol because the higher viscosity of this mixture impairs the dispensing feasibility.

Considering these inclusion sizes the Reynolds numbers should be small. Approximated values for *M5N* allow a rough calculation. With a density of 1025 kg m^{-3} (8CB) [111], a viscosity of 0.187 Pa s [110], a droplet radius of $25 \mu\text{m}$ and a final droplet velocity of $5000 \mu\text{m s}^{-1}$ the Reynolds number ($Re = 2r\rho v/\eta$) yields $Re \approx 0.0025$. Regarding $Re \ll 1$, a laminar flow in the film can be expected.

After preparation, the film is given time to rest until a homogeneous film thickness develops. The experiments are conducted with the vertical film setup, see section 2.3.2, since it provides a wider field of view than the microscope. The film thickness is determined from interference colors of the reflected light using a spectrometer as described in section 2.4.1. The droplets are placed onto the vertical film by the dispenser and the gravitational force drags the droplet down within the film. An example of the observed droplet motion is given in figure 4.5. The droplet appears as a small black dot within in the blue film.

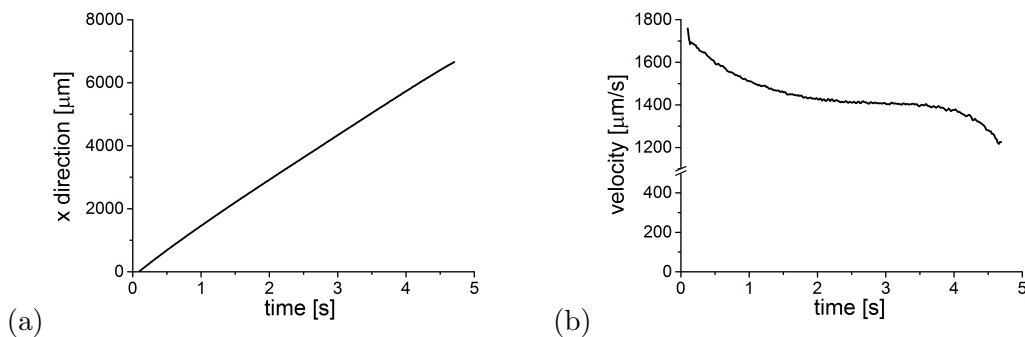


FIGURE 4.6: Data corresponding to figure 4.5. (a) The x-position of a droplet moving in a FSF shown as a function of time. The droplet radius is $21.2 \mu\text{m}$. (b) The corresponding droplet velocity is plotted as a function of time. The signal was smoothed by FFT-filter using 20 data points to regulate the cut-off frequency. Between 2.5 and 3 s, the droplet velocity appears to reach a plateau at about $1400 \mu\text{m/s}$.

4.2.1 Experiments with Embedded Droplets

The position of the droplet in figure 4.5 is plotted exemplary as a function of time in figure 4.6 (a). The data were generated using the droplet tracking technique described in section 2.4.4. The slope seems to follow a linear trend. However, when looking at figure 4.6 (b), a decrease in the corresponding velocity is noticeable. The droplet starts the movement with a velocity of around $1750 \mu\text{m/s}$ and leaves the field of view with a velocity of about $1200 \mu\text{m/s}$. The decrease in velocity during the first 3 seconds is probably due to evaporation and shape change of the inclusion. Subsequent, the velocity seems to reach a short plateau at $1400 \mu\text{m/s}$. Finally, the velocity decreases again because the droplet coincidentally gets close to the sideward frame of the film holder. For film thicknesses d smaller than 100 nm no constant velocity could be found, because the droplets move faster and the observation time is too short to overcome the initial evaporation period. And external air drag increases the mean variation of the data especially for thin films. Still, these data sets are included in the following results and will be treated with care. At times, the problem of non-constant drift velocity occurred also for larger film thicknesses. These data sets for thicker films are not included in the following results.

4.2.2 Determination of the Film Viscosity

The frictional force acting on the inclusion is fundamentally dependent on the film viscosity. Whether the frictional force follows an air friction dependent or a confinement dependent behavior can be determined from a ratio of film width and Saffman length $\ell_s = \frac{d\eta}{2\eta'}$. When twice the Saffman length expands to 2.7 times the film width W , the limit of validity of the air friction model is approached and the confinement is no longer

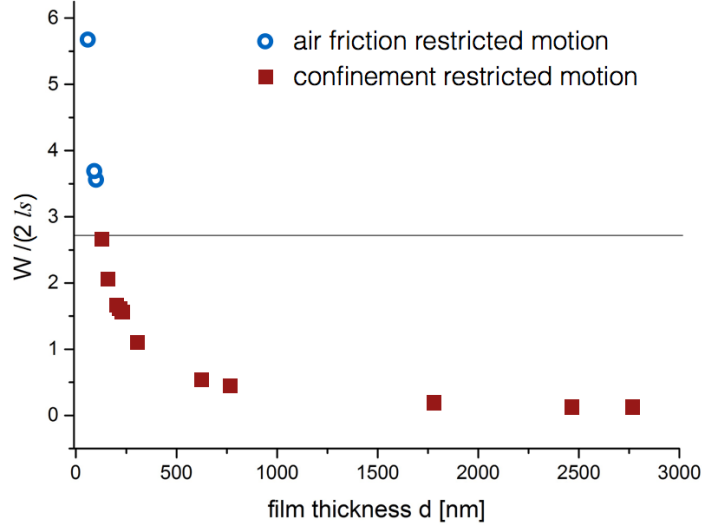


FIGURE 4.7: The film width divided by twice the Saffmann length l_s plotted against the film thickness. The experimental data points cover the full spectrum of film thicknesses measured in this study. The crossover from air friction restricted (blue circles) to confinement restricted (red squares) regime at $W/2l_s = 2.7$ is indicated by a straight line. This plot reveals that the majority of the measured film thicknesses fall in the regime of confinement restricted motion.

negligible [27]. In figure 4.7, the ratio is plotted against the film thickness for a film width of $W = 3.5$ mm. Film thicknesses larger than 122 nm should cause confinement dependent behavior (blue squares). Only three data points are in the regime of air friction restricted behavior (red circles). As mentioned previously, film thicknesses below 100 nm yield unstable velocities and will be not considered in the determination of the viscosity. Thus, only the confinement dependent behavior following equation 4.10 will be considered.

$$F_{\text{fr}} = \frac{v}{b} = 4\pi v d \eta \frac{1}{\ln \frac{W}{2r_m} + C} \quad (4.10)$$

When the frictional force is determined by equation 4.11, the viscosity can be calculated using equation 4.12, with m_{eff} being the effective mass.

$$\begin{aligned} F_{\text{fr}} &= F_{gx} - F_b \\ F_{\text{fr}} &= g(m_{\text{dm}} - \pi r_m^2 d \rho_{\text{film}}) \\ F_{\text{fr}} &= g m_{\text{eff}} \end{aligned} \quad (4.11)$$

$$\eta = \frac{g m_{\text{eff}}}{4\pi v d} \left(\ln \frac{W}{2r_m} + C \right) \quad (4.12)$$

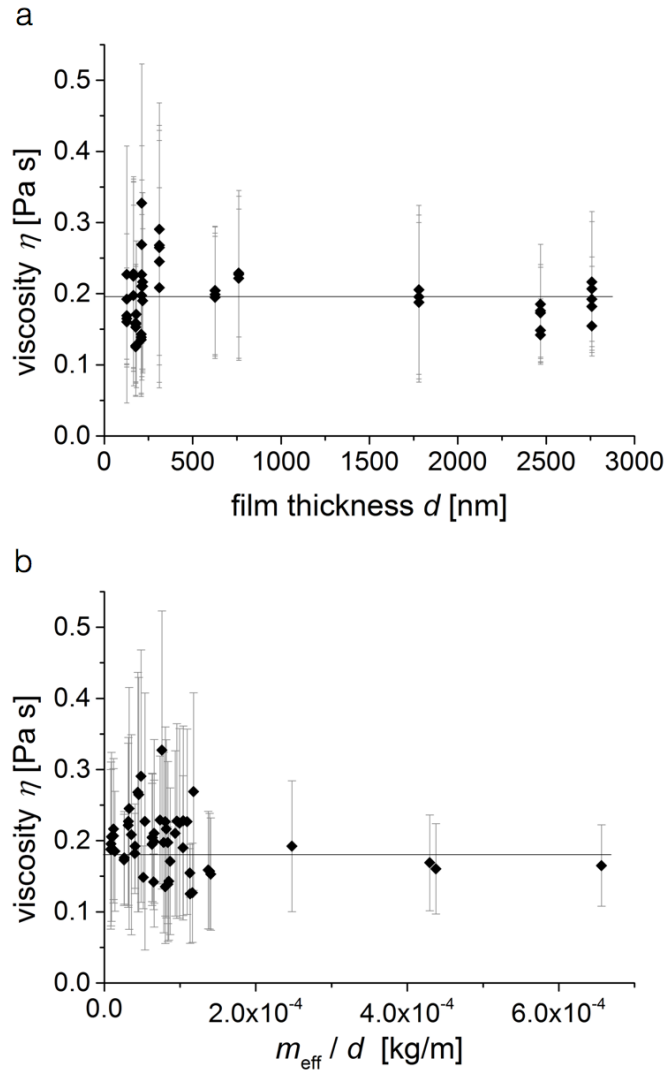


FIGURE 4.8: Viscosity of the *M5N* SmA film as a function of the film thickness (a) and a function of the ratio of effective mass and film thickness (b). Only experimental data in the confinement restricted regime are plotted.

The viscosity η is plotted as a function of the film thickness in figure 4.8 (a). It is equivalent to η_3 as introduced in section 1.1.4. The droplets are slow considering a viscosity of $\eta_3 = 0.187 \pm 0.04$ Pa s as stated by S. Baumgarten [110]. The mean value of the scattered data yield a viscosity of $\eta_3 = 0.198 \pm 0.1$ Pa s. The large error derives from the measurement precision concerning the radius of the droplet. The required large field of view does not allow a high resolution of the droplet. Hence, the determination of the viscosity is more precise using solid inclusions. The dimensions of beads may readily be determined prior to embedding and are constant over the course of the experiment. Diagram (b) in figure 4.8, shows the viscosity over the ratio of the effective mass and the

film thickness. The data set is distributed statistically, confirming that no systematic error is committed considering the inclusion mass.

4.2.3 Droplet Velocities and Mobilities

With the frictional force F_{fr} in the film given by $F_{\text{fr}} = v/b$, where b is the mobility, the equilibrium velocity of a droplet moving in the film can be described following equation 4.13.

$$v = [m_{\text{dm}} g - \pi r_{\text{m}}^2 d \rho_{\text{film}} g] b = m_{\text{eff}} g b \quad (4.13)$$

The term in brackets describes the gravitational force diminished by buoyancy with m_{dm} being the mass of droplet plus meniscus and r_{m} the outer radius of the inclusion with meniscus. The mobility b depends mainly on the film thickness d and the viscosity of the film η . Considering the experimental data in figure 4.9, the mobility b was approximated by two different models. Firstly, the Saffman-Delbrück (SD) model for air-friction dependency is applied following equation 4.14. Secondly, the mobility model for a confinement-restricted motion is shown in equation 4.15. Note, that this equation is modified to suit a rectangular confinement.

$$b = \frac{1}{4 \pi \eta d} \left(\ln \frac{2 \ell_s}{r_{\text{m}}} - \gamma \right) \quad (4.14)$$

$$b = \frac{1}{4 \pi \eta d} \left(\ln \frac{W}{2 r_{\text{m}}} - 0.88458 \right) \quad (4.15)$$

Experimentally, the droplet velocities were measured for different droplet radii and film thicknesses as seen in figure 4.9. The data points are divided in different ranges of droplet radii. The majority of the data comes within the range of 20-24 μm . The diagram shows an exponential decrease of the droplet velocity with increasing film thickness. The experimental data seem to agree with the theoretical expectations. The data points deviate partly from the models since the theoretical data sets are fixed at a droplet radius with meniscus of $r_{\text{m}} = 22 \mu\text{m}$. The experimental velocities are higher than the theoretical plot for larger droplets and lower for smaller ones.

Furthermore, the mobility of droplets in the film was determined. In figure 4.10, the experimental specific mobilities $b' = b \cdot d$ are plotted as a function of the reduced radius $\varepsilon = r_{\text{m}}/\ell_s$. The models for air friction dependence (dashed line) and rectangular confinement dependence (solid line) are drawn in as well. The values are considerably scattered. The substantial error originates mainly from the low resolution of up to 5.5 $\text{Pix}/\mu\text{m}$ which leads to a relatively large error in droplet radius. More importantly,

the mass of the droplet can not be determined accurately. The opening angle of the embedded droplets may change over time. Evaporation leads to loss of droplet mass. In addition, the droplet meniscus grows over time increasing the mass again.

4.2.4 Motion of Two Droplets in Proximity

In figure 4.11, an image of three droplets moving in proximity to each other is shown. The first two droplets move close to each other whereas the third droplet follows in a distance. Even though the droplets have the same radius, the distance over time plot in figure 4.12 reveals that the velocities differ enormously. The two droplets moving close to each other are considerably faster than the separated one. Clearly, the mobility of inclusions depends strongly on their surroundings. The first droplet, indicated with a black line in figure 4.12 shows a velocity v of $862 \mu\text{m}/\text{s}$. The next droplet following in close proximity (red line) moves with a slower velocity v of $763 \mu\text{m}/\text{s}$. These two droplets will be called twin droplets in the following. After 5 s, the distance between them is $300 \mu\text{m}$. This is much shorter than the Saffmann length of $l_s = 1.65 \text{ mm}$ for a film thickness of $d = 300 \text{ nm}$. The third droplet (green line) has only a velocity of $v = 447 \text{ nm}$. The distance between the third droplet and the middle one is already

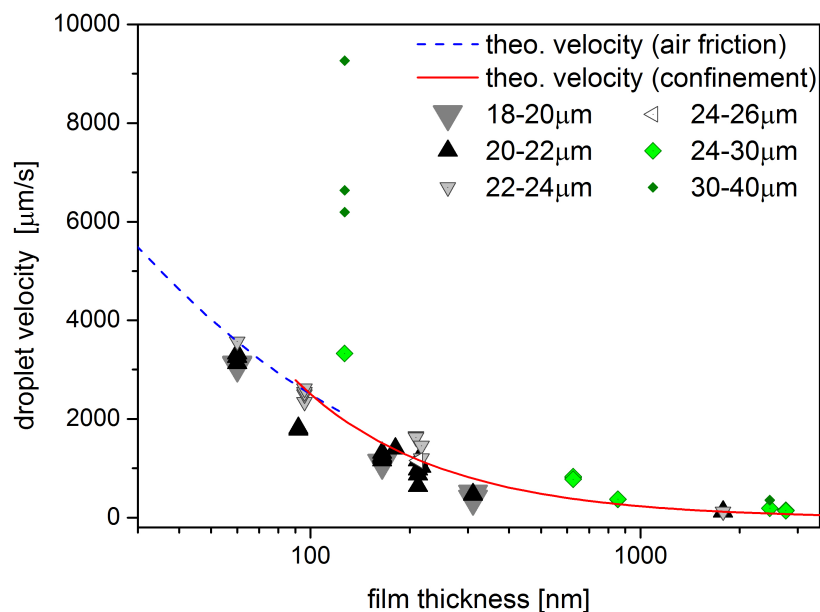


FIGURE 4.9: Single aqueous droplets with 5% (triangles) or 50% (diamonds) Ethylene Glycol were placed on a vertical film. The resulting droplet velocity is shown as a function of the film thicknesses. The experimental data is divided into sets for different droplet radii from $18 \mu\text{m}$ to $42 \mu\text{m}$ as indicated in the legend. The SD model for air friction dependence (dashed line) and the rectangular confinement dependence model (solid line) are shown for droplets with $r_m = 22 \mu\text{m}$. The viscosity is set to 0.198 Pas .

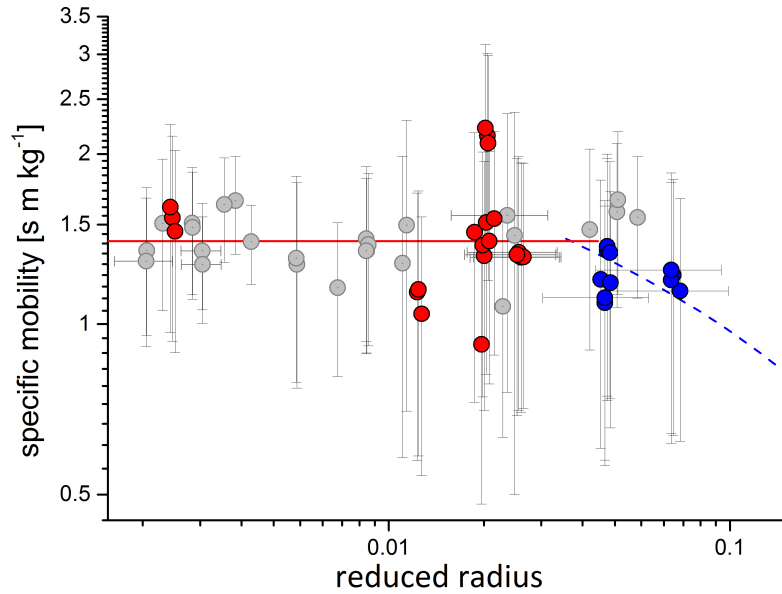


FIGURE 4.10: Specific mobility as a function of reduced radius ε for droplets in a *M5N SmA* film. The specific mobility b' is given by $b' = bd$, the reduced radius by $\varepsilon = r_m/\ell_s$. The experimental specific mobilities are shown as scatter plots with error bars. The droplet radii r_m vary from $18\ \mu\text{m}$ to $42\ \mu\text{m}$. Data points within the range of $r_m = 20 - 24\ \mu\text{m}$ are drawn in as red and blue points. Red circles correspond to the regime of confinement dependent behavior. Data points in the regime of air friction dependence are plotted as blue circles. The dashed blue line displays the theoretical SD model for air-film coupling. The solid red line indicates the theoretical behavior for confinement restricted mobility with a film width limited to $3.5\ \text{mm}$. For both models, the droplet radius is set to $r_m = 22\ \mu\text{m}$. The viscosity is set to $\eta = 0.198\ \text{Pa}\cdot\text{s}$. The film inclination is $\delta = 90^\circ$.

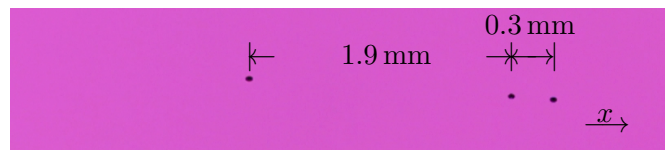


FIGURE 4.11: Image of three droplets moving down a film of $d = 300\ \text{nm}$ thickness, $5\ \text{s}$ after the the first droplet impact. After initial evaporation, all droplets have a radius of about $r_m = 22\ \mu\text{m}$. The motion in x -direction is indicated by an arrow. The distances between the droplets are also drawn in by arrows. The distance between the film barriers is about $W = 3.7\ \text{mm}$.

longer than the Saffman length and the distance to the film holder. It is considered an individually moving droplet.

The twin droplets affect each other and move almost twice as fast as the single droplet. They seem to move rather in a combined flow field than in individual ones. This creates the effect of a much larger droplet. In this combined flow field, the masses of the individual droplets add up and yield a velocity of about twice the speed of a single

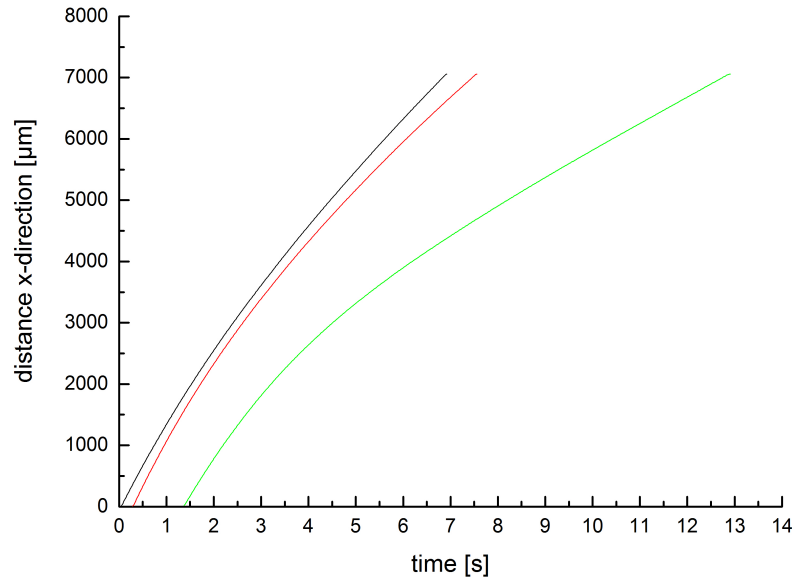


FIGURE 4.12: Distance versus time diagram of the droplets in figure 4.11. Two twin droplets move close to each other and a third droplet follows after about one second. The velocities decrease after impact due to evaporation and become more stable after 2-3 s. The final velocities from left to right are $862 \mu\text{m/s}$, $763 \mu\text{m/s}$ and $447 \mu\text{m/s}$. They were determined considering only the final 4 s of each droplet.

droplet. However, also the flow fields in the film and in air should be extended much wider compared to a single droplet and create a stronger resistance. When looking closer at the velocities of the twin droplets, they apparently do not move at exactly the same speed. The first droplet is about $100 \mu\text{m/s}$ faster than the second one. It is possible that the second droplet has a pushing effect on the first one. Investigating flow fields around twin droplets would give crucial information about this proximity effect.

4.3 Motion of Glass Beads in SmC Films

In this section, the motion of glass beads in SmC films will be investigated. For the complex system of SmC films, solid beads were chosen because of their well defined dimensions. In contrast to the previous experiments, these investigations were performed using the tilted microscope with tilt angles much smaller than $\delta = 90^\circ$. Thus, the effective gravitational force in the film plane is given by the gravitational forces times $\sin\delta$, see equation 4.3.

The Phenylpyrimidine mixture *PP*, cf. chapter 2.1.1, was chosen as film material. The films were inclined between 4° and 14° . Film widths ranged from 2 to 4 mm. The glass beads were picked up and placed on the film using a glass needle. The bead motion is investigated by reflective microscopy between crossed polarizers. Since the birefringence of the smectic material is low for small film thicknesses, only film thicknesses

above $1000\ \mu\text{m}$ were investigated. Below $1000\ \mu\text{m}$, the resulting contrast is not sufficient for optical observations. An exemplary image between crossed polarizers is shown in figure 4.13. The moving beads show a characteristic formation of the \vec{c} director around the bead. Considering the direction of motion, a broader dark brush emerges in front of the bead. This dark brush in moving direction shortens and bends closer to the bead when the velocity increases. The dark brush in front of the bead and three faint broader brushes form a cross with the bead at its center. Additionally, a narrow dark stripe appears behind the bead. It is distinct and sharp next to the bead and broadens further away from the particle. These characteristics will be discussed in the following.

4.3.1 Smectic Orientation around Beads

The orientation of the SmC director around the bead was determined using a λ -wave plate, described in chapter 2.4.2. An image of a stationary bead in the SmC film is shown in figure 4.14. The areas in the image showing a magenta color correspond to a SmC director parallel to the polarizer or the analyser. The bluish areas in the image indicate a parallel alignment of the SmC director to the slow axis of the λ -wave plate, yellow areas are parallel to the fast axis of the λ -wave plate. This indicates a tangential ordering around the bead. In this image it is not distinguishable if the bead generates a $+1$ or a -1 defect. However, it is likely that the bead creates a $+1$ -defect for two reasons. Firstly, all observed extinction crosses between crossed polarizers were following the polarizer-analyzer orientation, cf. figure 4.15. Extinction crosses of -1 -defects are not necessarily oriented along the polarizers. It is rather improbable that the observed extinction crosses correspond to -1 -defects, since they all would have to be aligned along the polarizers. Secondly, the liquid crystal will prefer either radial or tangential anchoring at the surface

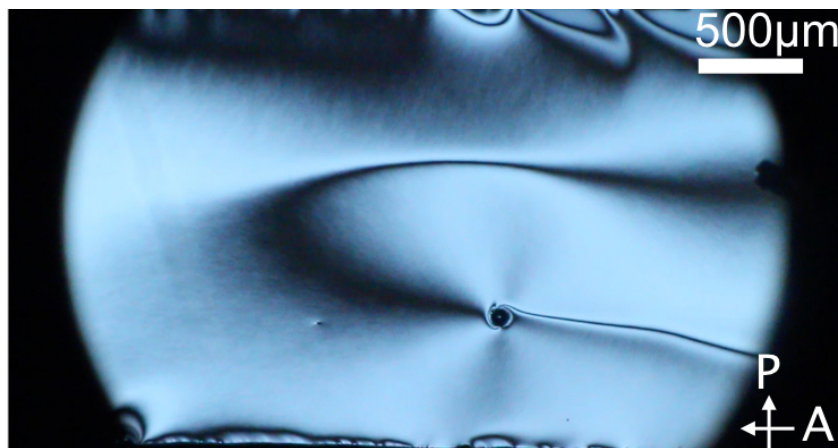


FIGURE 4.13: Silica bead moving from right to left in a SmC film. The image is taken between crossed polarizers indicated by arrows in the bottom right. The film thickness d is $5770\ \text{nm}$ and the film inclination δ is 9.8° .

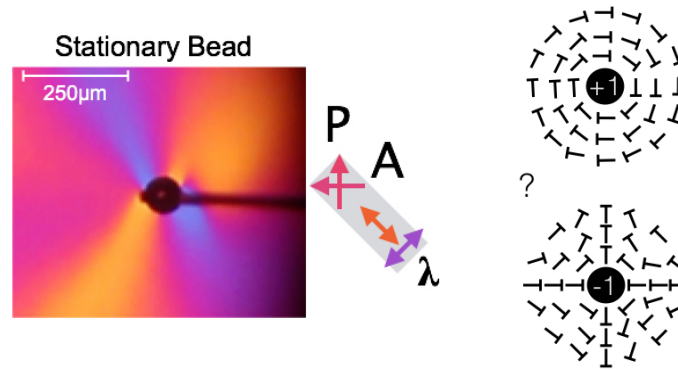


FIGURE 4.14: Orientation of SmC film around a stationary bead visualized via λ -wave plate. The droplet is embedded in the film. At the same time, the droplet is still attached to the glass needle which is positioned slightly above the film and out of focus. Polarizer (P) and analyzer (A) as well as the slow axis (blue) and the fast axis (yellow) of the λ -wave plate are indicated next to the image. At the right hand side, possible orientations of the SmC director are shown. The upper configuration displays a +1-defect, the lower one a -1-defect. Note, that the -1 defect is a rather unlikely configuration around the bead in the film. A +1 defect is much more probable since the extinction cross in the image is oriented along the polarizer-analyzer axis.

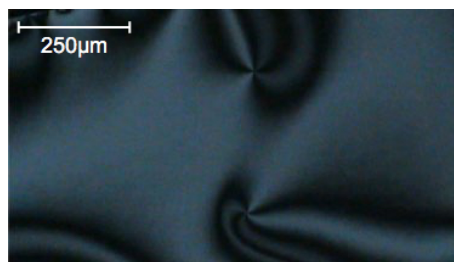


FIGURE 4.15: Defects in SmC film between crossed polarizers. The polarizers are oriented as depicted in figure 4.14.

of the bead. If the bead sits in a -1-defect, both anchoring conditions would occur which would be energetically unfavorable. Thus, the beads are assumed to create tangential +1 defects.

In figure 4.16, a moving bead is displayed using different polarizer and λ -wave plate settings. The image between crossed polarizers in figure 4.16 (a) displays a bead moving from right to left showing an extinction cross with the additional thin black stripe behind the bead. Image (b) was taken with additional λ -wave plate. The picture was taken immediately after image (a). When comparing image (b) with the stationary situation in figure 4.14, it is evident that the orientation differs from the stationary case. The influence of the anchoring orientation on the surrounding director is strongest for stationary beads. With increasing bead velocity, the orientation around the bead is dominated by the flow field. The anchoring alignment persists only in close proximity to the bead, almost indiscernible in figure 4.16. Fig. 4.16 (c) and (d) were also taken shortly after each other. In image (d) the complete set of polarizer, analyzer and λ -wave plate has been rotated around 45° . This is optically equivalent to the rotation of the sample which is faster and was preferred experimentally. The narrow black stripe

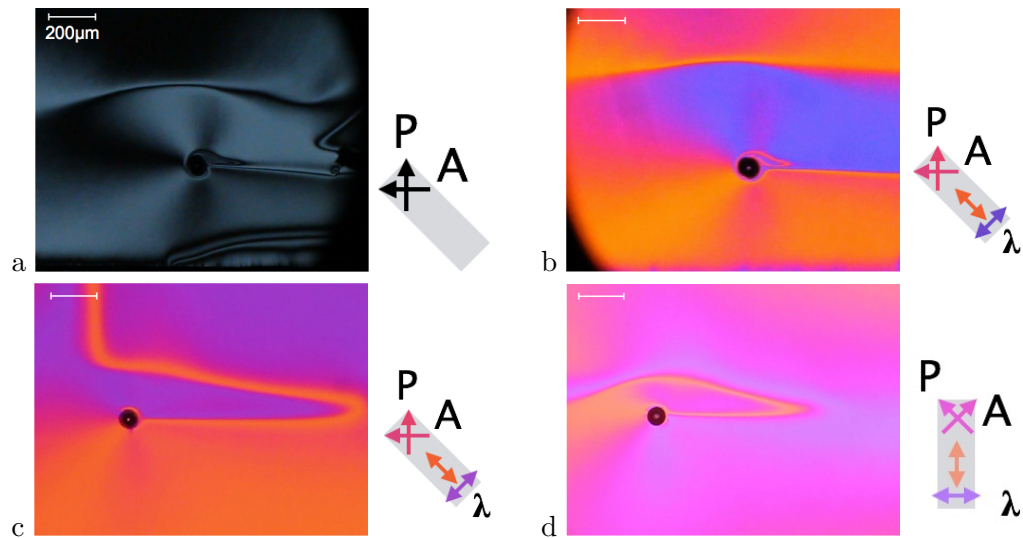


FIGURE 4.16: Orientation of SmC film around a fast moving bead. The polarizer, analyzer and λ -wave plate orientation is indicated to the side of each image. The bead is moving from right to left.

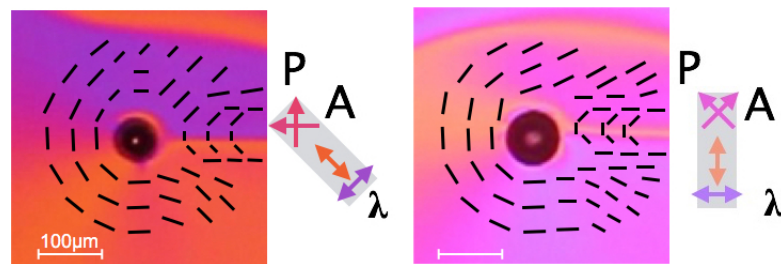


FIGURE 4.17: Orientation of SmC film around a moving bead visualized via λ -wave plate. The orientation of the SmC director according to the colors created by the λ -wave plate is drawn in as a guide for the eye.

behind the bead in fig 4.16 (a) appears yellow in figure (d), revealing the orientation of the SmC director to be perpendicular to the moving direction of the bead. Whereas the broader black stripe behind the bead in figure (a) appears blue in figure (d) giving a parallel orientation towards the moving direction. In figure 4.17, the arrangement of the director is shown for a moving bead. The flow field creates no defect structure. The SmC director in the flow field can be described continuously. This structure is only stable for moving beads and will annihilate as soon as the motion stops. Then, the stationary state anchoring is likely to recover slowly. However, the recovery of the stationary state was not observed within the observation period of a few seconds.

4.3.2 Flow Field around Beads

The flow field around the bead could be estimated by single dust particles on the film. Two examples of a bead moving in the vicinity of a dust particle are shown in figure 4.18. The trajectories of the dust particles, drawn in as thin black lines, seem peculiar at first

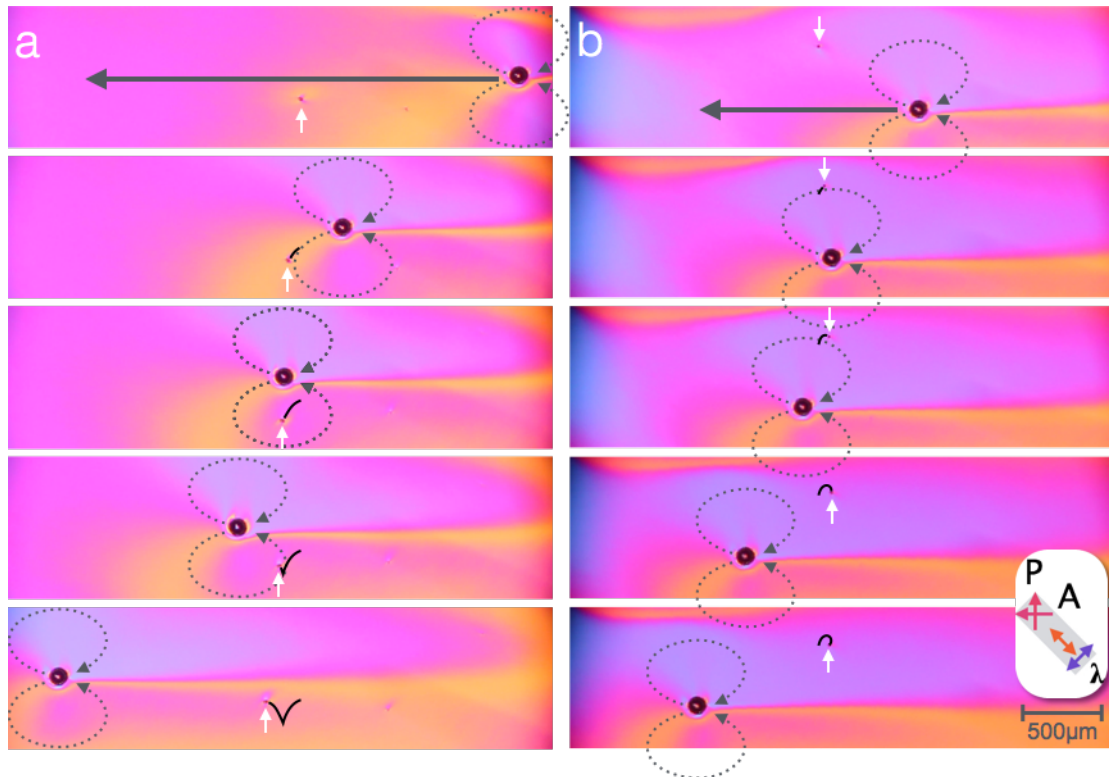


FIGURE 4.18: Motion of a bead in the vicinity of dust particles. Series (a) and (b) were taken at different locations on the SmC film with the same bead. The moving direction of the bead is indicated by a thick arrow, the position of the dust particle by small white arrows. The trajectories that the dust particles have completed are drawn in as black lines. As a guide for the eyes, the convective flow around the bead is approximated by dotted arrows. The orientation of polarizer, analyzer and λ -wave plate is shown in the inset.

glance. On closer inspection, this behavior is a direct result of the laminar convection around the moving bead. The dust particle in figure 4.18(a) is pushed in the same direction as the droplet and out of the way as the droplet gets closer. As soon as the droplet has passed the dust particle it is dragged along behind the droplet resulting in a v shaped trajectory. The trajectory of the dust particle in figure part (b) appears very different. However, the same mechanism applies. Only now, the dust particle is located further from the trajectory of the droplet experiencing another part of the same moving force field.

The same pattern is found for SmA films [110] and was simulated by A. Eremin for isotropic films, cf. figure 4.19. No apparent turbulences were caused by the SmC director field in comparison to SmA. The strength of the flow field in the simulation in figure 4.19 is indicated by arrows as well as a color map. The color indicates the absolute strength of the velocity from slow motion shown in blue to rapid movement in red. The following parameters were chosen for the simulation: film width $W = 1.2$ cm, film thickness $d = 3$ mm, inclusion radius $r = 30$ μ m, film viscosity $\eta_{\text{film}} = 0.52$ Pa.s,

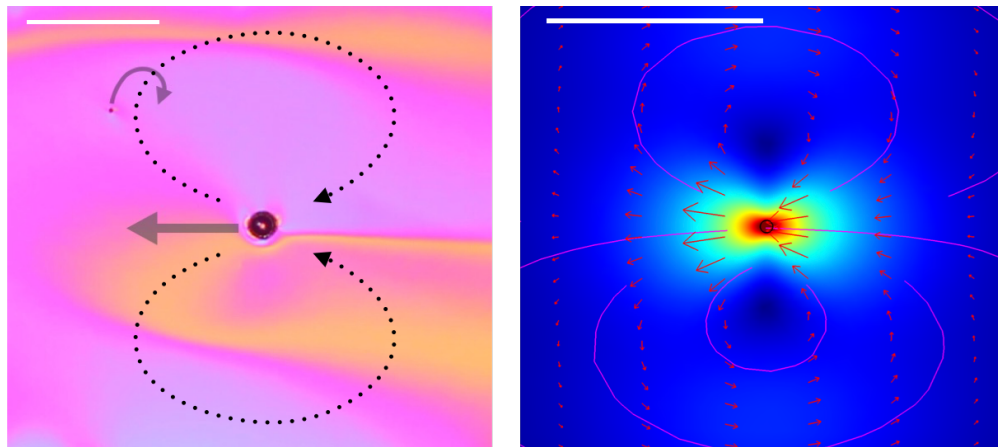


FIGURE 4.19: Flow field around a bead in a SmC film (left) and COMSOL simulation of flow around a bead for isotropic films (right) by A. Eremin, taken from [110]. In the left image, the dotted black arrows are a guide for the eyes indicating the flow in the film. The thick gray arrow represents the direction of motion of the bead. The trajectory of the dust particle, displayed as a thin gray arrow. The image to the right displays a velocity field around a moving bead. The red arrows point out the direction, the length marks the strength of the flow. At the top of the images, the white scale bar marks $500 \mu\text{m}$.

film density $\rho_{\text{film}} = 1025 \text{ kg m}^{-3}$, bead density $\rho_{\text{inc}} = 2490 \text{ kg m}^{-3}$, force per volume $F/V = 9 \cdot 10^{-5} \text{ Nm}^{-3}$.

4.3.3 Bead Moving Through π -Walls

In the previous section, the film was given time to restore a relatively homogeneous field orientation before starting an experiment. Now, the crucial question is targeted whether the orientation of the SmC director affects the mobility of the bead. A bead moving through a more complex SmC orientation field is shown in figure 4.20. The corresponding position over time and velocity is plotted in figure 4.21. The gaps in the position and velocity data derive from resetting the x-y-position every time after the bead drifted out of the field of view.

In figure 4.21(a), the position over time appears linear to the eye. However, the velocity decreases at about $0.7 \mu\text{m/s}^2$, because the bead moves towards the lower film barrier. Additionally, velocity fluctuations are visible in figure 4.21(b). The question whether these fluctuations are caused by different SmC director orientations in the film, as introduced in the last part of section 1.1.4, cannot be answered satisfactory. The fluctuations are $4 \mu\text{m/s}$ at most, which is of the order of the measurement precision. The video resolution is only $3.2 \mu\text{m/Pix}$. This shows a classical problem of mobility measurements where a wide field of view and a high resolution are required at the same

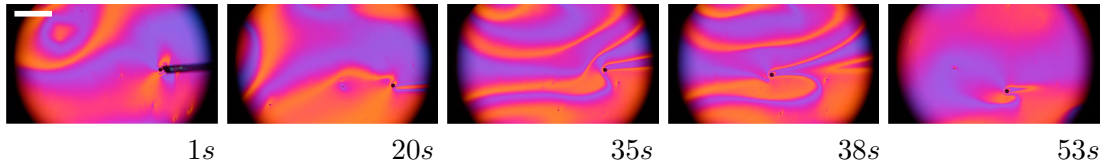


FIGURE 4.20: Images of a bead moving through inversion walls. The images were taken between crossed polarizers and additional λ -wave plate just as in the previous figure. The time after release from the needle is indicated below the images. The bead radius is $r = 26 \mu\text{m}$. The film thickness is $4660 \mu\text{m}$ and the film inclination of $\delta = 8.2^\circ$. The white scale bar in the first image indicates $500 \mu\text{m}$.

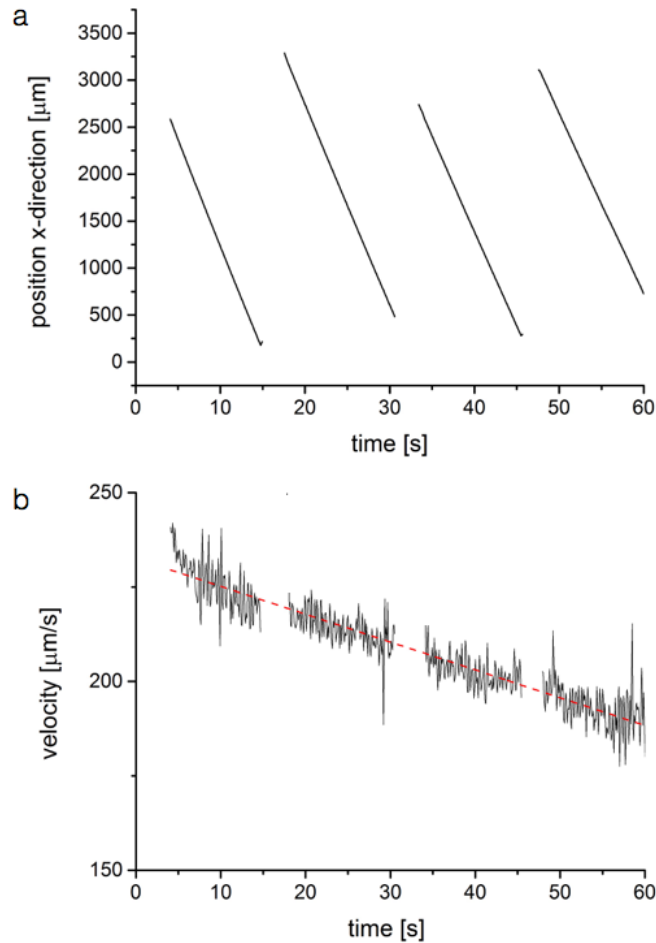


FIGURE 4.21: (a) Position over time of the bead in figure 4.20 passing through π -walls. The trajectories appear to follow a linear behavior. Plot (b) depicts the corresponding velocity of the same bead. The bead leaves the field of view repeatedly. In order to gather more data points, the film is relocated three times via x-y table of the microscope. Thus, the data gaps are related to a repositioning of the whole sample.

time. However, another approach to this problem is tasked by comparing the velocities of beads with and without a π -wall crossing.

Part of figure 4.21(b) is shown again in figure 4.22(b). The corresponding images in figure 4.22(a) offer a more detailed view of the events on the film at each point in time. For comparison, a bead that does not traverse a π -walls is plotted to the right,

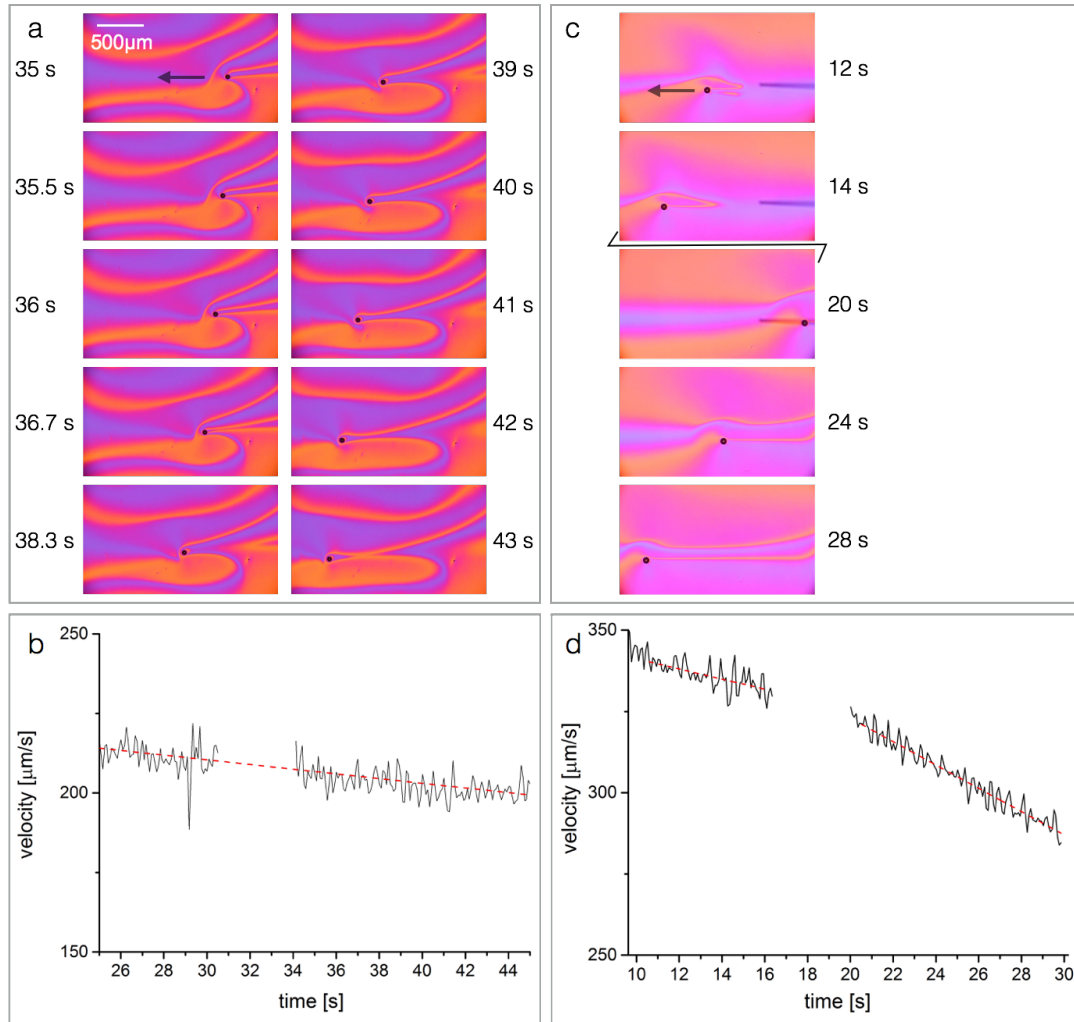


FIGURE 4.22: Beads moving down a film with π -wall (a+b) and without π -walls (c+d). The bead velocities are plotted in (b) and (d). The velocity diagram in (b) is a zoomed in view of figure 4.21(b). The film thicknesses are 4460 nm (a) and 3970 nm (c). The bead radii are 26 μm (a) and 35 μm (b). In both diagrams, the velocity fluctuations seem to be of similar intensity and reveal no significant difference between the two experiments.

c.f. figure 4.22(c+d). In section (c), the first two images are taken before relocation of the microscope stage. Thus, the bead reappears at the right edge of the third image. The thin shadow at right edge of the first three images in (c) belongs to the applicator needle above the film, which is then moved out of the field of view.

The first obvious difference between the two plots is the different deceleration. This derives from different film thicknesses and different bead radii. The bead in figure 4.22(b) is smaller and the film is thicker than in figure (d), thus the deceleration is smaller. The second striking feature is the difference in deceleration for the two parts of the plot in figure 4.22(d). After 10 s, the bead is just released from the needle. This often creates a pushing effect, thus the bead is accelerated in a specific direction. Upon bead release, it seems that the bead is pushed opposite to falling direction. Finally, gravity drags

the bead down against the film barrier. When comparing the fluctuations of the two velocities, no explicit difference can be found. We thus dare say, that the π -walls have no measurable impact on the bead velocity in our range of experiments. This might well be different for self diffusion and remains to be studied.

4.3.4 Bead Velocity and Mobility

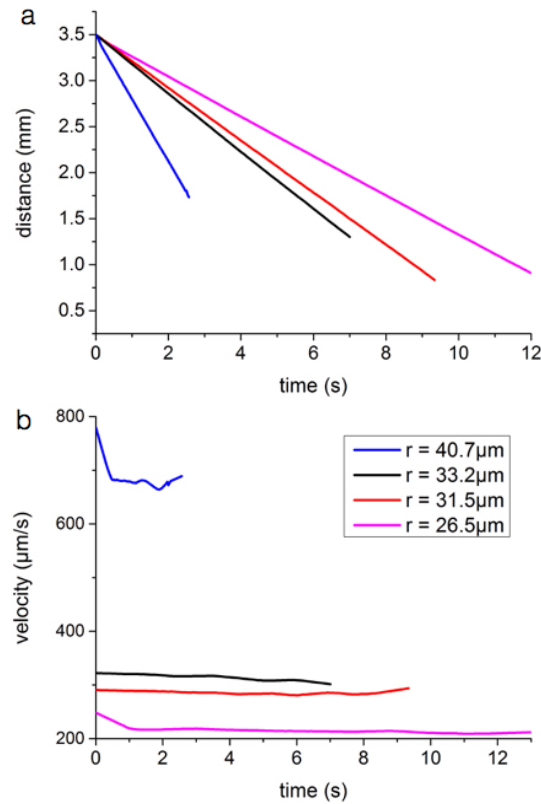


FIGURE 4.23: Position (top) and velocity (bottom) over time of beads with different radii at constant film thickness of $d = 4660$ nm. The microscope inclination angle is constant at $\delta = 8.2^\circ$.

To investigate the velocities and mobilities of beads in a SmC film, different radii of beads were tested. At constant film thickness, the radii varied from $26.5 - 40.7 \mu\text{m}$. The film was left to equilibrate and no π -walls or defect structures were present in these experiments. Fig. 4.23(a) shows a linear behavior of the distance in moving direction over time. The chart in figure 4.23(b) shows the bead velocity versus time to be relatively constant over short time scales. However, small fluctuations are still present.

The specific mobilities $b' = b \cdot d$ of the beads are plotted in figure 4.24 as a function of the bead radius r scaled by the film width W . The experimental data can be described using the Saffman-Delbrück model for confinement dependency (red curve), cf. equation 4.15. Since the film thicknesses in all experiments were intentionally kept above $1000 \mu\text{m}$ all data points are found in the regime of confinement dependent motion. Some

of the data points fall well below the prediction. This is probably caused by a placement of the bead closer to one of the film holder boundaries. Those beads experience a greater effective viscosity.

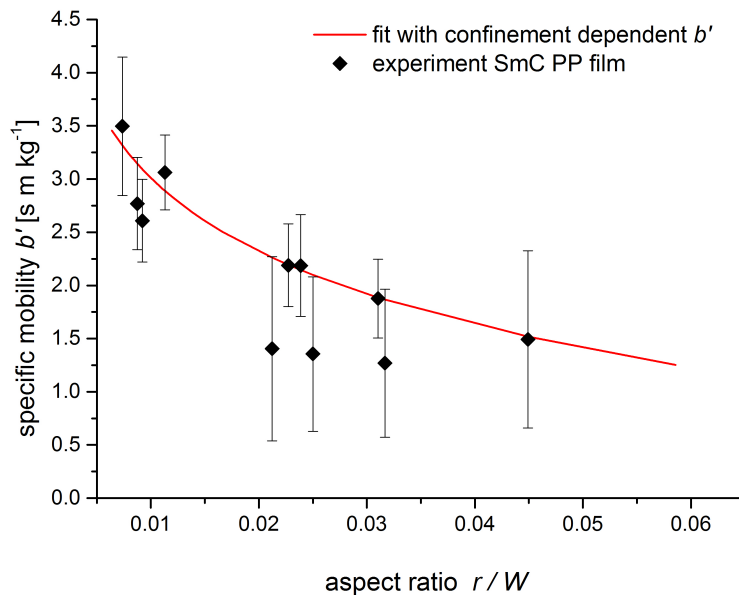


FIGURE 4.24: Specific mobility b' versus the aspect ratio r/W in a *PP* SmC film. The black diamonds show the experimental values with error. The red curve is a fit following equation 4.15 (with $r = r_m$) indicating the theoretical behavior for confinement restricted mobility. The film width W was varied from 1 mm to 3.6 mm. Three different film thicknesses were tested: 1030 nm, 4460 nm and 7640 nm.

4.4 Conclusions

In this chapter, the hydrodynamics of two-dimensional flow was analyzed in detail for small liquid inclusions in SmA films. The mobility was determined by a direct measurement of the gravitation-induced motion of inclusions in inclined films. Diverse new challenges were met in comparison to solid inclusions. The main difficulties with liquid inclusions were evaporation, shape change after film contact and meniscus formation, though, meniscus formation is also found for solid inclusions. Evaporation causes an initial decrease in droplet velocity that ceases a few seconds after impact. The volume of the droplet is a critical parameter that determines the force dragging the particle down the film. Additionally, the meniscus formation cannot be neglected, as done for solid inclusions, since the density of the droplet is very similar to the film density. All these special features make it challenging to determine the actual gravitational force acting on the object. In the previous chapter, the shape change of the droplet in the film was analyzed specifically for the determination of the droplet volume. This knowledge was combined with an analysis of the meniscus geometry to obtain the effective dragging force.

However, apart from the experimental difficulties, a similar behavior as found for solid inclusions could be confirmed for droplets. The droplet mobilities depend strongly on the film thickness as well as the film width. When the Saffman length is of the order of or larger than the film width, finite size effects control the motion, given that the inclusion size is very small compared to the Saffman length. The majority of the data points fell in this regime. The flow in the film and the mobility of an embedded droplet are well described by the 2D Navier-Stokes equations neglecting air friction and equation 4.15 for a rectangular film geometry.

If the Saffman length becomes smaller than the film width, a cross over to a behavior where air-film coupling governs the motion is obtained. Saffman length becomes small for very thin films. In this case, the data agrees with the SD model and the mobilities can be described by equation 4.14. The viscosity η in this equation corresponds to in plane viscosity η_3 . The viscosity of the SmA material *M5N* could be determined to be $\eta_3 = 0.198 \pm 0.1$ Pa.s.

Additionally, the topic of two droplets moving in vicinity of each other was investigated. The experiments indicate that droplets influence each another if the distance between them stays within a certain range. Then, they move in a conjoint flow field yielding roughly twice the velocity they would show individually. Additional investigations are necessary to determine the distance at which the coupling takes effect and how this distance is related to the Saffman-length. Furthermore, it would be interesting to analyze the coupling strength as a function of the distance between the droplets.

The motion of solid inclusions in SmC films was explored as well. SmC films are more complex since the film shows different orientations of the SmC director that interact with the inclusion. Initially, the orientation of the SmC director around a bead was determined in a stationary setting. There are strong indications for the bead filling into a virtual tangential +1 defect. When the bead starts moving this stationary orientation, seen in figure 4.15, is pushed back closer to the bead and a U-shaped orientation is induced, cf. fig 4.17. However, this is only one of the simplest possible orientations. More complex director fields around the bead were observed in films with π -walls. A first qualitative characterization of the flow field around the bead was achieved by tracing single dust particles. The motion of the tracer particles may be explained by a laminar flow field that matches the behavior of SmA films [110].

The mobility in SmC films was investigated for different bead radii at constant film thickness. The theoretical values for finite size behavior after Saffman and Delbrück agree well with the experimental results. Since the tested films were relatively thick in order to achieve strong birefringence, all data points fell into the regime of confinement restricted behavior.

Finally, the key issue whether the orientation of the SmC director affects the mobility of the inclusion was discussed. When beads were moving through complex orientation fields, velocity fluctuations were visible. However, considering a measurement precision of $3.2\ \mu\text{m}/\text{Pix}$, the the \vec{c} director field has no effect on the bead mobility. Further experiments with higher resolution are necessary to possibly distinguish fluctuations from background noise. The impact of the orientation may be not negligible for self diffusion where the motion is locally limited. A suggestion to further investigate effects of director field and inclusion mobility might be the combination of diffusion experiments with an external field that aligns the \vec{c} director.

Bibliography

- [1] P. G. Saffman and M Delbrück. Brownian motion in biological membranes. *Proceedings of the National Academy of Sciences*, 72(8):3111–3113, 1975.
- [2] P. G. Saffman. Brownian motion in thin sheets of viscous fluid. *Journal of Fluid Mechanics*, 73(04):593–602, 1976.
- [3] Pietro Cicuta, Sarah L. Keller, and Sarah L. Veatch. Diffusion of liquid domains in lipid bilayer membranes. *The journal of physical chemistry B*, 111(13):3328–3331, 2007.
- [4] CM White. The drag of cylinders in fluids at slow speeds. In *Proceedings of the Royal Society of London A: Mathematical, Physical and Engineering Sciences*, volume 186, pages 472–479. The Royal Society, 1946.
- [5] F. Reinitzer. Beiträge zur Kenntnis des Cholesterins. *Monatsh. f. Chem.*, 9:421–441, 1888.
- [6] O. Lehmann. Über fließende Kristalle. *Z. phys. Chem.*, 4:462–472, 1889.
- [7] P. G. De Gennes and J. Prost. *The Physics of Liquid Crystals, 2nd Ed.* Oxford University Press, New York, 1995.
- [8] G. Friedel. Les états mésomorphes de la matière. *Ann. Phys.*, 18:273–515, 1922.
- [9] Horst Stegemeyer. *Lyotrope Flüssigkristalle: Grundlagen Entwicklung Anwendung.* Springer-Verlag, 2013.
- [10] W. Maier and G. Englert. Ordnungsgradbestimmung an kristallinflüssigen Schichten durch Messung des Infrarotdichroismus. *Z. Elektrochem., Ber. Bunsenges. Phys. Chem.*, 64:689–694, 1960.
- [11] D. Demus and L. Richer. *Textures of Liquid Crystals.* VEB Verlag für Grundstoffindustrie, Leipzig, 1978.
- [12] Horst Stegemeyer. *Liquid Crystals.* Springer Science and Business Media, 1994.

-
- [13] I. Dierking. *Textures of Liquid Crystals*. Wiley-VCH Verlag, Weinheim, 2003.
- [14] Max Born and Emil Wolf. *Principles of optics: electromagnetic theory of propagation, interference and diffraction of light*. Elsevier, 2013.
- [15] J. L. Ericksen. Anisotropic fluids. *Archive for Rational Mechanics and Analysis*, 4(1):231–237, 1959.
- [16] Frank M. Leslie. Some constitutive equations for anisotropic fluids (continuum with director and constitutive equations for anisotropic fluids, obtaining solutions for simple shear, poiseuille and couette flows). *Quarterly Journal of mechanics and applied mathematics*, 19:357–370, 1966.
- [17] Frank M. Leslie. Some constitutive equations for liquid crystals. *Archive for Rational Mechanics and Analysis*, 28(4):265–283, 1968.
- [18] O. Parodi. Stress tensor for a nematic liquid crystal. *Journal de Physique*, 31(7):581–584, 1970.
- [19] M. Miesowicz. The three coefficients of viscosity of anisotropic liquids. *Nature*, 158(27), 1946.
- [20] W. Helfrich. Molecular theory of flow alignment of nematic liquid crystals. *The Journal of Chemical Physics*, 50(1):100–106, 1969.
- [21] W. Helfrich. Torques in sheared nematic liquid crystals: A simple model in terms of the theory of dense fluids. *The Journal of Chemical Physics*, 53(6):2267–2271, 1970.
- [22] Ch. Gähwiller. Direct determination of the five independent viscosity coefficients of nematic liquid crystals. *Molecular crystals and liquid crystals*, 20(3-4):301–318, 1973.
- [23] F. Schneider, H. Knepe, D. Demus, J. Goodby, G. W. Gray, H.-W. Spiess, and V. Vill. *Physical Properties: Flow Phenomena and Viscosity*. Wiley Online Library, 2003.
- [24] F. Schneider. Measurement of the viscosity coefficient η_3 in free-standing smectic films. *Physical Review E*, 74(2):021709, 2006.
- [25] T. Carlsson, F. M. Leslie, and N. A. Clark. Macroscopic theory for the flow behavior of smectic-c and smectic-c* liquid crystals. *Physical Review E*, 51(5):4509, 1995.

- [26] Zoom Hoang Nguyen, Markus Atkinson, Cheol Soo Park, Joseph MacLennan, Matthew Glaser, and Noel Clark. Crossover between 2d and 3d fluid dynamics in the diffusion of islands in ultrathin freely suspended smectic films. *Physical review letters*, 105(26):268304, 2010.
- [27] A. Eremin, S. Baumgarten, K. Harth, R. Stannarius, Z. H. Nguyen, A. Goldfain, C. S. Park, J. E. MacLennan, M. A. Glaser, and N. A. Clark. Two-dimensional microrheology of freely suspended liquid crystal films. *Phys. Rev. Lett.*, 107:268301, 2011.
- [28] Charles Rosenblatt and Nabil M. Amer. Optical determination of smectic a layer spacing in freely suspended thin films. *Applied Physics Letters*, 36(6):432–434, 1980.
- [29] Zhiyuan Qi, Zoom Hoang Nguyen, Cheol Soo Park, Matthew A Glaser, Joseph E MacLennan, Noel A Clark, Tatiana Kuriabova, and Thomas R Powers. Mutual diffusion of inclusions in freely suspended smectic liquid crystal films. *Physical review letters*, 113(12):128304, 2014.
- [30] A. Pattanaporkratana, C. S. Park, J. E. MacLennan, and N. A. Clark. Manipulation of disk-shaped islands on freely suspended smectic films and bubbles using optical tweezers. *Ferroelectrics*, 310(1):131–135, 2004.
- [31] A. A. Canabarro, I. N. De Oliveira, and M. L. Lyra. Homeotropic surface anchoring and the layer-thinning transition in free-standing films. *Physical Review E*, 77(1):011704, 2008.
- [32] P. V. Dolganov, V. K. Dolganov, and P. Cluzeau. Structure of π - and 2π -walls in smectic films. *JETP Letters*, 96(5):317–321, 2012.
- [33] Harold Eugene Edgerton and James Rhyne Killian. *Flash!: Seeing the unseen by ultra high-speed photography*. CT Branford Co., 1954.
- [34] Arthur Mason Worthington. *The splash of a drop*. Romance of Science. S.P.C.K., London, 1895.
- [35] S. T. Thoroddsen, T. G. Etoh, and K. Takehara. High-speed imaging of drops and bubbles. *Annu. Rev. Fluid Mech.*, 40:257, 2008.
- [36] A.L Yarin. Drop impact dynamics: Splashing, spreading, receding, bouncing. . . . *Annu. Rev. Fluid Mech.*, 38(1):159–192, 2006.
- [37] Stefano Schiaffino and A. A. Sonin. Molten droplet deposition and solidification at low weber numbers. *Physics of Fluids*, 9(11):3172, 1997.

- [38] M. B. Lesser and J. E. Field. The impact of compressible liquids. *Annu. Rev. Fluid Mech.*, 15(1):97–122, 1983.
- [39] M. Rein. Phenomena of liquid drop impact on solid and liquid surfaces. *Fluid Dyn. Res.*, 12(1):61–93, 1993.
- [40] A. L. Yarin and D. A. Weiss. Impact of drops on solid surfaces: self-similar capillary waves, and splashing as a new type of kinematic discontinuity. *J. Fluid Mech.*, 283(-1):141, 1995.
- [41] G. E. Cossali, A. Coghe, and M. Marengo. The impact of a single droplet on a wetted solid surface. *Experiments in Fluids*, 22(6):463–472, 1997.
- [42] An-Bang Wang and Chi-Chang Chen. Splashing impact of a single drop onto very thin liquid films. *Physics of Fluids*, 12(9):2155, 2000.
- [43] R. Rioboo, C. Bauthier, J. Conti, M. Vou, and J. de Coninck. Experimental investigation of splash and crown formation during single drop impact on wetted surfaces. *Experiments in Fluids*, 35(6):648–652, 2003.
- [44] C Josslerand and S Zaleski. Droplet splashing on a thin liquid film. *Phys. Fluids*, 15:1650–1657, 2003.
- [45] Kuo-Long Pan and Chun-Yu Hung. Droplet impact upon a wet surface with varied fluid and surface properties. *J. Coll. Interf. Sci.*, 352:186–193, 2010.
- [46] M.-J. Thoraval, K. Takehara, T. G. Etoh, and S. T. Thoroddsen. Drop impact entrapment of bubble rings. *J. Fluid Mech.*, 724:234–258, 2013.
- [47] N. Vandewalle, D. Terwagne, K. Mulleners, T. Gilet, and S. Dorbolo. Dancing droplets onto liquid surfaces. *Phys. Fluids*, 18:091106, 2012.
- [48] S. T. Thoroddsen, M.-J. Thoraval, K. Takehara, and T. G. Etoh. Droplet splashing by a slingshot mechanism. *Phys. Rev. Lett.*, 106:034501, 2011.
- [49] S. T. Thoroddsen, M.-J. Thoraval, K. Takehara, and T. G. Etoh. Micro-bubble morphologies following drop impacts onto a pool surface. *J. Fluid Mech.*, 708:469–479, 2012.
- [50] Marie-Jean Thoraval, Kohsei Takehara, Takeharu Goji Etoh, Stephane Popinet, Pascal Ray, Christophe Josslerand, Stephane Zaleski, and Sigurdur T. Thoroddsen. von karman vortex street within an impacting drop. *Phys. Rev. Lett.*, 108:264506, 2012.
- [51] M. J. Thoraval and SS. T. Thoroddsen. Contraction of an air disk caught between two different liquids. *Phys. Rev. E*, 88:061001, 2013.

- [52] L. V. Zhang, J. Toole, K. Fezzaa, and R. D. Deegan. Evolution of the ejecta sheet from the impact of a drop with a deep pool. *J. Fluid Mech.*, 690:5, 2012.
- [53] T. Jiang, J. Ouyang, X. Li, J. Ren, and X. Wang. Numerical study of a single drop impact onto a liquid film up to the consequent formation of a crown. *J. Appl. Mech. Techn. Phys.*, 54:720–728, 2013.
- [54] Romain Rioboo, Michel Voue, Helena Adao, Josephine Conti, Alexandre Vaillant, David Seveno, and Joel de Coninck. Drop impact on soft surfaces: Beyond the static contact angles. *Langmuir*, 26(7):4873–4879, 2010.
- [55] M. M. Driscoll and S. R. Nagel. Ultrafast interference imaging of air in splashing dynamics. *Phys. Rev. Lett.*, 107:154502, 2011.
- [56] Jolet de Ruitter, Jung Min Oh, Dirk van den Ende, and Frieder Mugele. Dynamics of collapse of air films in drop impact. *Phys. Rev. Lett.*, 108:074505, 2012.
- [57] John M. Kolinski, Shmuel M. Rubinstein, Shreyas Mandre, Michael P. Brenner, David A. Weitz, and L. Mahadevan. Skating on a film of air: Drops impacting on a surface. *Phys. Rev. Lett.*, 108:074503, 2012.
- [58] Andrzej Latka, Arianna Strandburg-Peshkin, Michelle M. Driscoll, Casey S. Stevens, and Sidney R. Nagel. Creation of prompt and thin-sheet splashing by varying surface roughness or increasing air pressure. *Physical Review Letters*, 109:054501, 2012.
- [59] I. Bischofberger, K. W. Mauser, and S. R. Nagel. Seeing the invisible-air vortices around a splashing drop. *Phys. Fluids*, 25:091110, 2013.
- [60] J. S. Lee, B. M. Weon, J. H. Je, and K. Fezzaa. How does an air film evolve into a bubble during drop impact? *Phys. Rev. Lett.*, 109:204501, 2013.
- [61] M. R. Moore, J. R. Ockendon, and J. M. Oliver. Air-cushioning in impact problems. *IMA J. Appl. Math.*, 78:818–838, 2013.
- [62] Peter D. Hicks and Richard Purvis. Liquid-solid impacts with compressible gas cushioning. *J. Fluid Mech.*, 735:120–149, 2013.
- [63] Tristan Gilet and John W. M. Bush. Droplets bouncing on a wet, inclined surface. *Phys. Fluids*, 24:122103, 2012.
- [64] Joel Koplik and Rui Zhang. Nanodrop impact on solid surfaces. *Phys. Fluids*, 25:022003, 2013.
- [65] Ildoo Kim and X. Wu. Tunneling of micron-sized droplets through soap films. *Phys. Rev. E*, 82(2):026313, 2010.

- [66] Minh Do-Quang, Laurent Geyl, Göran Stemme, Wouter Wijngaart, and Gustav Amberg. Fluid dynamic behavior of dispensing small droplets through a thin liquid film. *Microfluidics and Nanofluidics*, 9(2-3):303–311, 2010.
- [67] P. Cluzeau, G. Joly, H. T. Nguyen, and V. K. Dolganov. Two-dimensional ordering of inclusions in smectic *c* phase. *Journal of Experimental and Theoretical Physics Letters*, 75(9):482–486, 2002.
- [68] P. Cluzeau, G. Joly, H. T. Nguyen, and V. K. Dolganov. Formation of two-dimensional crystal-like structures from inclusions in smectic *c* films. *Journal of Experimental and Theoretical Physics Letters*, 76(6):351–354, 2002.
- [69] C. Bohley and R. Stannarius. Inclusions in free standing smectic liquid crystal films. *Soft Matter*, 4:683–702, 2008.
- [70] P. V. Dolganov, V. K. Dolganov, and E. I. Kats. Anomalies of a meniscus of microinclusions in freely suspended smectic films. *JETP Letters*, 102(4):242–247, 2015.
- [71] P. Cluzeau, V. Bonnard, G. Joly, V. Dolganov, and H.T. Nguyen. Self-organization of n^* inclusions in smc^* free-standing films. *The European Physical Journal E*, 10(3):231–240, 2003.
- [72] P. V. Dolganov, H. T. Nguyen, G. Joly, V. K. Dolganov, and P. Cluzeau. Ferroelectricity-induced effects in interaction and self-organization of inclusions in smectic membranes. *EPL (Europhysics Letters)*, 76(2):250, 2006.
- [73] P. V. Dolganov, H. T. Nguyen, G. Joly, V. K. Dolganov, and P. Cluzeau. Shape of nematic droplets in smectic membranes. *EPL (Europhysics Letters)*, 78(6):66001, 2007.
- [74] Elena S Pikina and Boris I Ostrovskii. Nucleation and growth of droplets in the overheated free-standing smectic films. *The European Physical Journal E*, 40(3):24, 2017.
- [75] Elena S Pikina and Boris I Ostrovskii. Anomalous melting of overheated smectic films. *Liquid Crystals*, 44(5):889–896, 2017.
- [76] Marjetka Conradi, Primož Zihlerl, Andreja Šarlah, and I Muševič. Colloids on free-standing smectic films. *The European Physical Journal E*, 20(2):231–236, 2006.
- [77] H. Schüring, C. Thieme, and R. Stannarius. Surface tensions of smectic liquid crystals. *Liq. Cryst.*, 28:241, 2001.

- [78] Heidrun Schüring and Ralf Stannarius. Isotropic droplets in thin free standing smectic films. *Langmuir*, 18(25):9735–9743, 2002.
- [79] H. Lamb. *Hydrodynamics*. Cambridge University Press, Cambridge, 1932.
- [80] Carl Wilhelm Oseen. *Über die stoke'sche formel und über eine verwandte aufgabe in der hydrodynamik*. Almqvist & Wiksell, 1911.
- [81] B. D. Hughes, B. A. Pailthorpe, and L. R. White. The translational and rotational drag on a cylinder moving in a membrane. *Journal of Fluid Mechanics*, 110:349–372, 1981.
- [82] Eugene P Petrov and Petra Schwille. Translational diffusion in lipid membranes beyond the saffman-delbrück approximation. *Biophysical journal*, 94(5):L41–L43, 2008.
- [83] S. Aliaskarisohi, P. Tierno, P. Dhar, Z. Khattari, M. Blaszczyński, and Th. M. Fischer. On the diffusion of circular domains on a spherical vesicle. *Journal of Fluid Mechanics*, 654:417–451, 2010.
- [84] V. Prasad and Eric R. Weeks. Flow fields in soap films: Relating viscosity and film thickness. *Physical Review E*, 80(2):026309, 2009.
- [85] C. Cheung, Y. H. Hwang, X. L. Wu, and H. J. Choi. Diffusion of particles in free-standing liquid films. *Physical review letters*, 76(14):2531, 1996.
- [86] Tristan T. Hormel, Sarah Q. Kurihara, M. Kathleen Brennan, Matthew C. Wozniak, and Raghuveer Parthasarathy. Measuring lipid membrane viscosity using rotational and translational probe diffusion. *Physical review letters*, 112(18):188101, 2014.
- [87] Christoph Herold, Petra Schwille, and Eugene P. Petrov. Dna condensation at freestanding cationic lipid bilayers. *Physical review letters*, 104(14):148102, 2010.
- [88] Zhiyuan Qi, Cheol Soo Park, Matthew A Glaser, Joseph E MacLennan, and Noel A Clark. Experimental realization of an incompressible newtonian fluid in two dimensions. *Physical Review E*, 93(1):012706, 2016.
- [89] S. Amm, R. Stannarius, and AG Rossberg. Optical characterization of chevron formation in nematic electroconvection. *Physica D*, 126(3-4):171–188, 1999.
- [90] J. Shi, C. Wang, K. Surendranath, V. and Kang, and J. T. Gleeson. Material characterization for electroconvection. *Liquid Crystals*, 29(6):877–880, 2002.
- [91] K. May, K. Harth, T. Trittel, and R. Stannarius. Dynamics of freely floating smectic bubbles. *Europhys. Lett.*, 100:16003, 2012.

- [92] Nikos G. Tsierkezos and Ioanna E. Molinou. Thermodynamic properties of water + ethylene glycol at 283.15, 293.15, 303.15, and 313.15 k. *Journal of Chemical & Engineering Data*, 43(6):989–993, 1998.
- [93] S. Dölle, K. Harth, T. John, and R. Stannarius. Impact and embedding of picoliter droplets into freely suspended smectic films. *Langmuir*, 30:12712, 2014.
- [94] C. Bohley and R. Stannarius. Colloidal inclusions in smectic films with spontaneous bend. *Eur. Phys. J. E*, 23(1):25–30, 2007.
- [95] Duong Hoang Nguyen. *Smectic Liquid Crystal Freely Suspended Films: Testing Beds for the Physics in Thin Membranes*. PhD thesis, University of Colorado, 2011.
- [96] K. Harth and R. Stannarius. Measurement of the interface tension of smectic membranes in water. *Phys. Chem. Chem. Phys.*, 15:7204, 2013.
- [97] J.-W. Kim, H. Kim, M. Lee, and J. J. Magda. Interfacial tension of a nematic liquid crystal/water interface with homeotropic surface alignment. *Langmuir*, 20:8110, 2004.
- [98] K. Harth and R. Stannarius. Corona patterns around inclusions in freely suspended smectic films. *Eur. Phys. J. E*, 28(3):265–272, 2009.
- [99] K. Harth, R. Stannarius, B. Schulz, and Ch. Bahr. Atomic force microscopy of menisci of free-standing smectic films. *Soft Matter*, 7:7103, 2011.
- [100] S. Dölle and R. Stannarius. Microdroplets impinging on freely suspended smectic films: Three impact regimes. *Langmuir*, 31:6479, 2015.
- [101] Y Ishii and Y Tabe. Gas permeation of lc films observed by smectic bubble expansion. *The European Physical Journal E: Soft Matter and Biological Physics*, 30(3):257–264, 2009.
- [102] T. Lopez-Leon, A. Fernandez-Nieves, M. Nobili, and C. Blanc. Nematic-smectic transition in spherical shells. *Phys. Rev. Lett.*, 106:247802, 2011.
- [103] H.-L. Liang, S. Schymura, P. Rudquist, and J. Lagerwall. Nematic-smectic transition under confinement in liquid crystalline colloidal shells. *Phys. Rev. Lett.*, 106:247801, 2011.
- [104] H.-L. Liang, G. Scalia E. Enz, and J. Lagerwall. Liquid crystals in novel geometries prepared by microfluidics and electrospinning. *Mol. Cryst. Liq. Cryst.*, 549:69, 2011.

-
- [105] H.-L. Liang, R. Zentel, P. Rudquist, and J. Lagerwall. Towards tunable defect arrangements in smectic liquid crystal shells utilizing the nematic-smectic transition in hybrid-aligned geometries. *Soft Matter*, 8:5443, 2012.
- [106] H.-L. Liang, JungHyun Noh, R. Zentel, P. Rudquist, and J. Lagerwall. Tuning the defect configurations in nematic and smectic liquid crystalline shells. *Phil. Trans. Roy. Soc. A*, 371:20120258, 2013.
- [107] Q. Liang, S. W. Ye, P. W. Zhang, and J. Z. Y. Chen. Rigid linear particles confined on a spherical surface: Phase diagram of nematic defect states. *J. Chem. Phys.*, 141:244901, 2014.
- [108] Yangsoo Son, Chongyoup Kim, Doo Ho Yang, and Dong June Ahn. Spreading of an inkjet droplet on a solid surface with a controlled contact angle at low weber and reynolds numbers. *Langmuir*, 24(6):2900–2907, 2008.
- [109] M. Conradi, P. Zihler, A. Šarlah, and I. Muševič. Colloids on free-standing smectic films. *Eur. Phys. J.*, 20:231, 2006.
- [110] S. Baumgarten. *Bewegung von Inklusionen auf flüssigkristallinen Filmen*. Diplomarbeit, Universität Magdeburg, 2011.
- [111] A. J. Leadbetter, J. A. L. Durrant, and R. Rugman. The density of 4'-n-octyl-4-cyano-biphenyl (8cb). *Mol. Cryst. Liq. Cryst.*, 34:231–235, 1977.
-

Dipl.-Chem. Sarah Dölle
Bertha-von-Suttner-Str.20
14469 Potsdam

Selbstständigkeitserklärung

Hiermit erkläre ich, dass ich die von mir eingereichte Dissertation mit dem Titel:

„Dynamics in Thin, Freely Suspended, Fluid Films: Impact of Picoliter Droplets and In-plane Microrheology“

selbstständig verfasst habe, sie nicht schon als Dissertation verwendet wurde und die benutzten Hilfsmittel und Quellen vollständig angegeben wurden.

Weiterhin erkläre ich, dass ich weder diese noch eine andere Arbeit zur Erlangung des akademischen Grades doctor rerum naturalium (Dr. rer. nat.) an anderen Einrichtungen eingereicht habe.

Potsdam, 22.09.2017

Sarah Dölle